Politecnico di Torino

Scuola di Dottorato

Ph. D. Thesis

Cavity Flows Control by High Frequency Forcing

Mariano A. Martinez

2012

ACKNOWLEDGEMENTS

Thanks to my dear Professor Michele Onorato, who guided me all through my doctoral studies, even after his retirement. His outstanding professional and human qualities are a clear example to follow. Also, thanks to his wife Susana. Together, they make Ph.D. students feel like part of their beautiful family.

To Dr. Gaetano Di Cicca, great experimentalist researcher who was my tutor after the retirement of Prof. Onorato, thanks for all his helpful guidance in performing the PIV tests, in the analysis of the results and in the writing of this thesis.

Thanks to Dr. Michele Iovieno, for all his help in the stability analysis of the cavity flow.

Thanks to my former colleagues Dr. Christian Haigermoser, Dr. Lukas Vesely and Dr. Peter Bailey. As part of my working group they studied other aspects of the cavity flow leaving an important background of knowledge in our “team”.

Thanks to Eng. Kirstin Heuler, as a young Erasmus undergraduate student she cooperated, working hardly in the analysis of the stability.

TABLE OF CONTENTS

This thesis and the research work it is based on was developed under the Project

AeroTraNet

http://aerotranet.imft.fr

TABLE OF FIGURES

ABSTRACT

In the surfaces of vehicles, such as airplanes, cars and trains, open cavities are an important source of aerodynamically generated noise, drag increase, and dangerous pressure fluctuations. Many different methods have been tested to suppress these undesired effects; some of them reached a partial success. In general, it can be seen that methods which are simple, economic and easy to apply achieve an effect that is restricted to a small operational range, while those which offer a wider operational range are complex and expensive.

It has been recently discovered that exciting the flow at high frequencies it is possible to suppress or weaken the undesired effects in a wide range of flow conditions. Additionally, this forcing can be generated by a simple Von Karman wake. In this way both advantages, simplicity and a wide operational range, can be achieved at the same time.

The physical mechanisms leading to cavity flow control by high frequency forcing is not well understood yet. The author of this thesis intends to offer a contribution toward a physical explanation for them, based on the analysis of data acquired with the Time Resolved PIV technique.

SOMMARIO

Sulle superfici di veicoli, come aerei, automobili e treni, le cavità aperte sono una importante sorgente di rumore aerodinamico, e producono aumenti di resistenza e di fluttuazioni di pressione che possono risultare pericolose. Per cercare di eliminare questi effetti indesiderati, nel corso degli ultimi anni sono state studiate diverse metodologie di controllo, alcune delle quali hanno mostrato un'efficacia almeno parziale. In linea generale, si è potuto osservare che le metodologie più semplici, economiche e facili da implementare mostrano una buona efficacia solo in un range di funzionamento ristretto, mentre quelle più complesse e costose risultano essere efficaci in un range più ampio.

È stato recentemente dimostrato che, introducendo nel flusso di cavità una forzante ad alta frequenza, è possibile cancellare o attenuare gli effetti indesiderati in un ampio intervallo dei parametri di funzionamento. Questa forzante può essere generata anche da una semplice scia di Von Karman. In questa maniera si possono ottenere contemporaneamente entrambi i vantaggi, semplicità e ampio range di funzionamento.

I meccanismi fisici che sono alla base del controllo del flusso di cavità per mezzo di un forcing ad alta frequenza non sono ancora chiaramente conosciuti. L'autore di questa tesi si propone di offrire un contributo all'individuazione di tali meccanismi, per mezzo di uno studio sperimentale condotto utilizzando la metodologia Time Resolved PIV.

RESUMEN

En la superficie de vehículos, tales como aviones, automóviles y trenes, las cavidades abiertas son una importante fuente de ruido generado aerodinámicamente, de aumento de la resistencia y de peligrosas fluctuaciones de presión. Diversos métodos han sido probados para suprimir estos efectos no deseados; algunos de los cuales han logrado un éxito parcial. En general, puede observarse que los métodos que son simples, económicos y fáciles de aplicar logran un efecto limitado a un rango operacional pequeño, mientras que aquellos que ofrecen un rango operacional más amplio son complejos y onerosos.

Recientemente se ha descubierto que excitando el flujo a altas frecuencias es posible suprimir los efectos no deseados en un amplio rango de condiciones de flujo. Además, este forzado puede ser generado por una simple estela de Von Karman. De este modo ambas ventajas, simplicidad y amplio rango operacional, pueden ser logradas al mismo tiempo.

El mecanismo físico subyacente al Control de Flujo en Cavidades por Forzado de Alta Frecuencia no está claramente comprendido aún. El autor de la presente tesis se propone ofrecer una explicación física para el mismo, basada en el análisis de los datos adquiridos con la técnica de PIV resuelto en el tiempo.

Chapter 1

INTRODUCTION AND HISTORY

Fluids motion has awakened the curiosity of scientists since the old times. Many of them tried to explain it achieving different levels of success, but always partial.

In the ancient times the interest was generated by practical reasons. In Egypt, Mesopotamia and India the necessity of controlling water for irrigation arose. The development was limited to the construction of channels. In 250 B.C. Archimedes postulated the principles of hydrostatics and flotation. Despite the technical advances that implied the construction of sophisticated aqueducts by the Romans and sophisticated rowboats and sailboats by different civilizations, the knowledge on fluids motion did not progress significantly for many centuries.

As the science progressed, experimentation acquired its methodology and mathematics developed, the primitive descriptive and artistic approaches of the first times started being replaced by scientific theories. Those theories achieved an increasing prediction capacity based in more or less complex mathematical models.

The fundamental principles of classical fluid-dynamics started to be drawn between the XVII and XVIII centuries, with the postulates of Newton, Bernoulli and Euler. However, during many years, a strong separation between theoretical fluid-dynamics and practical fluid-dynamics was verified. Mathematicians and Physicists formulated laws for the fluids motion without considering their viscosity; therefore, they were useless for the engineers who had to perform their designs and calculations based on reality. On the other hand, engineers formulated empirical laws with scarce scientific fundamental that were applicable only to particular cases.

After the work of Osborne Reynolds and others, by the end of the 19th century both methodologies could start being combined. The singular contribution of Ludwig Prandtl in the 20th century, who proposed the concept of boundary layer, permitted the final unification of both theoretical-scientific and practical fluid-dynamics.

The understanding and prediction of the fluid motion is of paramount importance for the development of a large number of technical applications. For example, when civil constructions are designed (buildings, bridges, sport stadiums,…), it is fundamental to know the characteristics of the wind in the region, and the way the structure will behave under the conditions it will be submitted to. In the same way, when vehicles, like automobiles, buses, ships and aircraft, are designed their aerodynamic and/or hydrodynamic study is fundamental to diminish the drag, noise and to enhance their comfort.

In spite of the great development experienced by fluid-dynamics in the last years, fluid motion can be predicted only partially and in limited circumstances; being even more difficult to succeed in any attempt to control it. This is the reason why the important branch of Flow Control has an important handcraft component together with the scientific one.

In the surface of vehicles, such as airplanes, cars and trains, open cavities are an important source of aerodynamic noise, increased drag, and dangerous pressure fluctuations. In the present thesis the author intends to contribute with new details on this particular fluid-dynamical configuration, known as “cavity flows”, and to explain the physical fundamentals of a new and successful control technique for it.

The experimental work will be performed using the modern flow visualization technique called *Time Resolved Particle Image Velocimetry*. With this technique it is possible to do an indirect visualization of the flow. It is highly reliable and, with its very high time and space resolution, offers highly detailed information that could not be achieved with other techniques. The acquired data, after a basic processing, are presented as instant velocity

fields. In addition to the dynamic visualization of the flow, these vector fields will be analyzed using different statistical methods, frequency spectra, vorticity fields and vortex visualization.

Chapter 2

MOTIVATIONS, OBJECTIVES AND CONTRIBUTION TO THE SCIENTIFIC KNOWLEDGE

2.1 Motivations

Cavity Flows Control is a branch of the Mechanics of Fluids that started to be developed by the middle of the 20th century. Despite all the work done on this field, there is still a lot to discover. The importance that is internationally assigned to it can be appreciated by considering the number of active research projects currently existing all around the world. It was in one of those projects, called AeroTranet (Marie Curie Actions), where the author of this thesis had his first contact with Cavity Flows and started working on it. During the following two years, under the expert direction of Professor Michele Onorato, and together with his colleagues Eng. Christian Haigermoser and Eng. Lukas Vesely, the author performed several experimental tests in the laboratories of the Dipartimento di Ingegneria Aeronautica e Spaziale at the Politecnico di Torino, Italy.

Each one of those researchers faced the subject with a different approach and was dedicated to the development and research of a different control method. After studying several articles to know the 'state of the art', the undersigned become immediately interested in the suppression of the undesired effects of cavity flows by High Frequency Forcing. This resulted to be an exciting research field; since the success of this technique was already known but the understanding of the underlying physical mechanism, leading to those effects, was still ignored. To contribute with the necessary knowledge to the understanding of those effects constitutes the main motivation of this thesis.

2.2 Objectives

A clear contrast between the technical development and the scientific research can be observed in this case; at the same time that useful complementarities arises between them.

The control mechanism this thesis is based on seems to be successful enough in the suppression of the undesired elements of the cavity flows to recommend its usage in the technical applications that could require it. However, the scientific investigation success seemed to be still far away at the moment of starting this work.

What for the technical development is considered an achievement, for the scientific research is the beginning of a threat; since the first one searches for an effect to solve a concrete problem, without caring about its causes, while the second one starts from the observance of this effect with the purpose of explaining its causes.

The contribution to the understanding of the physical phenomena leading to the suppression of the pressure peaks in a cavity flow by high frequency forcing, constitutes the central core of this thesis and its main objective.

2.3 Contribution to Scientific Knowledge

- To contribute with new data on cavity flows obtained by modern dynamic flow visualization techniques (Time Resolved PIV)

- To confirm the efficiency of the high frequency forcing technique (performed by a rod in cross-flow) to suppress the undesired effects in cavity flows.

- To clarify the underlying physical fundamentals of the high frequency forcing technique to suppress cavity flows undesired effects.

Chapter 3

CAVITY FLOWS

3.1 How was the problem discovered?

In the early ‘50s studies performed on the bombs bay of an aircraft B.47 showed that, on the basis of random pressure fluctuations, strong periodic pressure fluctuations appeared. Krishnamurty (1) discovered that those periodic fluctuations were accompanied by a strong sound radiation and that their frequencies were higher as the velocities were increased and it diminished as the cavity was longer.

A bit later Plumbee et al. (2) concluded that the periodic fluctuations in cavities were due to acoustic resonance excited by the turbulent Boundary Layer approaching the cavity. This was rapidly discarded by Krishnamurty who demonstrated that the periodic fluctuations were also present when the incoming Boundary Layer was laminar. However, he confirmed that the acoustic resonance played an important role, but the ‘forcing function’ would be a property of the flow on the cavity rather than the incoming Boundary Layer.

In 1964 Rossiter (3) investigated the flow past a cavity and discovered the mechanism of self sustained oscillations based in a natural feedback loop. He proposed a formula to calculate the frequency of the resonant instability that will be explained in the next chapter.

3.2 First attempts to control

Rossiter, himself, led the first attempt to suppress the Periodic Pressure Fluctuations. He obtained an acceptable level of reduction placing three different spoilers ahead of the cavity (3).

Many other methods attempting to control cavity oscillations have been developed until our days. However, all of them have been just partially successful. The application of leading edge spoilers and flaps is certainly the most common technique, even when it is only capable to suppress the undesired oscillations in a very narrow band of flow conditions and its utilization introduces many undesirable effects such as increased drag.

For that reason many other suppression techniques have been developed with variable success. Until the late nineties, none of them seemed to join all the basic requirements. While the simpler techniques offered a narrow range of operation and an increased drag, others offering a wider range appear to be excessively complex and expensive.

Since 1997, a new technique called *High frequency forcing by a rod in crossflow* appears to fulfill all the requirements; however, its physical basis is not well understood, yet.

3.3 Definition

What do we call *cavity flows*?

Let us consider a flat surface immersed in a fluid moving in a direction parallel to it. Let us suppose now that in this surface there is an open cavity (Figure 1). A characteristic fluid-dynamic configuration will develop in the neighborhood of the cavity. This particular configuration is known as “Cavity Flow”.

This kind of flow is highly unsteady. When the incoming boundary layer reaches the cavity leading edge the flow detaches giving place to a shear layer on the cavity mouth. Kelvin-Helmholtz instabilities start to develop in this naturally unstable layer, giving birth to vortices that travel downstream. As will be seen later, such vortices present a periodicity that will be fundamental in the genesis of the problem we want to solve.

Despite the unsteady characteristics of this flow, in the interior of the cavity two typical and more or less steady vortical structures can be identified (Figure 1). The larger vortex is placed downstream, covering approximately three quarters of the cavity mouth and one half of its bottom, while, the smaller counter-rotating vortex, is placed upstream in the bottom of the cavity. Further details on this figure will be given later on this thesis.

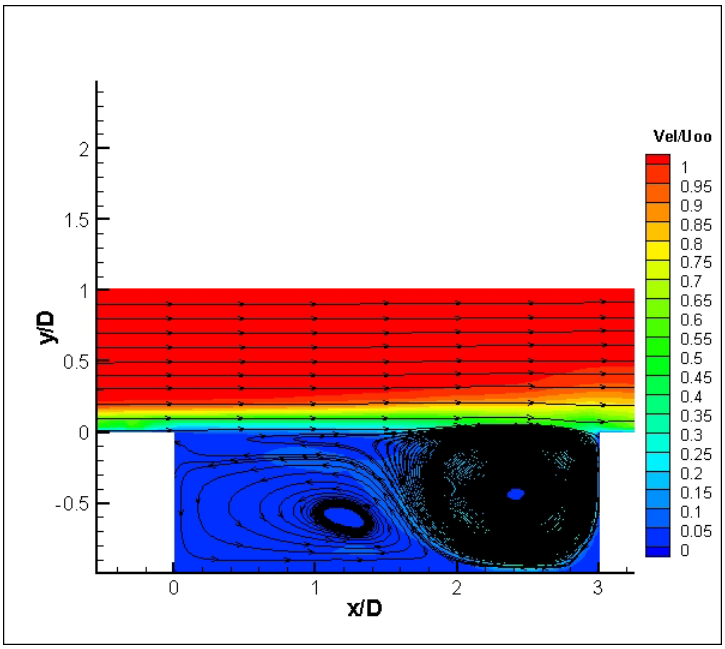

Figure 1. Non-dimensional mean velocity field. $\left(\frac{Local\ \ Mean\ \ Velocity}{Free\ \ Stream\ \ \ Mean\ \ Velocity}\right)$.

3.4 Classification and geometry

Independently of the existence of some characteristic patterns which are common to all cavity flows, the general characteristics can differ in each particular case. The cavity geometry and the incoming flow properties affect the flow patterns in different ways.

Let us start analyzing the flow down a step (Figure 2). We can observe that the flow detaches from the leading edge of the cavity and reattaches ahead, somewhere in the bottom of the cavity. The pressure in the separated region is lower than in the free stream and the flow speed increases. Near the reattachment point a stagnation point will appear. A recirculation zone appears from the flow that reattaches before the stagnation point. The position of this point will be placed more forward as the incoming flow velocity is higher (4) and the step is higher.

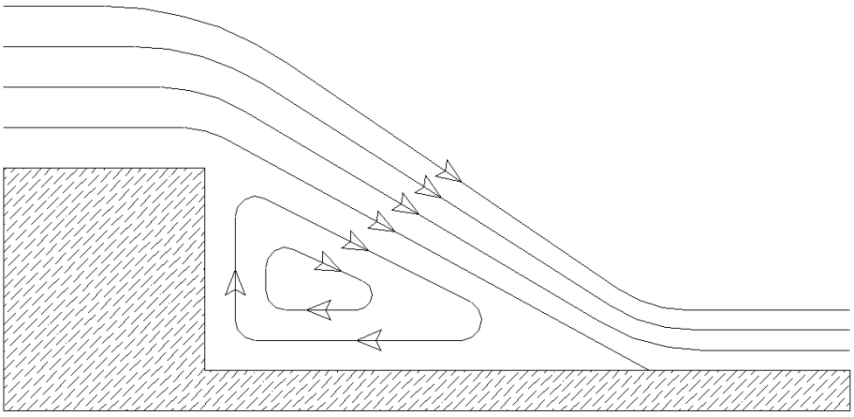

Figure 2. Approximate sketch of a flow down a step configuration.

Let us now analyze the flow up a step (Figure 3). As the flow approaches the step its pressure rises and its horizontal velocity diminishes. When the velocity gradient $\partial u/\partial y$ in the bottom of the cavity becomes zero (5) the flow detaches, jumping over the step and reattaching beyond it. A stagnation point will be placed in the neighborhood of the detaching point and a recirculation zone will be found downstream to it. The stagnation point will be placed more downstream as the free stream velocity and the step are higher.

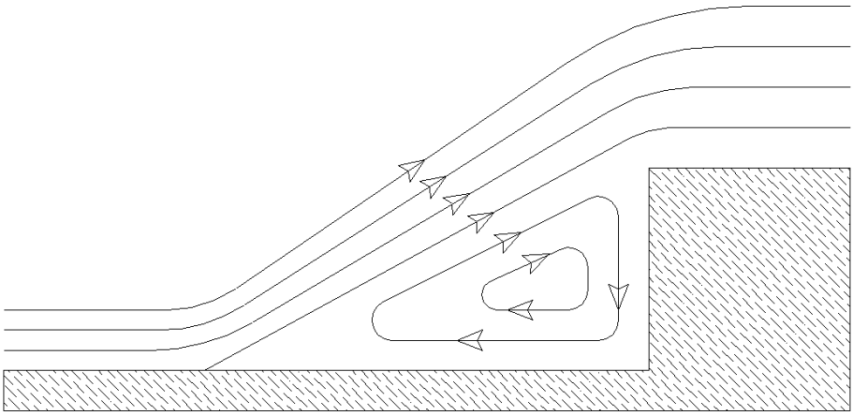

Figure 3. Approximate sketch of a flow up a step configuration.

If we combine the two patterns described before (Figure 4) we will have a new pattern that is similar to a cavity with a low D/L (depth/length) ratio.

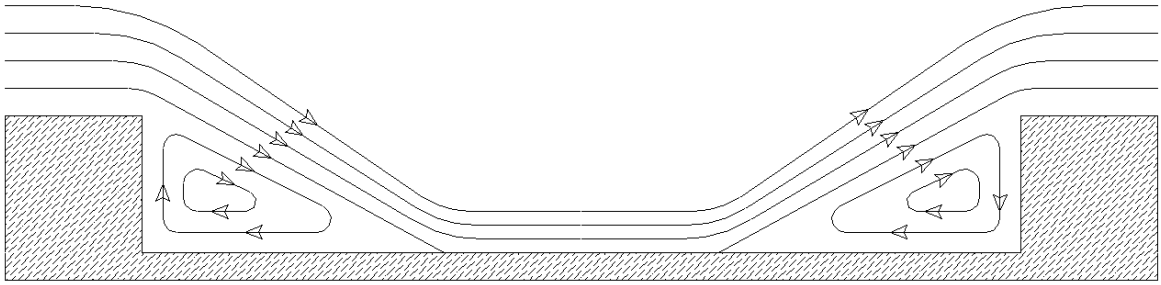

Figure 4. Flow down a step and flow up a step put together.

If now, both steps start to approach the ratio D/L will increase and both stagnation points will get closer and closer until they reach the limit condition in which both stagnation points are coincident (Figure 5).

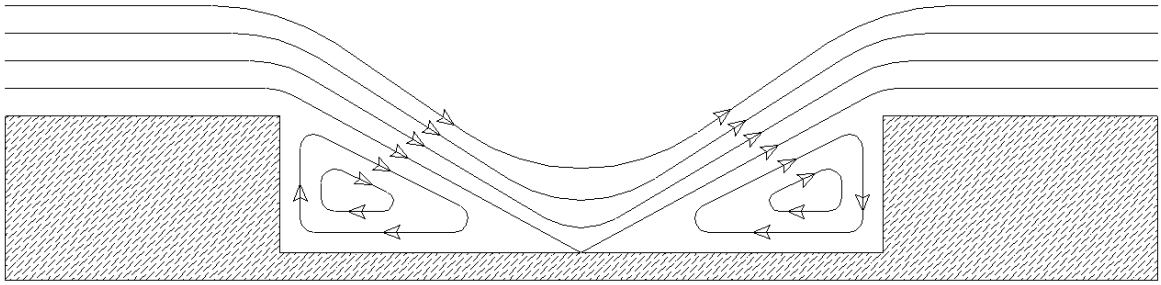

Figure 5. Coincident stagnation point.

Beyond that point, if both steps approach even more, a strong backward flow will develop from the upstream high pressure zone to the downstream low pressure zone, giving birth to a big recirculation (Figure 6) area inside the cavity (6). A similar effect would take place if, instead of making the cavity shorter, it were made deeper or the flow faster.

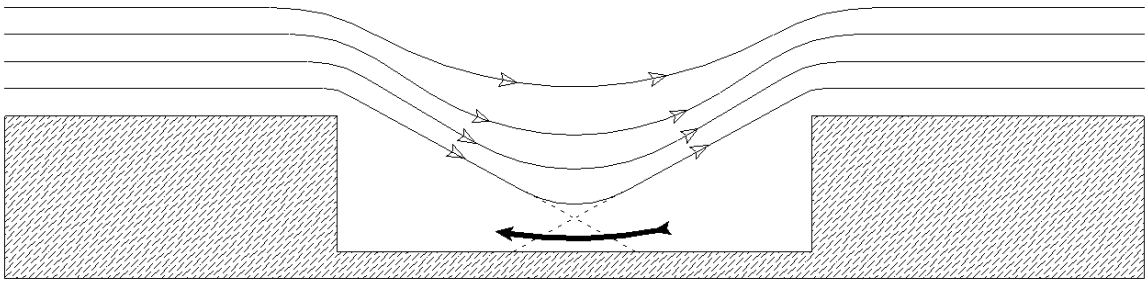

Figure 6. Appearance of Reversed Flow

Involved Variables

The main variables that affect the fluid-dynamical pattern are the length of the cavity, its depth, the incoming flow velocity and the incoming boundary layer momentum thickness. The ratios between the cavity dimensions (L/D) and (L/w) and the ratios between its length and the incoming boundary layer momentum thickness (L/θ) are the most important non-dimensional relations. While, the values of p_{rms}/q_∞ , Re_θ, M_∞ and the boundary layer shape factor $H = \delta^*/\theta$ are important flow parameters (7).

L: Cavity length D: Cavity depth w: Cavity span
θ: Boundary Layer Momentum Thickness
p_{rms} : Pressure root mean square
q_∞: Free stream dynamic pressure
δ^*: Displacement thickness of the upstream boundary layer
M_∞: Free stream Mach number

Other factors, such as the turbulent or laminar condition of the incoming flow, or the presence of modified edges or control devices, are capable to strongly influence the flow characteristics.

3.5 Identification of the problem

When a cavity is opened in an airplane the pressure fluctuations may be amplified by resonant systems, producing dangerously high pressure peaks. Resonant tones can reach 170dB sound pressure level (8), corresponding to rms pressure amplitudes of 6300Pa. This *cavity flows* problem has a close relationship with the periodicity of certain phenomena observed in the flow. The periodicity, which can be detected as a high peak in the velocity spectra, is coincident with the generation of high pressure and acoustic emission peaks.

We must wonder, then, which is the origin of the observed periodicity. In 1964 Rossiter (3) performed several experiments which allowed him to observe that in shallow cavities (L/h > 10) the fluctuations were random. As the cavity became deeper some peaks appeared in the spectra showing periodic pressure fluctuations superimposed to the random ones. For even deeper cavities (L/h < 2) the periodic component prevailed.

Based on those studies, Rossiter proposed a mechanism to explain the physical origin of the periodic phenomena. This mechanism has counted with widely acceptance in the scientific word until our days. The, so called, *"Rossiter Mechanism"* (Figure 7) is formed by four well defined steps, that repeat in a feedback cycle. We will describe them in accordance to Panickar et al. (9):

- **Amplification:** The Kelvin-Helmholtz instabilities, naturally present in the shear layer, grow up giving birth to vortices, which are convected downstream.
- **Interaction:** The convected vortices travel downstream and impinge the trailing edge of the cavity, generating acoustic instabilities.
- **Feed-back:** The acoustic instabilities propagate upstream.

- **Receptivity:** The acoustic instabilities trigger the shear layer instabilities generating a new vortex.

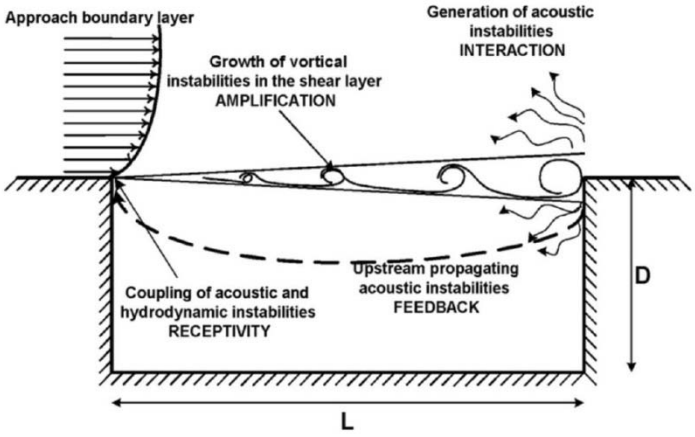

Figure 7. Rossiter Cycle (9)

The time elapsed between the generation of a vortex and its impingement on the trailing edge of the cavity, plus the time taken by the acoustic instabilities to propagate upstream and trigger a new vortex, defines the total time between two successive vortices. In other words, this defines the frequency of the whole Rossiter cycle.

The four steps previously described take place in a regular time, giving the whole cycle its characteristic periodicity.

It is easy to see how this model explains the influence of the cavity length and the flow velocity (3.4) on the frequency. A larger cavity will increase the time taken to the vortices in completing their travel downstream, as well as the time taken to the acoustics instabilities in completing their travel upstream, resulting in a diminished frequency. It is equally easy to see that an increased flow velocity will diminish the vortices travel time, without an important modification of the acoustic instabilities travel time, as they can travel by the inside of the cavity. On the basis of this facts and some previous studies made by Powell (10) (11), Rossiter introduced a simple empirical formula to predict, the frequencies at which the peaks in the spectra will appear (3).

$$S_T = \frac{fL}{U_e} = \frac{n - a}{M + \frac{1}{k}}$$

where S_T is the Strouhal number, f is the frequency, L is the cavity length, U_e is the free stream velocity, n is the modal number, M is the Mach number, k and a are respectively the mean velocity of convection of the vortical disturbance in the shear layer and the phase delay. Typically $k = 0.57$ and $a = 0.25$ (3).

The Rossiter model and its further developments (see Rockwell and Naudascher (12)) predict, hence, the dominant frequencies of the cavity acoustic feedback mechanism, when the flow is in the shear layer regime.

A good example of the effects of the Rossiter cycle is provided by Haigermoser (13). We can observe a large peak in the spectra corresponding to a St_L=0.95. Es second peak corresponding to St_L=1.9 is also observed.

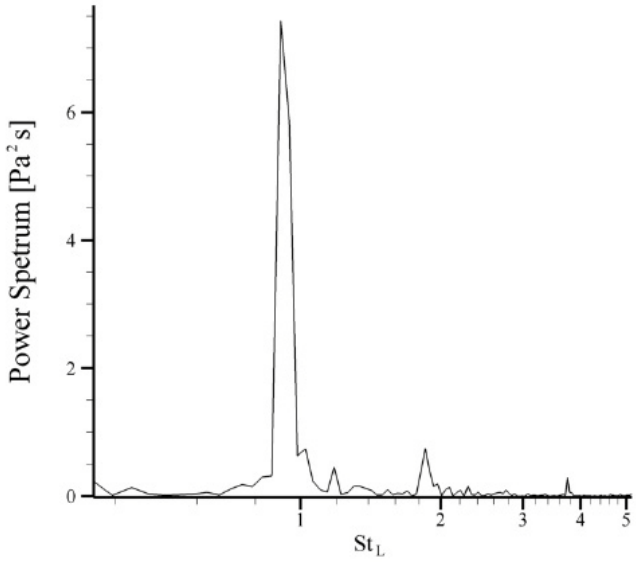

Figure 8. Example of Pressure Power Spectrum by Haigermoser

3.6 Importance of the frequency prediction

One of the most dangerous situations involving Cavity Flows is the case in which a Rossiter frequency equals one of the natural frequencies of the cavity. That *resonance* situation would produce a huge amplification of the oscillations, leading to severe structural damage, payload damage, onboard electronic devices malfunction and passengers injure. Since the pressure waves are spatially correlated fatigue is a very common result. In less

dramatic situations Cavity Flows are, also, an important source aerodynamically generated noise and drag.

Controlling acoustic tones is closely coupled with flight vehicle drag and store separation characteristics. The aerodynamic drag on cavities was measured by McGregor & White (14) to be 250% higher during acoustic resonance than under non-resonant conditions.

The difference between a good design and a bad design could result in: important efficiency loss due to an increased drag, bothering comfort diminishing due to vibration and noise and severe structural damage due to pressure peaks and other aerodynamic forces.

According to Steinburg (15) the effects of acoustic noise on electronic equipment can be of two different types: Outright failure due to physical breakeage (fatigue failure) and the microphonic effect. The last one is originated when a component is sensitive to acoustic levels due to the change in size (volume) of a device, which in turn changes its the electrical properties.

3.7 At very low Mach numbers

It should be noticed that he nature of the self sustained oscillations in cavities at very low Mach numbers has been object of debate. Tam and Block (1978) (16) claimed that at very low Mach numbers the cavity physics is dominated by normal mode resonance. If this were the case, their model would predict, in the present experiment, oscillations at very much higher frequency (see Fig. 18 in their paper). More recently Chatellier et al. (2004) (17) argued that the self-sustained oscillations, in very low subsonic flows, can be a direct consequence of the natural instability of the cavity shear layer, strongly enhanced by the presence of the cavity downstream edge. In this case, the feedback process is a quasi immediate consequence of the hydrodynamic disturbance occurring at the downstream edge. This mechanism was defined as fluid–dynamic oscillation mode in Rockwell and Naudascher (1978) (12) review, where the Rossiter mechanism was defined as a longitudinal fluid-resonant mode.

It should, finally, be observed that the cavity flow is a complicated dynamical system and, due to the amount of geometrical and physical parameters involved, many points about the mechanism of self-sustained oscillations are still to be understood.

3.8 Spanwise fluctuations

The shear layer instability leading to cavity resonant conditions is not the only instability mechanism observed in cavity flows. Direct numerical simulations of compressible flows over open cavities of aspect ratio of 2 and 4 led by Brès and Colonius (18) showed a three-dimensional instability mode having a spanwise wavelength of approximately one cavity depth. These authors found that this mode oscillates with a frequency about one order of magnitude lower than the Rossiter instabilities, experiencing non-linear interactions with the shear layer oscillation. Low frequency spanwise modulations and spanwise structures have been also observed in previous experimental and numerical studies on open cavity flows (19) (20). The origin of these three-dimensional unsteady flow cavity motions is not yet completely understood.

Chapter 4

FLOW CONTROL

4.1 Generalities of Flow Control

We call flow control "*any mechanism or process able to make the flow in the neighborhood of a solid body behave differently than it would behave in its absence"* (21).

This concept is clearly described by Flatt (22) in relation to boundary layer control, but can be extended to all type of flow control. Prandtl in 1904 (23) was a pioneer of the modern concept of flow control. He presented his work in the 3rd International Congress of Mathematicians in Heidelberg, Germany, describing the Boundary Layer Theory, explaining the steady separation mechanisms and opening the way to understand the viscid fluids flow. He also described some experiments involving boundary layer active control. Despite the good works of Prandtl, in the following three decades aircraft designers accepted that lift and drag forces had predetermined values that could not be modified (24). These concepts started changing receiving a strong impulse in Germany and in the U. S. A. before and during the Second World War. Flow control involves passive and active devices able to provoke a benefic change in wall flows and free shear flows. Passive systems do not require external energy while active ones do. Some authors consider more convenient to call the passive system *Flow Management* (25), instead of *Flow Control.*

In general, the objectives of Flow Control consist, according to the convenience, in delay or advance the turbulent transition, suppress o increase the turbulence, prevent or provoke the flow separation, with the purpose of reducing the aerodynamic drag, increase the lift, increase the flow mixing, induce noise reduction by fluid-dynamic methods.

In this context it is possible to define five eras in the development of the flow control art and science: empiric age (before 1900), scientific age (1900-1940), Second World War age (1949-1970), energetic crisis age (1970-1990) and the current age (after 1990). In this way

the works of Prandtl are the origin of the scientific method for the study of flow control. In fact, this method stopped being a test and error one, giving place to the physic scientific thought in the choice of the control devices.

Since 1990, bibliography on flow control devices has been in constant augment, in particular, researchers centered their efforts in the coherent structures manipulation , in the transition and in turbulent shear flow control (26) (27). Advances in chaos control theory, the development of micromachines systems (MEMS) and neural networks has contributed to those efforts (28) (29) (30) (31).

According to Cattafesta (7), Flow Control approaches can be classified as follows:

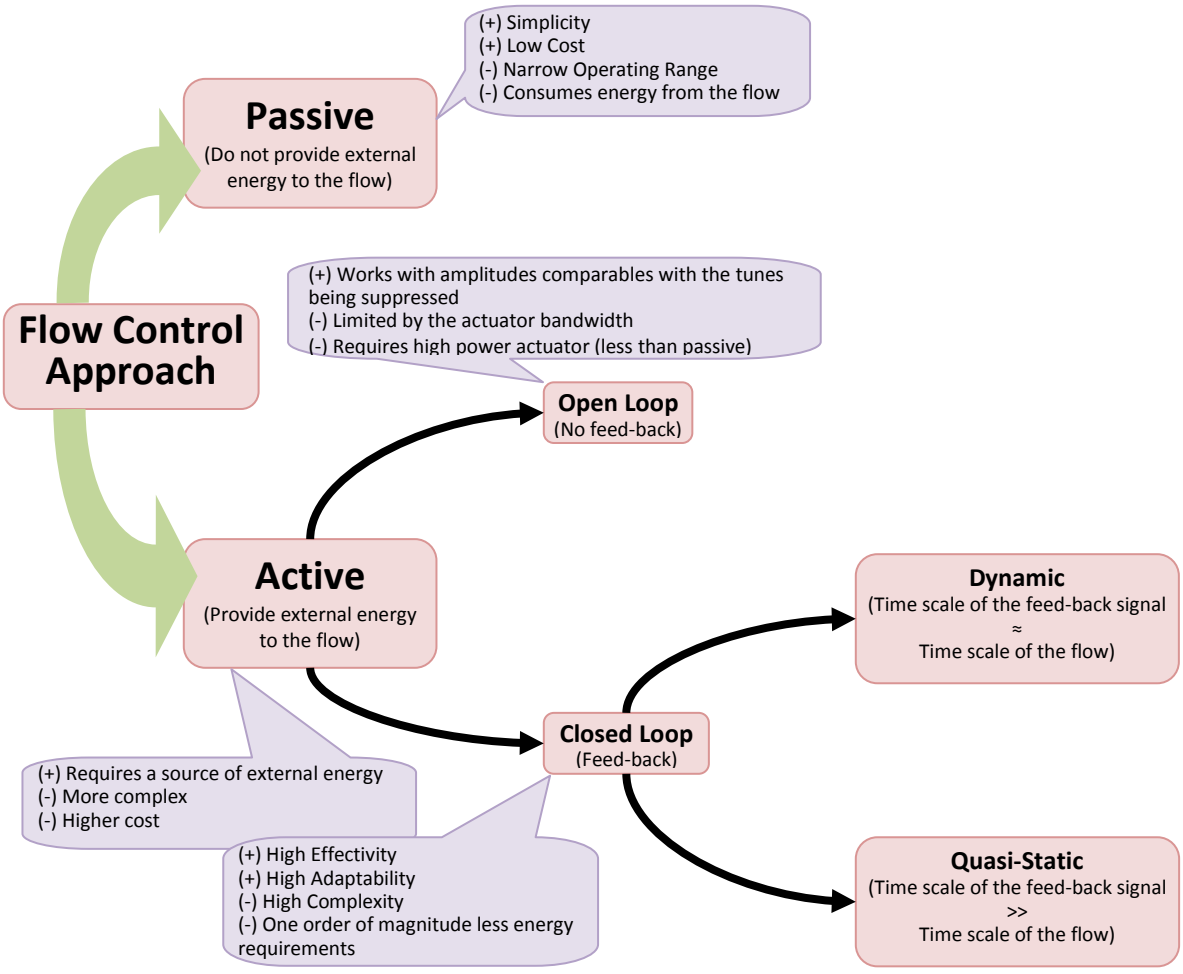

Figure 9. Flow control classification

4.2 Cavity Flow Control

4.2.1 Objectives of Cavity flow Control

In 2006 Rowley and Williams (32) defined the key goals of cavity flow control techniques in the following manner: “To suppress the acoustic tones to background sound pressure levels, over a range of flight conditions, with the smallest possible actuator requirements, resulting in reduced drag and possibly enhanced store separation characteristics”. Prevention of damage by periodic pressure peaks and comfort should be added to that definition.

4.2.2 Basic Cavity Flow Control Techniques

Different methods have been developed to cancel the undesired effects of cavity flows, obtaining different levels of success. The three most common suppression techniques and the physical method they are based on are briefly mentioned below, before discussing the frequency forcing techniques.

Still Flaps and Spoilers

These are the most widely used techniques in the industry. Steady flaps and spoilers are typically placed in the leading edge of the cavity to give a vertical component to the flow velocity, displacing the shear layer away from the cavity mouth. The success of these devices is partial, depending on the flow velocity and other factors.

Steady Mass Injection

Vakili and Gauthier (33) obtained significant attenuation with steady normal mass injection through variable-density porous plates upstream of the cavity leading edge. According to them the influence of mass injection on the external flow depends upon the relative momentum of the injected mass to the free stream. The purpose of mass injection was to control the thicknesses of boundary layer ahead of the cavity and the cavity shear layer

In general, in the steady mass injection method a jet is injected close to the cavity leading edge to thicken the boundary layer and the shear layer. This alters the shear layer stability characteristics and blows the shear layer off the cavity mouth, preventing it from impinging on the trailing edge. Large mass flow rates are required for this method.

Pulsed mass injection

The effects of this technique are due to both, mass injection and frequency forcing. The first effect is equal to the steady mass injection technique; while the second effect is a case of low frequency forcing that will be treated in the next item.

4.3 Frequency forcing

According to Cattafesta et al. (34) "Forcing the shear layer to oscillate at a frequency different from the Rossiter modes result in noise attenuation."

Arriving to a similar conclusion Sarno and Franke (35) stated "Forcing the shear layer at a frequency different from the Rossiter mode is a way to suppress resonance."

However, the characteristics of the oscillations can be very different and multiple methods can be used to produce them. If we consider the Frequency Rate as the parameter:

$$FR = \frac{Forcing\ frequency}{Frequency\ to\ suppress}$$

We can classify:

$$FR \geq 10\ \times Frequemcy\ to\ suppress \rightarrow High\ Frequency\ Forcing\ (HIFEX)$$

$$FR\ \approx Frequemcy\ to\ suppress \rightarrow Low\ Frequency\ Forcing\ (LowFEX)$$

The difference between these two forcing types is not trivial, Stanek et al. (36) stated the thesis that *"high frequency acoustic suppression is based upon a fundamentally different physical mechanism than low frequency acoustic suppression, and that it is this physically based difference that allows for radically higher rates of acoustic suppression"*.

4.3.1 *Low Frequency Forcing*

The basic principle of this method could be described as follows: Exciting the flow at a frequency close to the one that must be suppressed shifts the energy from the undesirable frequency to the excited one. In particular, forcing the flow at a frequency

close to the Rossiter one produces a shift of the corresponding Rossiter spectral peak to the forced frequency.

According to this thesis, a valid way to avoid resonance situations due to Cavity Flows would be to excite the shear layer at frequencies close to the natural frequencies in order to prevent the coincidence between a flow frequency and any natural frequency.

This method, which looks simple at first, presents several inconvenients. First of all, Rossiter frequencies are not constant for a given cavity; they vary as the flow velocity is changed. This circumstance makes necessary to excite different frequencies, according to the incoming flow velocity and, to do that, it is necessary to use some sort of active open-loop or close-loop system. Besides, it was seen that this technique has only a moderate success, since, when applied, smaller peaks still remain in the attacked frequencies. Moreover, a new peak appears in the excited frequency.

Some of the characteristics of these systems have been seen in Figure 9. It is easy to see that the utilization of these methods, besides requiring a source of energy, increases the system complexity with the consequent increased possibility of failure. If we wanted to apply this system in an airplane, it would be necessary to excite the flow at a different frequency for each flight condition. Besides, if it were necessary to suppress more than one frequency at a time, one device would be necessary for each frequency. The most frequently used devices in these cases are leading edge flaps and spoilers.

McGrath and Shaw (37) studied hinged flaps oscillating at frequencies up to 35Hz. They were successful for a limited bandwidth. Much later Cattafesta (34) studied a six-element piezoelectric flap array flush mounted at the leading edge of the cavity. The bandwidth of the actuators (300Hz.) was close to the cavity tones. The system produced a disturbance that was large enough to prevent the growth of the natural cavity disturbances. It was capable to suppress the cavity tone.

The ideal situation would be to have a simple, economic and light method which does not add extra possibilities of failure.

4.3.2 High Frequency Forcing

According to Stanek et al (36) HIFEX corresponds to forcing the flow with frequencies about an order of magnitude larger than the resonant tones.

In 1996 McGrath & Shaw (37) were the first to demonstrate “high frequency” acoustic suppression in a cavity. They placed a cylinder in the upstream subsonic boundary layer,

obtaining substantial reductions of both the cavity tones and the broadband level. They called this system High Frequency Tone Generator (HFTG). They considered that high frequency forcing due to shedding or "the cross rod in cavity flow" was a specially promising flow control device, and further research and improvements should be done on it.

In 1998, Shaw (38), testing in an advanced fighter model weapons bay, failed to produce any meaningful suppression at supersonic conditions. After this his research project was cancelled, and powered low frequency techniques were used instead.

The experiments of Wiltse and Glezer (39) in 1998 demonstrated that by forcing at relatively high frequencies, it is possible to drain energy out of low frequencies, and dump this energy into high frequencies. Based upon those experiments Alan Cain (40) proposed his thesis that the mechanism described in Wiltse and Glezer (39) could be used as a very effective cavity acoustic suppression technique.

Stanek et al. (36) continued doing a lot of work in high frequency acoustic suppression. They were the first to demonstrate very high levels of acoustic suppression in cavities at supersonic conditions. The rod in crossflow produced dramatic suppression results at subsonic and supersonic conditions. This work triggered the rapid growth of this new flow control area as the technique showed to be robust, worked well and required no sophisticated closed-loop control.

4.3.3 Comparison between LowFEX and HIFEX

A comparison between Low Frequency Forcing and High Frequency Forcing strongly supports the Stanek's hypothesis, that they both invoke different physical mechanisms, and so, they are capable to induce dramatically different effects (see Table 1).

LowFEX	HIFEX
Forcing the flow at a frequency of the same order as the frequency to suppress.	Forcing the flow at a frequency one order of magnitude larger.
Regular levels of suppression.	High levels of suppression.
The forcing frequency generates itself a peak in the low frequency region and is a source of unwanted noise.	All the frequencies in the low region are cancelled.
It is necessary to force one individual frequency to suppress each unwanted frequency.	Exciting just one high frequency, all the low frequencies are cancelled.

When the flow Mach number changes the unwanted frequencies changes and the forcing frequencies must be adapted.	Are useful for all flow conditions.
Large coherent structures remain, impinging on the trailing edge and being an important source of noise.	All large coherent structures are eliminated.
Can excite amplified instabilities in the flow in the sense of Ho and Huerre (41).	The frequency is too high to excite amplified instabilities in the flow (41).

Table 1. Comparison between LowFEX and HIFEX (based on Stanek en al. (42))

4.3.4 Theories on the Physical Fundamentals of HIFEX

In a first moment it was necessary to discard the possibility that the suppression were due to other effects produced by the control devices, instead of being due to the HIFEX itself. In the case of "pulsed mass injection" it was necessary to demonstrate that the effect attributed to high frequency forcing was not caused by the mass injection. While, in the case of the rod it should be discarded that the suppression were not due to its direct interaction with the flow. In that order Panickar and Raman (9) performed an experiment using a rod covered with a thin spiral filament to avoid the Von Karman vortex shedding. The non shedding rod did not have any suppression effect.

Regarding those results it is possible to assure that: ***"The High Frequency Forcing is the real cause of the pressure peaks suppression effects."***

a) Direct interaction

In an early work from 1996, McGrath and Shaw (37) considered that the suppression effects of the rod were due to the direct interaction of the vortex shedding with the Shear Layer instabilities. In the same fashion other authors stated that the rod itself would interact directly with the Boudary Layer. As we will comment later this hypothesis was discarded by Panickar and Raman (9)

b) Alteration of the impingement region

Ukeilei et al. (2002) (43) presented experimental evidence that the cylinder lifts the shear layer and causes the impingement region to be altered, affecting the pressure wave source region and consequently interrupting the feedback loop responsible for the cavity self-sustained oscillation phenomenon

c) Reorganization of the vorticity field in the shear layer

Stanek et al. (2007) numerical simulation (44) shows that the initial spanwise coherence and the successive breakdown of the pair of opposite sign vortical structures produced by the rod lead to a dramatic reorganization of the vorticity field in the shear layer. The authors argue that this specific vorticity reorganization is responsible for the observed stabilization, leading to the tone suppression.

d) Stability

It has been known for quite some time that free shear layers are receptive to a specific range of perturbation frequencies (a range where the shear layer will amplify a small perturbation), and that outside that range, the shear layer will not amplify the perturbation input. The growth of instabilities in a shear layer based upon a perturbation within this "receptive" range is the basis for a large body of work in flow control (45) (46) (41).

Stanek et al. (42) (2002) offered a new model for high frequency forcing. They stated that high frequency forcing alters the stability characteristics of the mean flow in the shear layer such that the growth of the large scale disturbances is inhibited or prevented.

e) Excitation of non amplified instabilities

Panickar and Raman (2008), on the basis of measurements in the shear layer and linear stability calculations based on experimental data, proposed a new model to explain cavity resonant acoustics suppression using high frequency excitation. According to this model, acoustic suppression is brought about by introducing high frequency excitation into the shear layer. This excitation frequency has to be high enough to lie outside the envelope of amplified instabilities such that a dominant part of the energy of the excited flow is contained within this frequency. This spanwise coherent, high frequency excitation introduced by the rod in cross-flow just upstream the cavity leading edge decays rapidly as it is convected downstream along the shear layer.

f) Energy cascade

Wiltse & Glezer (39) argue that the direct excitation of small turbulent scales in the shear layer accelerates the energy cascade. Following the same line Stanek et al. (36) attributed the suppression by high frequency forcing to an accelerated energy cascade in the conservative part of the energy spectra, stimulated by the excitation. This accelerated cascade is accompanied by the elimination of all large coherent structures in the shear layer, reduction in the size of the smallest identifiable coherent structures and increase of the viscous dissipation rate.

In 2000, 2001 and 2002 Stanek showed experimental evidence suggesting that forcing the shear layer at high frequencies induces an acceleration of the conservative energy cascade.

Chapter 5

EXPERIMENTS

In order to evaluate the physical mechanism underlying the self sustained oscillations suppression by high frequency forcing, several cavity flow configurations were tested. Models with variations in the cavity length, in the position of the rod and in the flow velocity were tested until a configuration was found in which the studied phenomena was most evident and clear. All the results shown in this work correspond to this "best" configuration, which is described immediately below.

5.1 Experimental setup

Planar PIV time-resolved experiments were carried out in a water tunnel (see 5.1.2) at the Politecnico di Torino. Figure 10 shows the cavity model in the tunnel test section. The cavity depth (D) was 10mm, the cavity length-to-depth ratio (L/D) was 3 and the incoming flow velocity $U_\infty = 0.31$m/s.

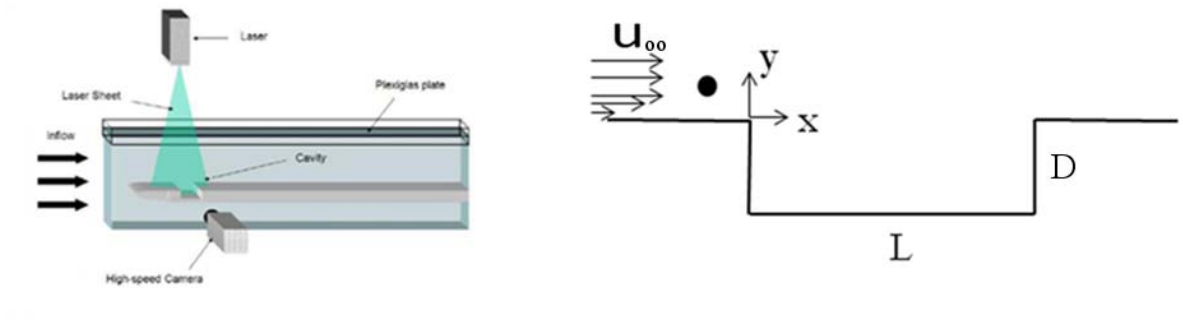

Figure 10. Sketch of the Experimental Setup and the coordinate reference system.

5.1.1 The PIV system

The PIV system is basically composed by three parts: (1) a Spectra-Physics Argon-Ion laser with a maximum emitted beam power of 6 Watt (2) a Dantec MK III CMOS camera with a resolution of 1280x1024 pixels and a maximum recording rate at full resolution of 1000 fps and (3) the hollow glass spheres with a nominal diameter of 10µm with which the fluid is seeded. The laser was placed in order to illuminate the measurement plane with a light sheet about 1mm thick, the camera was set to record at its maximum speed at full resolution covering a field containing the whole cavity and the complete shear layer up to the region of undisturbed external flow. The particle image size was between 2 and 3 pixels.

Two successive images were cross-correlated to obtain the velocity field using a multigrid algorithm provided by the DAVIS 7.2 software from LaVision, with an initial interrogation window size of 128 x 128 pixels and a final interrogation window size of 32 x 32 pixels, with a 50% overlap, applying sub-pixel refinement and window deformation. One vector corresponds to the velocity in a spatial area of 0.8 x 0.8 mm^2. Hence, one 1mm corresponds to 40 pixels.

5.1.2 Water Tunnel and Base Flow Characteristics

Experiments were carried out in the Hydra water tunnel of the Dipartimento di Ingegneria Aeronautica e Spaziale at the Politecnico di Torino. This facility is a closed loop, open flow channel, with 350mm x 500mm x 1800mm test section. The tunnel is stainless steel made; only the windows of the test chamber are made in Plexiglas. The tunnel contains about 3500 litres of water. The maximum flow speed in the test chamber (without model) is about 350mm/s.

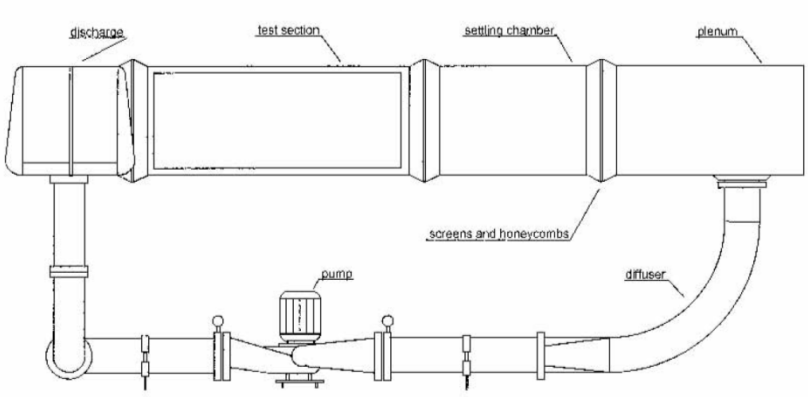

Figure 11. Hydra water tunnel scheme

The incoming boundary layer was laminar. The experimental conditions for the baseline (non-controlled) cavity flow are listed in Table 2.

Variable	Value just upstream of the leading edge	Definition
U_∞	0.31m/s	Free stream velocity
ReL	9300	Reynolds number based on L
f_{vs}	77.5Hz	Vortex shedding frequency
L	30mm	Cavity length
D	10mm	Cavity depth
ϕ	0.8mm	Rod diameter
L/D	3	

Table 2. The controlled flow experiments were carried out at similar flow conditions. Further details about the boundary layer will be seen in 6.1.6.

5.1.3 Model Geometry and Characteristics

As shown in Figure 12, a 10mm deep by 30mm long cavity was carved in the upper surface of a Plexiglas board. The leading edge of the cavity was placed 90mm downstream of the rounded leading edge of the board.

The whole model was placed in a water tunnel at a distance of 100mm from its bottom, leaving a space to permit the water to flow under the board. A special flap was placed near the water inlet to regulate the proportion of water flowing over and under the board, in order to have a null angle of attack and no recirculation bubble close to the leading edge.

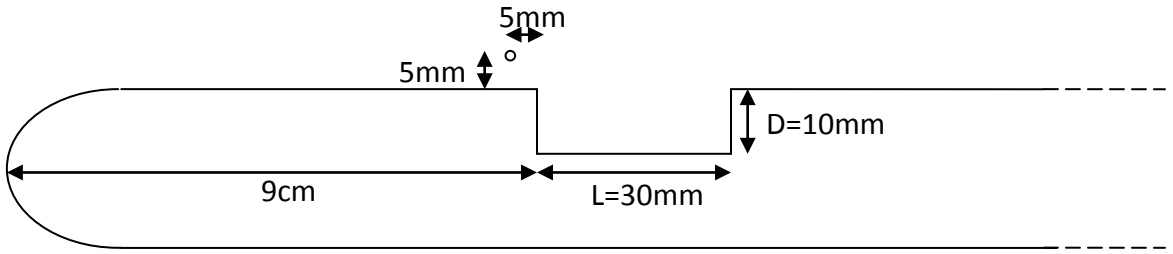

Figure 12. Cavity model sketch.

To test the controlled cavity a 0.8mm diameter (d) metallic rod was positioned at a distance of D/2 upstream and D/2 over the cavity leading edge, it will be shown later that it is clearly out of the boundary layer. The vortex shedding frequency from the rod was about one order of magnitude higher than the frequency predicted by the Rossiter formula for the baseline flow. The Strouhal number for a vortex shedding from a cylinder is derived from:

$$St = \frac{fd}{U_\infty} = 0.2$$

Then, the shedding frequency from our rod is:

$$f_{vs} = \frac{0.2U_\infty}{L} = \frac{0.2 \cdot 0.31}{0.0008} = 77.5Hz$$

It was already mentioned that, during the tests, the model was submitted to a 0.31m/s laminar water flow. For this condition a Re_L=9250 was calculated.

Applying the Rossiter equation the frequencies of the first four modes were calculated:

Mode	Frequency	$St = \frac{fL}{U_\infty}$
1	4.56Hz	0.44
2	10.06Hz	0.98
3	16.7Hz	1.61
4	22.8Hz	2.2

Table 3. Rossiter frequencies for the four first modes and their corresponding Strouhal numbers.

5.1.4 Coordinate System Definition

At this point it will be useful to define a default coordinate system for our model. In this three dimensional X-Y-Z system the axes are orientated as follows:

- X: Parallel to the cavity floor, following the streamwise direction.
- Y: Normal to the cavity floor.
- Z: In the spanwise direction orientated to form a right-handed coordinate system with X and Y. In other words, if we look at the cavity from the top with the free stream flowing upwards, in the image the z-axis will be positive to the right.

According to the defined Coordinate System we are especially interested in the definition of the xy-plane (also called ‘normal plane’) and the xz-plane (also ‘parallel plane’).

Finally, it is necessary to define the coordinate origin location. It will be placed in the cavity leading edge on the left extreme of the image in the xz-plane (Figure 10).

5.1.5 Normal to the wall plane (xy-plane)

PIV measurements were made in a streamwise plane normal to the cavity floor, at the cavity mid-span (Figure 10). In the normal plane the visual field was a rectangle of 39mm along the x-axis and 31mm along the y-axis, covering the whole cavity and the complete shear layer up to the region of undisturbed external flow.

The laser was placed in a high position at one side of the gallery. The beam was converted into a light sheet by a special optic system before being deflected downwards by a mirror.

The camera was placed on the opposite side of the gallery at the correct distance to cover the area mentioned above. The focus was set to sharply see the particles lighted by the laser sheet.

5.1.6 Parallel to the wall planes (xz-planes)

In the streamwise planes parallel to the cavity floor, PIV measurements were made at five different levels (see Table 4).

In this case the laser sheet was deflected twice. It was first deflected downwards by a fixed mirror. Then, it was deflected to the horizontal plane again by a mirror adjustable in height, in order to be able to move the horizontal laser sheet through the four levels.

The camera was placed over the gallery, looking downwards, at the proper distance to cover a visual field of 40mm along the x-axis and 50mm along de z-axis, centered at 50% of the cavity span.

5.2 Data acquisition

Twelve time resolved series were acquired for the vertical plane test, six corresponding to the uncontrolled cavity and six corresponding to the controlled case. For the horizontal

plane five levels were measured, and twelve time resolved series were acquired for each; again, six for the controlled case and six for the uncontrolled case.

Horizontal Level	Y-Axis Position [mm]	Approximate Position
1	-4	About D/2 – Center on the downstream recirculation zone.
2	-1	Slightly inside the cavity
3	0.5	Cavity Mouth
4	3	Between the rod and the cavity mouth
5	5	Rod Level

Table 4. Horizontal Plane Measured Levels

5.3 Measurement Uncertainty

The image acquisition frame rate was 1000Hz, for all the measurements. The exposure time of each PIV image was 190µs. Since the internal memory of the camera is 4GB at 1000 frame/sec a maximum of 3272 images could be acquired, from which 3271 velocity fields could be calculated. In order to perform statistic analysis using uncorrelated data, only one couple of consecutive images every 100 images were memorized. Statistical results were then obtained using six packages of 3272 recorded images at an effective acquisition rate of 10Hz. For the time resolved analysis and for the spectral analysis, PIV images were recorded at the frequency of 1000 Hz.

The uncertainty in measuring the velocity with PIV depends mainly on the quality of the images, the particle image size, the particle image density, the displacement of the particles from one image to the successive and the velocity gradient. Since the particle image size was between 2 and 3 pixels and a good contrast between the particle light intensity and the background light intensity was obtained, according to Figure 13 the error in locating the correlation peak was estimated to be lower than 0.1 pixels (47). Taking into account a displacement of particles from the first to the second image of 12.4 pixels in the

outer flow and about half of it in the shear layer, the error in measuring the instant velocity results near 0.8% in the outer flow and is less than 2% in the shear layer.

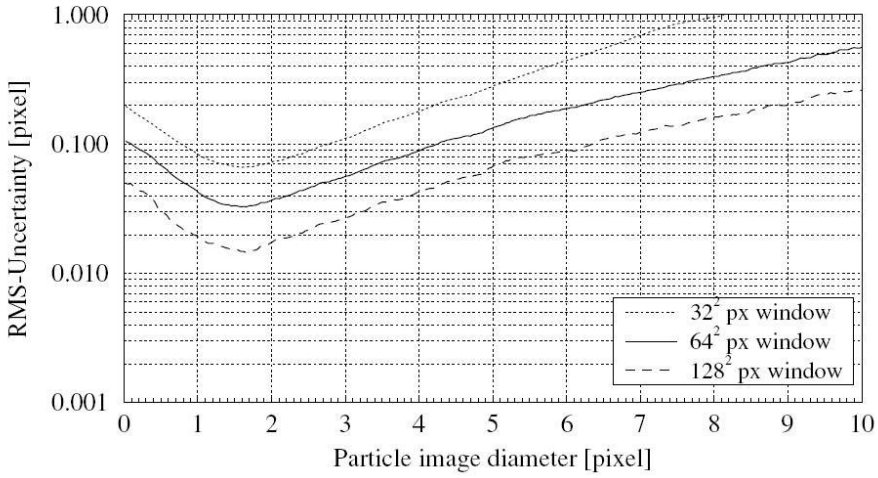

Figure 13. Measurement uncertainty in digital cross-correlation PIV evaluation with respect to varying particle image diameter, from Raffel et al., 2007 (47)

Chapter 6

ANALYSIS OF THE DATA

6.1 Normal Plane Data Analysis

6.1.1 Instant Velocity Field

Since PIV is a method to measure instant velocities, the first result that we obtained was its field. Time Resolved PIV permits us to obtain an equally-spaced-in-time image sequence from which it is possible to reconstruct the time history of the field, as a video. In our particular case, six sequences of 3272 images each have been taken, at a frequency of 1000Hz, from which 3271 instant velocity fields have been obtained.

In Figure 14 we can observe two instant images corresponding to the tests without control (left) and with control (right).

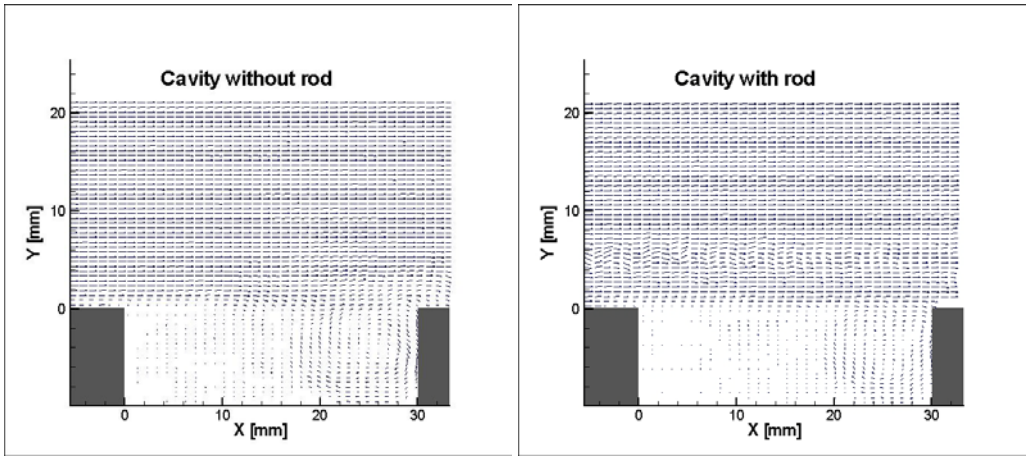

Figure 14. Instant Velocity Field – Non-controlled case (left) and Controlled case (right)

These images correspond to the raw data obtained after the PIV processing with DaVis®. In the baseline flow (non-controllled cavity) we can observe the incoming laminar Boundary Layer and the shear layer where some instabilities seem to appear, while, in the cavity with rod (controlled flow) we can also see the von Karman vortex shedding effect.

6.1.2 Mean Velocity Field

We will start our analysis of the velocity fields with a statistical analysis. Its first step will be the derivation of the mean velocity field. In Figure 15 the streamlines of the mean velocity field and a color plot of the normalized velocity modulus are reported, respectively for the baseline and for the controlled flow.

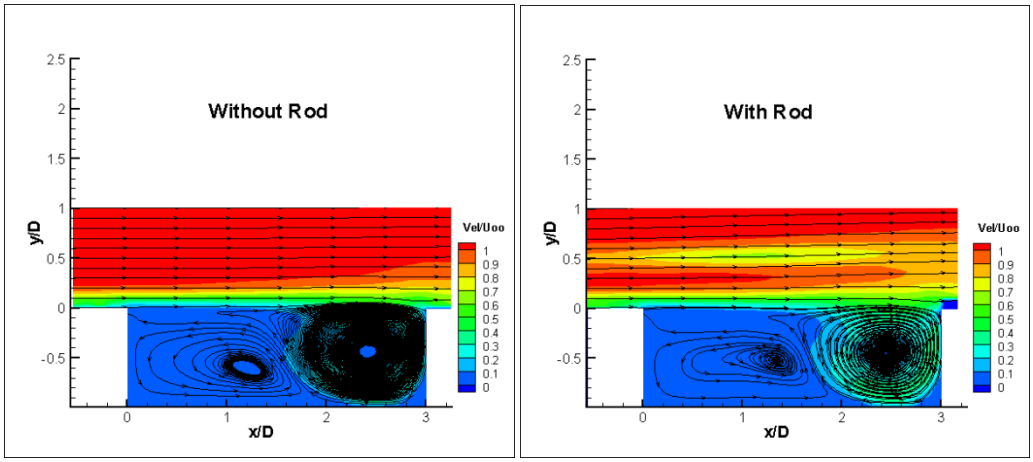

Figure 15. Mean Velocity Field for the uncontrolled case (left) and the controlled case (right).

In the non-controlled cavity flow (without rod), a large clockwise recirculation zone, covering all the downstream half of the cavity can be observed. A weaker counter recirculation zone is present in the upstream half. The Boundary Layer and the Shear Layer are clearly visible.

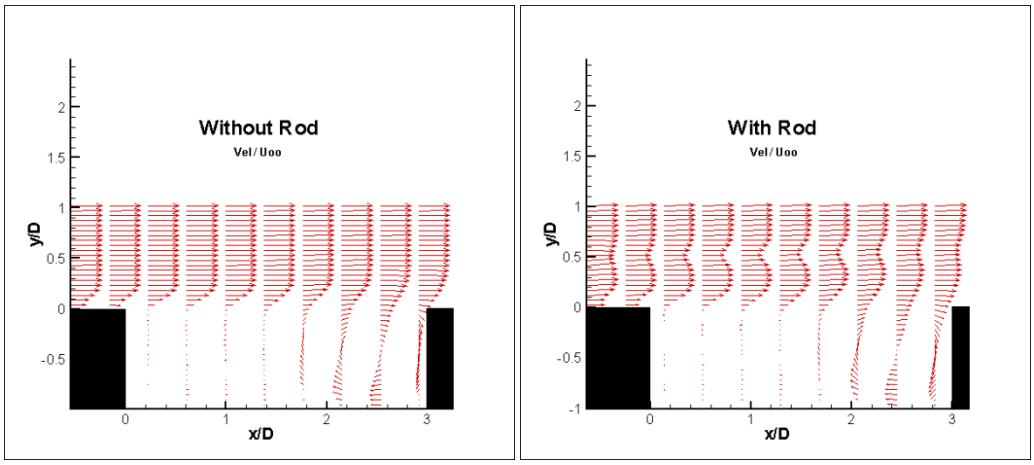

Figure 16. Mean Velocity Vectors profile

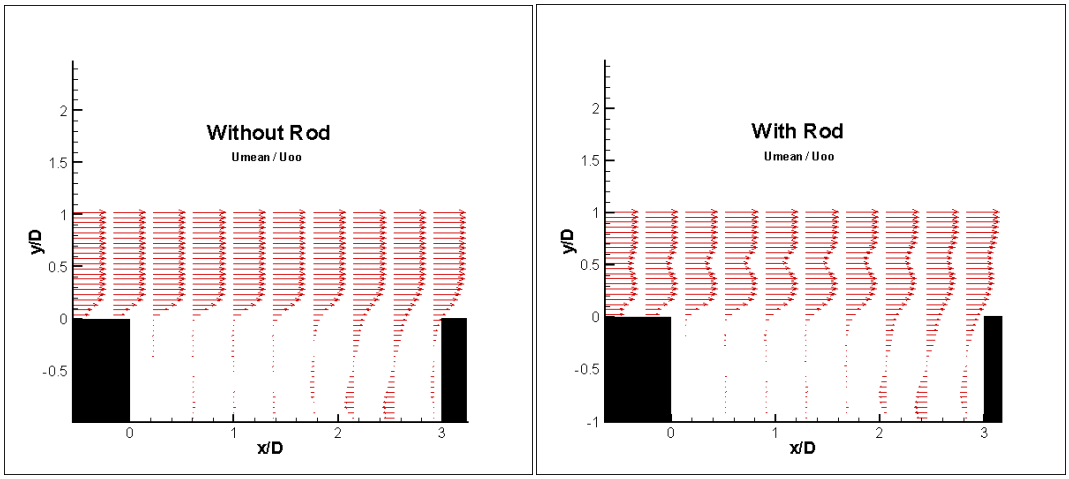

Figure 17. u-component of the Mean Velocity vector Profiles

In controlled cavity flow (with rod) all the previous description does not seem to be altered. The difference lies in the presence of the cylindrical rod wake at y/D=0.5 that is evident and produces the expected velocity defect (Figure 16 and Figure 17). The rod appears clearly situated outside of the incoming boundary layer. The fact that the flow between the wake of the rod and the boundary/shear layer assumes a velocity nearly equal to the external velocity suggests the absence of direct interference between the cylinder wake and the boundary layer.

Remark 1. *Absence of direct interference between the cylinder wake and the boundary layer.*

Special attention will be paid to the development of the shear layer (see 6.1.7).

6.1.3 Root Mean Square of the normalized fluctuating velocities

The r.m.s. values of the fluctuating velocity, normalized with the free stream velocity, give us an approach to the intensity of the velocity fluctuations in the different points of the field.

Let us consider first the fluctuation of the streamwise component of the velocity showed in Figure 18, where u'_{rms} is the root mean square of the fluctuating velocity component u'. The most evident (and certainly expected) difference observed is the presence of the vortex shedding from the rod. However, this presence *does not seem to provoke any disturbance in the incoming boundary layer*, since it looks almost similar in both images. A clear gap between the vortex shedding and the boundary layer, where the flow shows the same characteristics as in the uncontrolled case, also supports the thesis that there is no direct interaction between the rod and the Boudary Layer.

Remark 2. *The presence of the rod does not seem to provoke any disturbance in the incoming boundary layer.*

In both cases large longitudinal fluctuations appear in the incoming Boundary Layer.

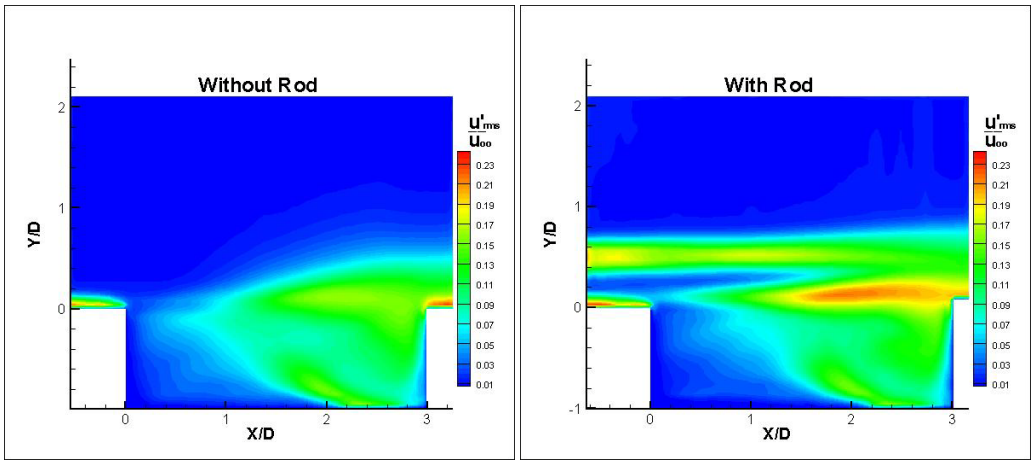

Figure 18. Streamwise component of the fluctuating velocity, u'_{rms}, for the uncontrolled case (left) and the controlled case (right).

In addition, we can observe high levels of u' in the downstream half of the Shear Layer with a peak between x/D=2 and x/D=3, which is 30% higher in the controlled case. We notice that the presence of the rod, even being placed out of the boundary layer and not having a direct interaction with it, produces, somehow, a visible effect on the downstream shear layer.

Remark 3. *…the presence of the rod, even being placed out of the boundary layer, has a visible effect on the downstream shear layer.*

The following observation is an important result, since it will be of high importance in our future analysis:

Remark 4. *The velocity fluctuations in the rod wake decay downstream, while the shear layer fluctuations grow up downstream.*

Considering now the normal-to-the-wall component of the fluctuating velocity field, v', (Figure 19), the difference between the controlled and the uncontrolled flow seems to be mainly in the wake of the rod. However, high levels of v' are also present in the downstream half of the Shear Layer with peaks between x/D=2 and x/D=3, which are 15% lower in the controlled case.

Remark 5. *While the peak value of u' increases about 30% in the controlled flow with respect to the baseline case, the peak value of v' decreases about 15%.*

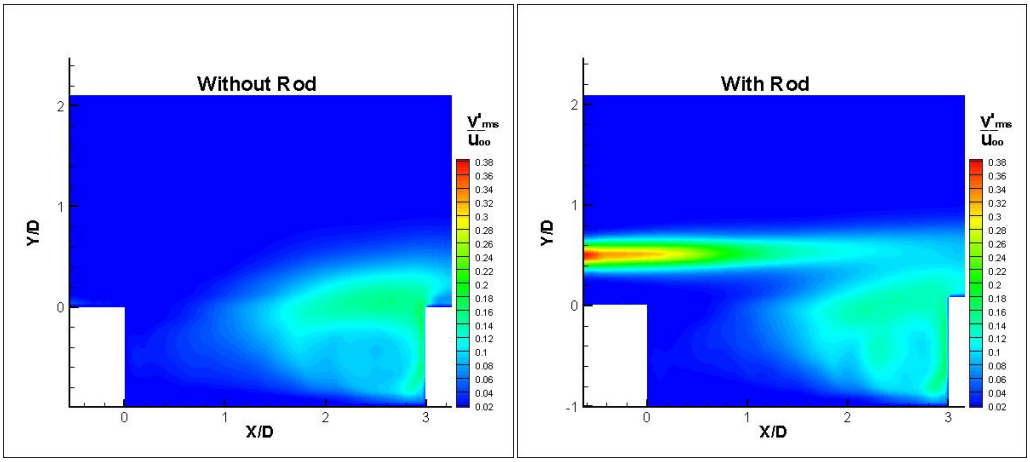

Figure 19. Wall normal component of the fluctuating velocity, v'_{rms}, for the uncontrolled case (left) and the controlled case (right).

As a general comment we can say that the overall streamwise fluctuation values are larger in the controlled cavity shear layer, while, the normal fluctuation values are smaller. As will be shown in 6.1.8 this results are in total agreement with the facts that were found in the frequency spectra. An explanation for this behavior will be introduced at section 6.1.5.

6.1.4 Mean Vorticity Field

In Figure 20 the spanwise normalized mean vorticity, $\overline{\omega_n}$, is reported for the baseline flow and for the controlled flow. High values of the mean vorticity are shown in the shear layer, in the wake of the rod and in the downstream re-circulating bubble. Anti-clockwise (positive) vorticity is evidenced near the trailing edge, induced by the clockwise (negative) bubble. In both flows the absolute value of the mean vorticity in the shear layer assumes a peak value at about x/D=0.3 in the proximity of the leading edge and then decays going downstream, assuming higher values in the case of the baseline flow. Actually, the distribution of the absolute value of the mean vorticity along the shear layer shows a reduction up to 20%, in the last 2/3rd of the cavity shear layer, for the case of the controlled flow with respect to the basic flow

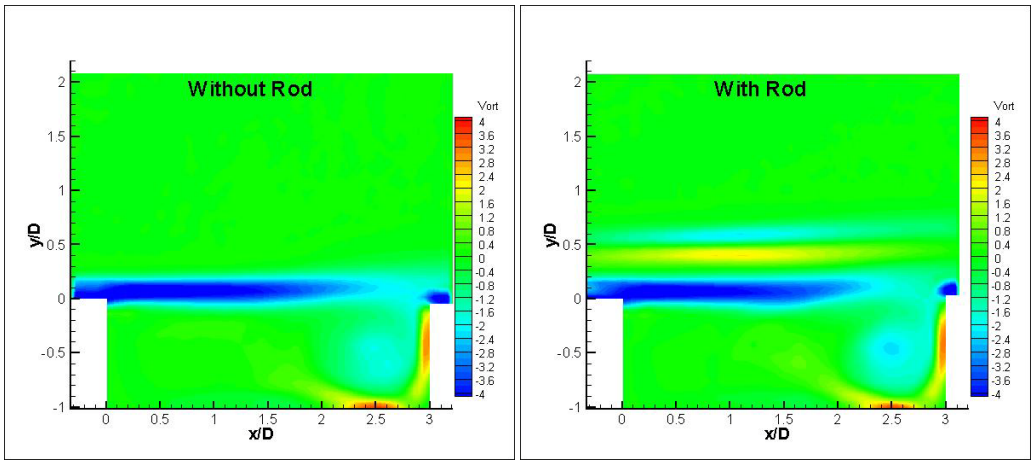

Figure 20. Normalized mean vorticity $\boldsymbol{\omega D/u_\infty}$

6.1.5 Root Mean Square of the normalized Vorticity

In the case of the controlled flow, the distribution of the root mean square of the spanwise normalized vorticity, ω_{rms}, along the shear layer, (see Figure 21), shows an increase in the upstream region (x/D≤1/3) up to about 100% and a reduction up to 15% in the downstream region. Its increase in the upstream region is due to the train of weak vortices travelling along the shear layer induced by the cylinder Von Karman wake. The presence of these vortices will be highlighted in Figure 35, in 6.1.9.

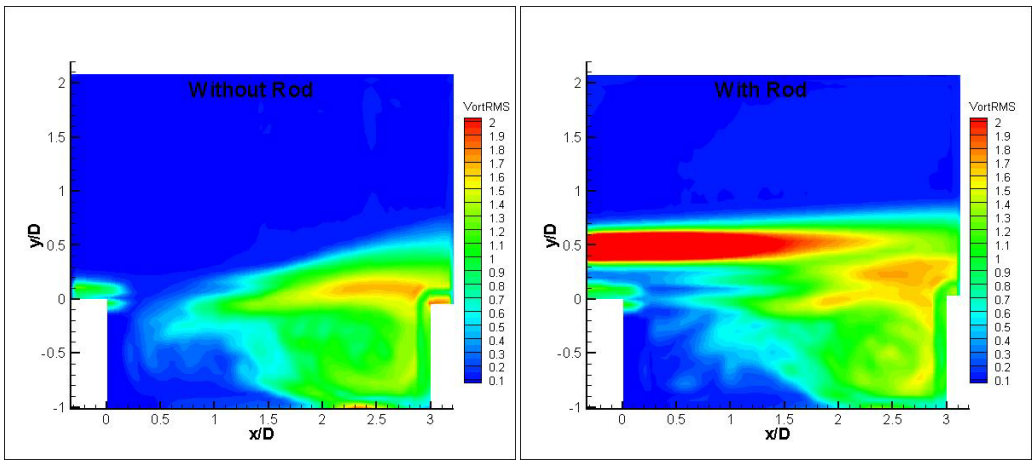

Figure 21. Normalized RMS Vorticity $\boldsymbol{\omega' D/u_\infty}$

The reduction of ω_{rms} and of the absolute value of $\overline{\omega_n}$ in the downstream region is provoked by the development of the rod wake. In fact, it has been recently demonstrated by Stanek et al. (2007) (44) numerical simulation that the initial spanwise coherence and the successive breakdown of the pair of opposite sign vortical structures injected at high frequency by the rod lead to a reorganization of the vorticity field in the cavity shear layer. In particular the vortical structures in the shear layer loose, in part, their spanwise coherence, already in the region close to the leading edge, showing consequently a new organization with their axis more often oriented in the y-direction and in the x-direction rather than in the z-direction. This effect justifies, to a good extent, the measured reduction in the mean and fluctuating spanwise component of the vorticity in the case of the controlled flow in the shear layer region. Moreover, the reduction of the vorticity absolute value in the controlled shear layer can be in part attributed to an unwind action by the positive Karman vortices in the cylinder wake lower side, as it will be evidenced later.

The early loss of spanwise coherence of the structures in the shear layer justifies also the observed reduction of the v'-component of the fluctuating velocity shown in Figure 19 for the case of controlled flow.

6.1.6 Incoming Boundary Layer

The experimental data shows that, for the non-controlled case, the mean velocity profile, measured at the cavity leading edge (x=0), fits accurately the profile predicted by the Blasius self-similar solution for laminar boundary layer (Figure 22). For the present experimental conditions the incoming boundary layers appear to be laminar.

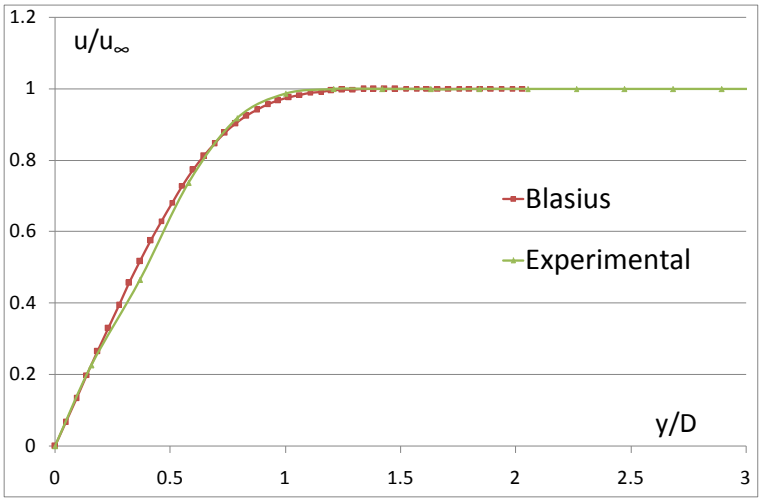

Figure 22. Incoming boundary layer in the non controlled case.

A similar velocity profile measured for the controlled cavity showed a zone of depression coincident with the level where the control device is placed (Figure 22). It can be seen that under the position of the rod (5mm) the mean velocity recovers the value that it would have in its absence, indicating that the rod does not influence in a direct manner on the Boundary Layer, being placed clearly outside of it. The effect found in the Boudary Layer is coincident with what was found by Panickar and Raman (9) at similar conditions. It should be reported here that Sarpotdar et al. (2010) (47) conducted a parametric study to optimize the gap, g, between the rod and the cavity wall, founding the optimum gap to be $g/\delta=1.14$. In the present experiment $g/\delta=2$.

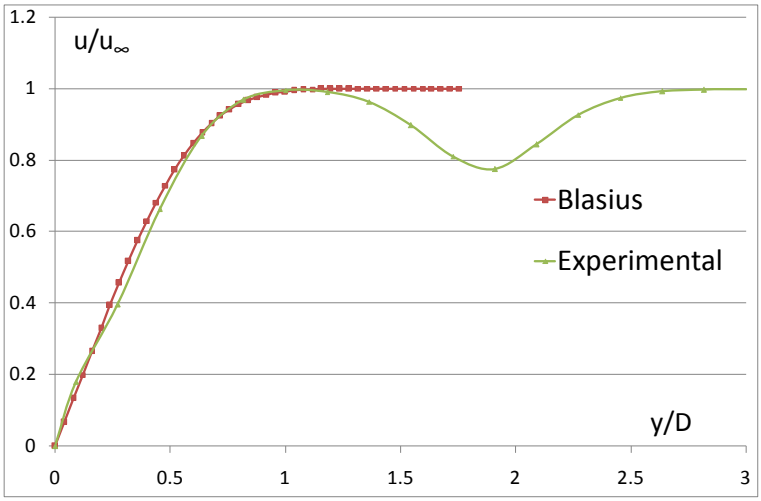

Figure 23. Incoming Boundary Layer Velocity Profile for the controlled case.

Remark 6. *This is the third result indicating that the vortex shedding does not have a direct influence on the Boundary Layer.*

It is important to remark that the velocity profiles correspond to a position in the *x-axis* downstream of the rod position, close to the leading edge of the cavity.

	Without Rod	BL at the Trailing Edge
δ	2.34mm	B. L. Thickness
δ^*	0.97mm	Displacement Thickness
$\delta^*_{Blasius}$	0.93mm	DT from Blasius equation
θ	0.37mm	Momentum Thickness
H_{sp}	2.6	Shape Factor (δ^*/θ)
Re_δ	740	Reynolds number based on δ
Re_θ	113	Reynolds number based on θ
L/θ	81	Gharib & Roshko criterion
$\frac{L}{\delta}\cdot\sqrt{Re_\delta}$	348.75	Sarohia criterion

Table 5. Boundary Layer parameters.

The ratio L/θ was 81, which is just above the $L/\theta = 80$, the threshold for the onset of self-sustained cavity oscillations, as determined by Gharib and Roshko (48). The Sarohia (49) criterion to occur self-sustained oscillations for a laminar incoming boundary layer $\left[\frac{L}{\delta}\cdot\sqrt{Re_\delta} > 290\right]$ is also satisfied. Namely, in the present experiment is: $\left[\frac{L}{\delta}\cdot\sqrt{Re_\delta} > 348\right]$.

6.1.7 Shear Layer Characteristics

The streamwise component of the mean velocity measured just above the cavity mouth is plotted in Figure 24. We can see that in both cases, controlled and uncontrolled, it remains almost equal.

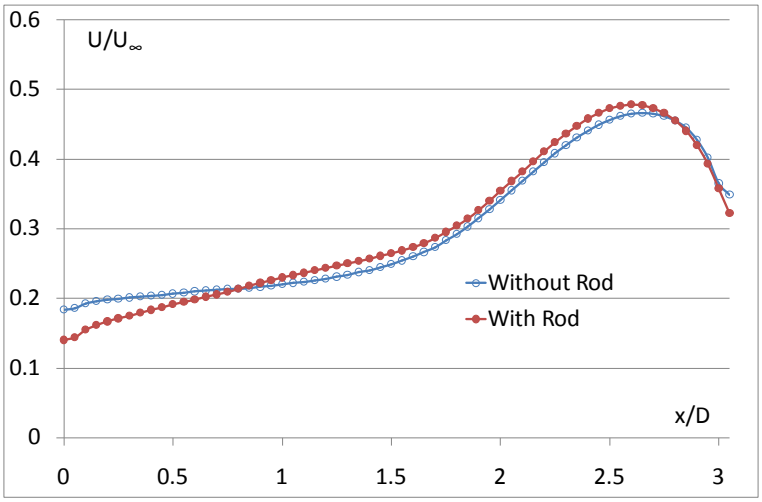

Figure 24. Mean streamwise velocity along the shear layer

The shear layer momentum thickness is considered a common measure of the shear layer growth. Its value, normalized by the initial momentum thickness, plotted in Figure 25, shows a slow increment in the first two thirds of the cavity that becomes faster in the last third. In both cases, controlled and non-controlled, this variable seems to develop in a similar way; however, in the controlled case its development is less pronounced in the last part.

$$\theta = \int_{-2.09mm}^{2.83mm} \frac{u}{U_\infty}\left(1 - \frac{u}{U_\infty}\right)$$

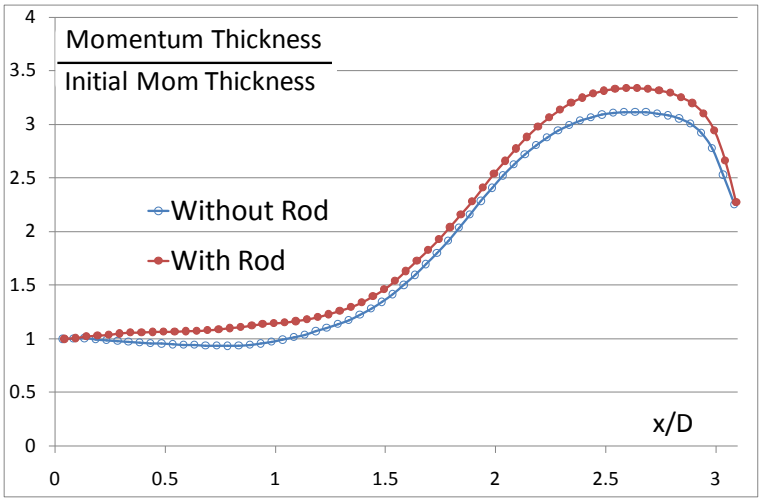

Figure 25. Shear layer momentum thickness.

The vorticity thickness is considered useful to characterize the shear layer thickness.

$$\frac{\delta_\omega}{D} = \frac{1}{\omega_{max}} \int_{-\infty}^{\infty} |\omega| dy$$

where $\omega = -\frac{\partial u}{\partial y}$

The vorticity thickness is appropriate, because modern theories of shear layers view their growth as "basically the kinematic problem of the unstable motion induced by the vorticity" (Brown and Roshko, 1974) (50).

The effect of the presence of the rod on the last third of the shear layer appears clearer in this measure (Figure 26).

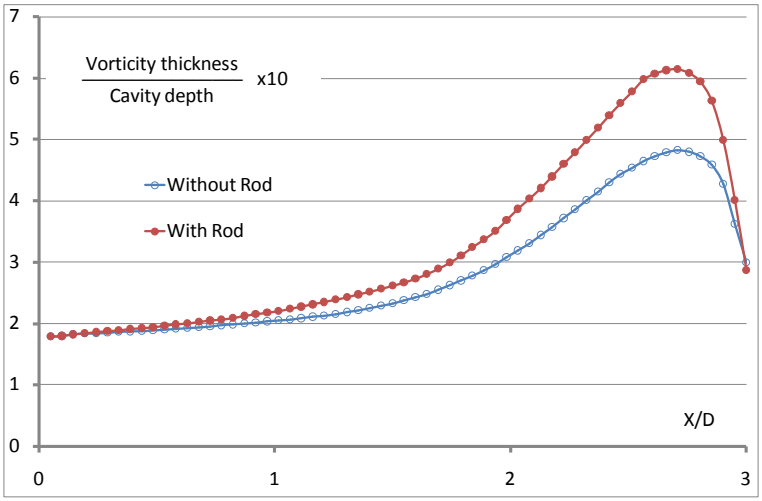

Figure 26. Shear Layer Vorticity Thickness development

Remark 7. *The presence of the rod seems to have an effect only in the last third of the shear layer.*

In Figure 27, profiles of the streamwise component of the mean velocity, at different distances from the leading edge, are reported for the baseline and the controlled flows. Reverse flow near the cavity bottom reveals for both flows the presence of the large clockwise recirculation zone in the downstream part of the cavity. The counter-rotating bubble in the upstream part that was clearly seen in Figure 15 is poorly evidenced by these velocity profiles. The wake of the cylindrical rod at y/D=0.5 and the shear layer separating from the cavity leading edge are evident, showing the expected velocity defect. It is important to observe that the flow between the wake of the rod and the shear layer assumes a velocity nearly equal to the free stream velocity, as in the baseline flow, for more that two thirds of the cavity length, suggesting the absence of direct interference between the cylinder wake and the shear layer in this region. As it is also confirmed by the profiles of the v-component of the mean velocity in lower plot of Figure 27, the rod and its wake scarcely influence the mean velocity in the cavity and in the shear layer.

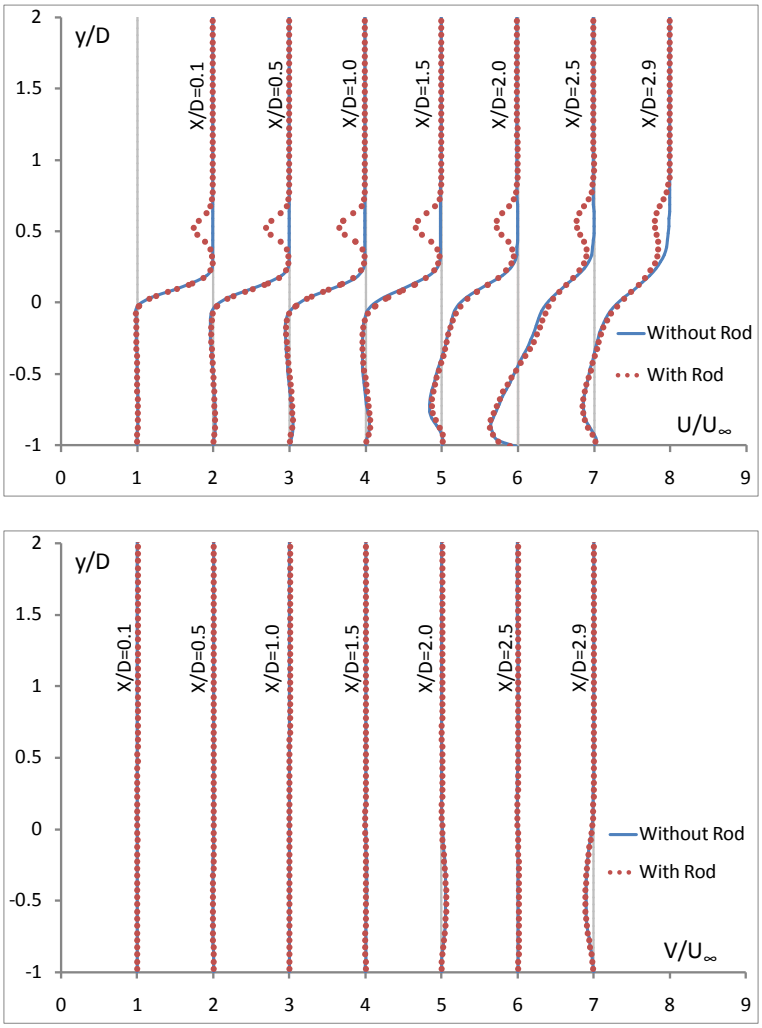

Figure 27. Normalized streamwise (U/U_∞) and wall normal (V/U_∞) mean velocity profiles at different distances from the leading edge. Each velocity profile is shifted by 1 with respect to the previous one.

Remark 8. *The wake of the rod does not seem to interfere with first two thirds of the shear layer.*

In order to understand if the presence of the rod deflects upwards the shear layer, thereby impairing the efficiency of its interaction with the aft cavity wall, as stated by Ukeilei et al. (2002) (43) (see 4.3.4b) a measure of the shear layer deflection is reported in Figure 28. The final position y_f (at x/D=2.9) of the velocity streamlines as a function of the initial position y_i (at x/D=0.05) is reported for different streamlines in the shear layer and above of the cavity. The comparison between the two flows, the basic and the controlled one, does not show an evident lift-off of the shear layer induced by the rod.

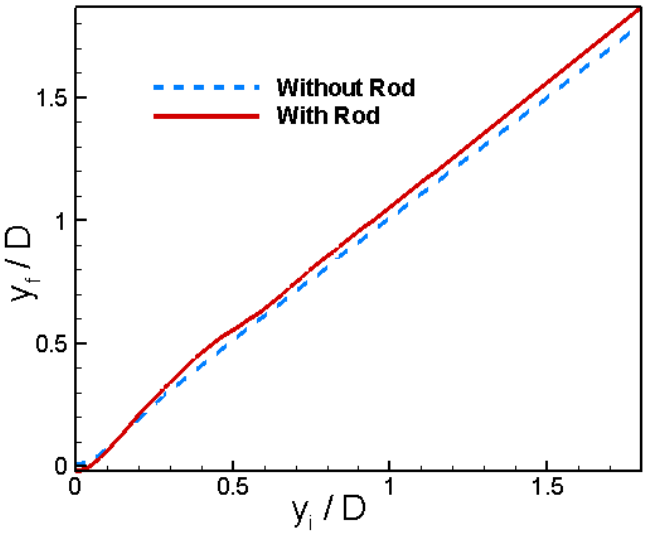

Figure 28. Final position (y_f) of the velocity streamlines as function of the initial position (y_i)

Remark 9. *No lift-off of the shear layer is observed*

A list of some important variables together with their definitions is shown in Table 6

Variable	Value just upstream of the leading edge	Definition
U_∞	0.31m/s	Free stream velocity
$\mathrm{Re_L}$	9300	Reynolds number based on L
f_{vs}	77.5Hz	Vortex shedding frequency
L	30mm	Cavity length
D	10mm	Cavity depth
ϕ	0.8mm	Rod diameter
L/D	3	

Table 6. Flow and model variables

6.1.8 Velocity Frequency Spectra

Considering that the main subject concerning the cavity flows is the presence of periodic pressure peaks, it is easy to understand that the analysis of the power spectra of the wall normal velocity is especially interesting. All periodic effect in the flow will be detected as a peak in the frequency spectrum. In particular, it will be possible to evaluate the presence or the absence of peaks at the Rossiter frequencies, and of effect of the control device on them.

The frequency spectra corresponding to six different points placed at y/L=0.06 along the cavity mouth will be evaluated.

Very close to the leading edge no frequency peak is detected in the spectrum (Figure 29). However, looking with more detail, by using a logarithmic scale, we can detect a peak at St $\cong$ 7.5 $(\mathrm{St} = \mathrm{fL}/\mathrm{U}_\infty)$ in the controlled cavity and another peak at St $\cong$ 1. The first one corresponds to the vortex shedding frequency while the second one corresponds to the second Rossiter mode (see Table 3).

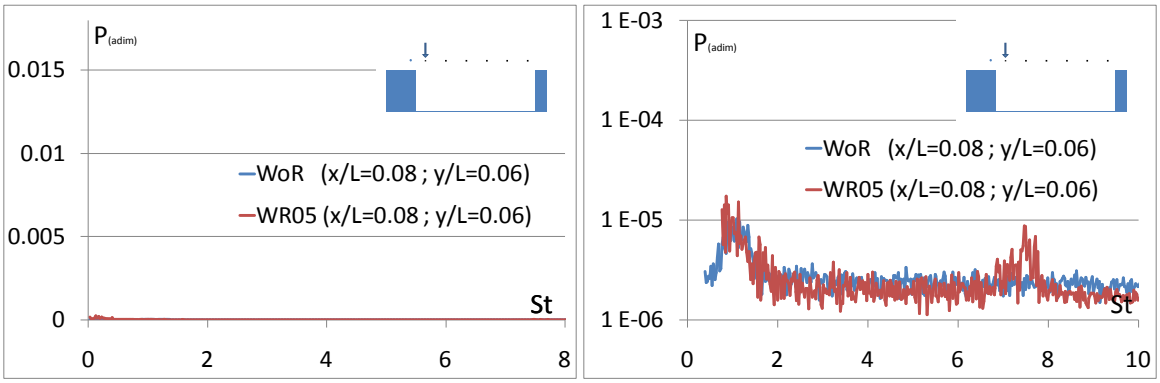

Figure 29. Non-dimensional Power Spectra $[\boldsymbol{P_{adim}} = \boldsymbol{P_v}/(\boldsymbol{u_e} \cdot \boldsymbol{D})]$ of the normal-to-the-wall velocity component (v) at x/L = 0.08 and y/L=0.06. WoR: without rod, WR05: with rod. Normal scale (left), logarithmic scale (right).

In the second point along the cavity mouth (Figure 30) the situation looks very much like in the previous case. No frequency peak is detected in the normal scale; however, using a logarithmic scale, the von Karman vortex shedding frequency and the second Rossiter frequency come out. The first one appears to be weaker, while the second appears to be stronger than in the previous point.

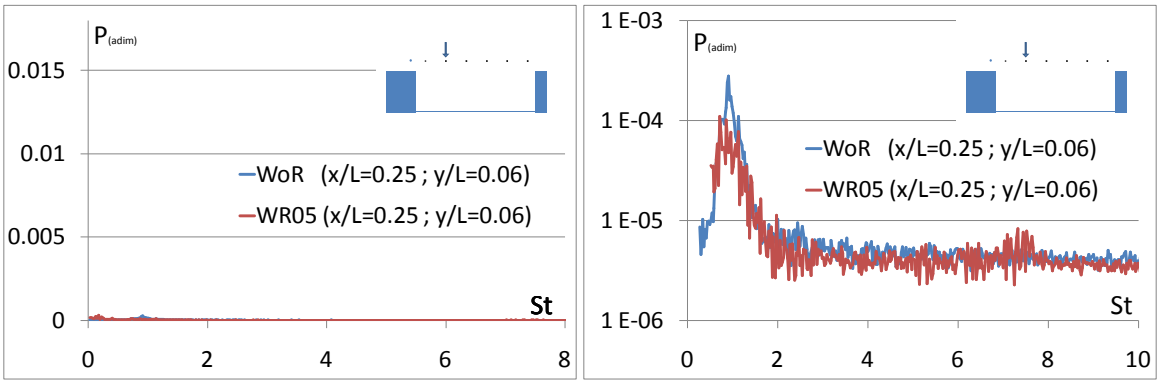

Figure 30. Velocity Frequency Spectra (v-component) at X/L = 0.25, normal scale (left), logarithmic scale (right)

In the third point, placed almost in the mid length of the cavity mouth (Figure 31), the St=1 peak is clearly visible in the uncontrolled case; however, it does not appear in the controlled case. The logarithmic scale is no longer necessary since it does not give any further information. The vortex shedding peak is not visible any longer.

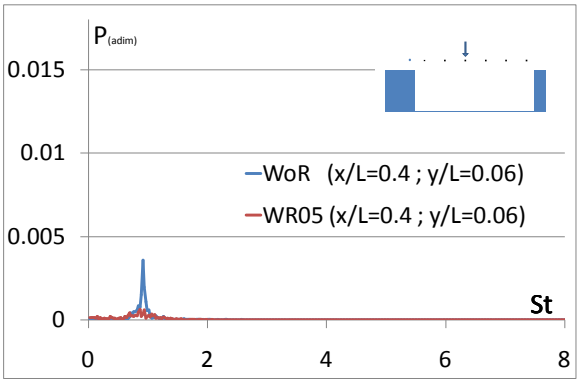

Figure 31. Velocity Frequency Spectra (v-component) at X/L = 0.4

The fourth point is located at x/L=0.55 from the cavity leading edge, just downstream from the cavity mid length. Figure 32 shows that the St=1 peak in the non controlled case gets higher than in the previous point, while in the controlled case it is almost absent. A second peak appears, at St=1.7, in the clean cavity spectrum. This frequency is coincident with the third Rossiter mode theoretically calculated in Table 3.

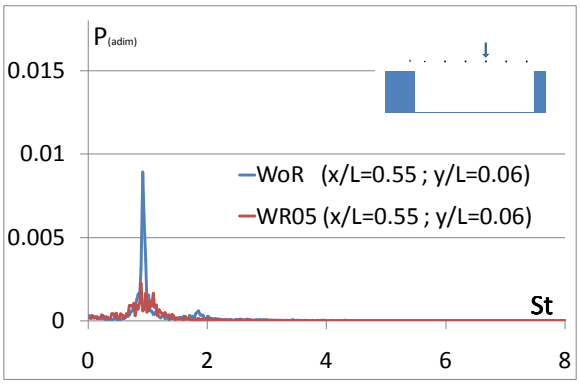

Figure 32. Velocity Frequency Spectra (v-component) at X/L = 0.55

In the fifth and sixth points both peaks corresponding to the baseline flow (non-controlled cavity) spectrum get higher than in the previous point, while the controlled cavity levels remain unchanged.

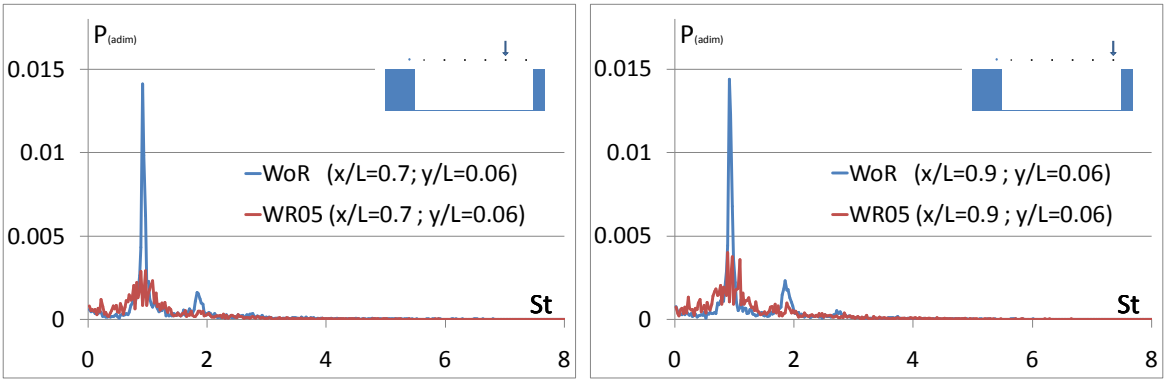

Figure 33. Non-Dimensional Velocity Frequency Spectra (v-component) at X/L = 0.7 (left) and at X/L = 0.9 (right). $\boldsymbol{P_{adim} = P_v/(u_e \cdot D)}$.

The frequency spectra are, probably, the best way to verify the presence of periodical fluctuations and the suppression capacity of a control mechanism. It is clearly seen that the rod in crossflow is able to suppress the cavity tones reducing them to broadband noise levels.

Remark 10. *The rod in crossflow is able to suppress the cavity periodic fluctuations.*

However, this is not the only conclusion that we could obtain from the spectral analysis. Two more facts that will be fundamental in our future global analysis can be found:

> **Remark 11.** *Cavity periodic fluctuations increase downstream, while, the rod shedding frequency decays downstream.*

A comment should be done about the fact that in the baseline flow the tonal frequency has been found to correspond to the second mode predicted by the Rossiter formula. Sarpotdar et al. (2010) (47) showed a comparison between experimentally observed Strouhal number of the dominant instability associated with cavity tones in their experiments on a cavity with L/D=2 and the prediction of the Rossiter formula. It appears from the comparison (Fig.4 of their paper) that, at high Mach number, their experimental data are in good agreement with the theoretical prediction, showing a tonal frequency corresponding to the first mode predicted by the Rossiter formula, with k=0.75 and γ=0.30. However, at very low Mach numbers, M < 0.3, the experimental cavity tone frequency shifts to a value very close to the one corresponding to the second mode predicted by Rossiter. Similar behaviour was observed by Gharib and Roshko (1987) (48) in their experimental investigation of incompressible flow over an axisymmetric cavity. The authors observed that the cavity oscillates in mode II or mode III, always omitting the first mode. These results appear to be in agreement with the present low Mach number measurements.

Figure 34 shows spectra corresponding to points placed at the level of the rod. On them it is even clearer that the peaks at the vortex shedding frequency decays downstream.

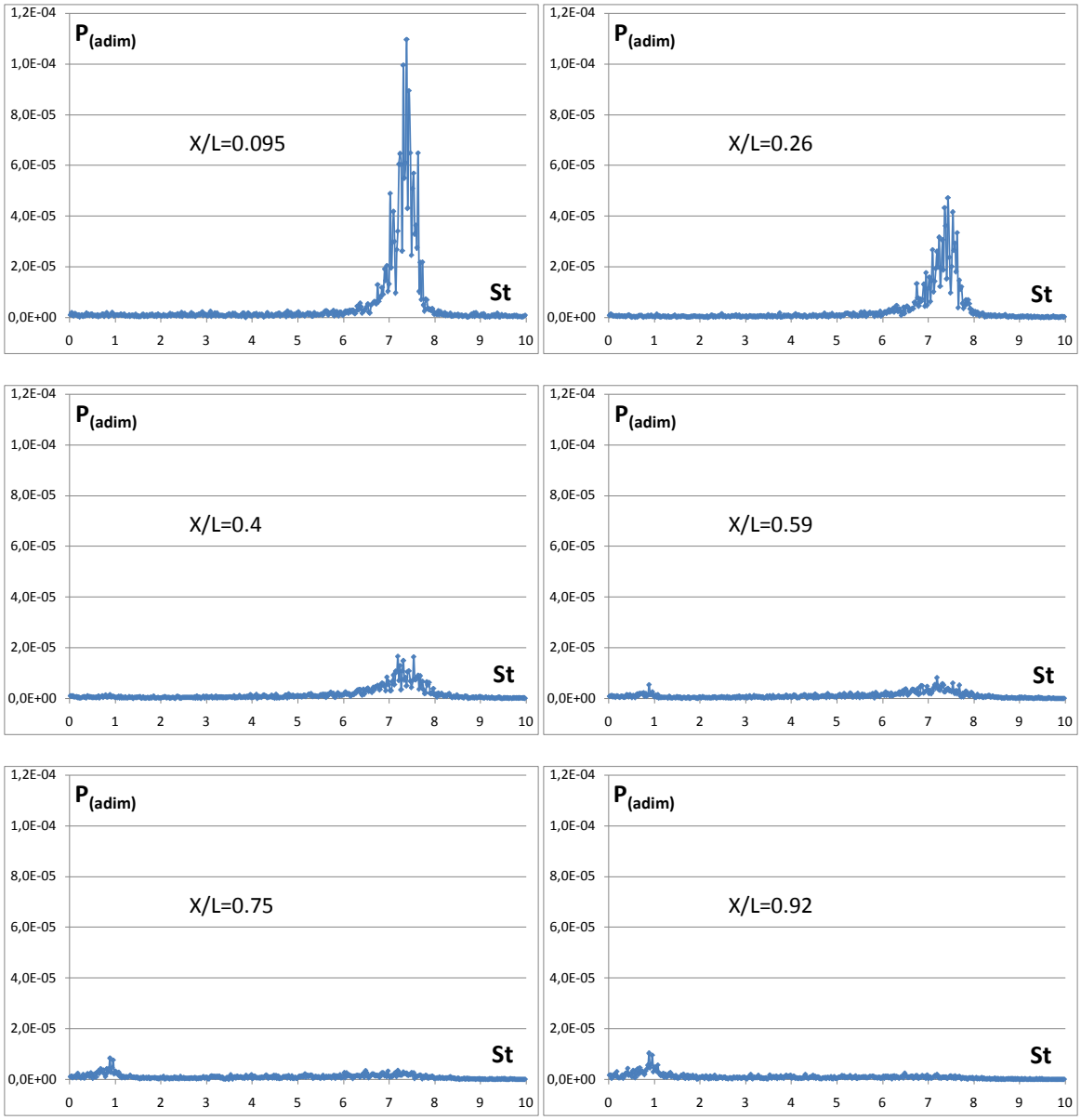

Figure 34. Velocity Frequency Spectra (v-component) at the rod level

Remark 12. *The vortex shedding from the rod decays downstream*

6.1.9 Vortex Detection

The λ_{ci} method was used to detect and follow vortical structures and to know their intensity and swirling direction, this is one of the most powerful and useful methods for vortex visualization.

Samples of snapshots, showing the instantaneous swirling strength and highlighting the spanwise vortices (51) detected in the measurement plane, are shown in Figure 35.

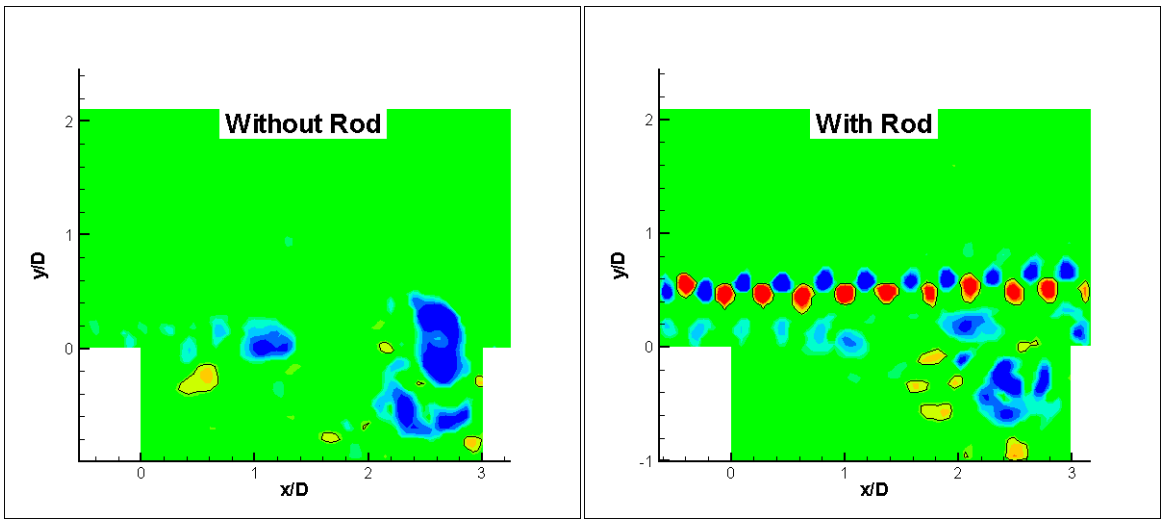

Figure 35. Vortex detected by the λ_{ci} method. Uncontrolled case (left), controlled case (right)

In this figure a high contrast can be observed between the vortical structures present in the uncontrolled cavity (left) and the ones present in the controlled case (right). It is important to remember that those images are snapshots, taken from two sequences of more than three thousand images each.

Periodic vortices are identified in the baseline flow. Watching the sequence of snapshots corresponding to the left image we see that, periodically, vortices appear at x/D=1 and grow up while they are convected downstream until they impinge on the trailing edge of the cavity. In many cases, after the impingement, they split into two smaller vortices; one of them continues traveling downstream while the other half gets immersed in the big recirculation vortex in the downstream half of the cavity (see also Figure 48). It seems that, as described by Rossiter (3), the vortices are formed from the Kelvin-Helmholtz instabilities naturally present in the shear layer at the first third of the cavity length.

Remark 13. *In the non-controlled cavity, vortices generated periodically from Kelvin-Helmholtz instabilities are amplified while they are convected downstream in the shear layer.*

Watching now the image on the right of Figure 35, and the sequence corresponding to it, the first clear difference that we found respect to the previous case is the presence of a vortex line of alternated swirling direction, that form the so called Von Karman vortex shedding from the rod. Regarding this image, two important things must be highlighted: (1) for some reason that will be explained later in this thesis, the intensity of these vortices diminishes downstream, vanishing until they disappear, (2) it is never observed a direct interaction between the vortices from the vortex shedding and the shear layer or the boundary layer.

Remark 14. *The intensity of the vortices shed from the rod diminishes downstream.*

Remark 15. *No direct interaction is seen between the vortex shedding and the shear layer or the boundary layer.*

However, under the Von Karman vortex street a new vortex line appears with the same frequency. It seems that some kind of disturbance produced by the vortex shedding acts on the shear layer instabilities as a "trigger" provoking the train of wake vortices that we referred to in 6.1.5. We will see later that, according to the author's opinion, this mechanism is of paramount importance in the suppression of the Rossiter frequencies; provoking, perhaps, the loss of the necessary regularity of the cycle. The lower vortex street gets weaker downstream disappearing at $x/D \approx 1$ and giving place to bigger vortices with a frequency of the same order of magnitude as the frequency observed in the baseline flow, but without a regular space and time step. **The regularity is lost**.

Remark 16. *The shear layer instabilities can be triggered by disturbances coming from the vortex shedding.*

Remark 17. *As the lower vortex street disappears downstream, bigger and non regular vortices appear in the shear layer.*

Finally, comparing the frequencies and intensities of the vortices detected in Figure 35 with the peaks of the spectra in Figure 29 to Figure 33, a clear relation between them comes out. The peaks in the baseline flow spectra are perfectly compatible with the regular vortices seen in the figures, as their frequency is similar and both increases downstream from 1/4L. The absence of peaks in the controlled flow spectra is compatible with the loss of regularity seen in the vortex detection analysis. Also the high frequency shedding is detected in both places.

6.1.10 Spatial Velocity Correlations

The two-point Spatial Velocity Correlation Coefficient (Correlation between two points of the field at the same time) has been calculated over the entire velocity field, taking reference points over three different streamwise lines. The lower line was at the cavity mouth level (y/D=0), the intermediate line at (y/D=0.2) and the higher line at the rod level (y/D=0.5). The results were presented as a series of snapshots (video) for each level. Since it is naturally impossible to show the whole series in this thesis, only three images for each level will be showed.

a) Component u'u'

The spatial correlation coefficient is defined as follows:

$$\rho_{u'u'} = \frac{\overline{u'_{ref}\, u'_{xy}}}{\sigma_{u'_{ref}}\, \sigma_{u'_{xy}}}$$

Where: $u'_{ref} = (u_{ref} - \overline{u_{ref}})$ is the streamwise velocity fluctuation component at the reference point.

$u'_{xy} = (u_{xy} - \overline{u_{xy}})$ is the streamwise velocity fluctuation component at all the points (x, y) in the field.

$\sigma_{u'_{ref}} = \sqrt{\overline{(u_{ref} - \overline{u_{ref}})^2}}$ is the square root of the variance calculated at the reference point.

$\sigma_{u'_{xy}} = \sqrt{\overline{(u_{xy} - \overline{u_{xy}})^2}}$ is the square root of the variance calculated at all the points (x, y) in the field

Starting by the non-controlled cavity, in Figure 36 we see that, at the cavity mouth level, the correlation is very low. Most of the flow field is green (near zero), while just a few pale blue zones (slightly negative) are visible and just a small elliptical red zone (positive) is present in the surroundings of the reference point.

A similar situation is found in the other levels at the first third of the cavity length. However, things dramatically change from 1/3L on. A sequence of **regularly spaced correlated regions**, alternating between positive and negative values is clearly visible. These vertical elliptical regions become larger as they are placed more downstream.

Remark 18. *A sequence of regularly spaced correlated regions.*

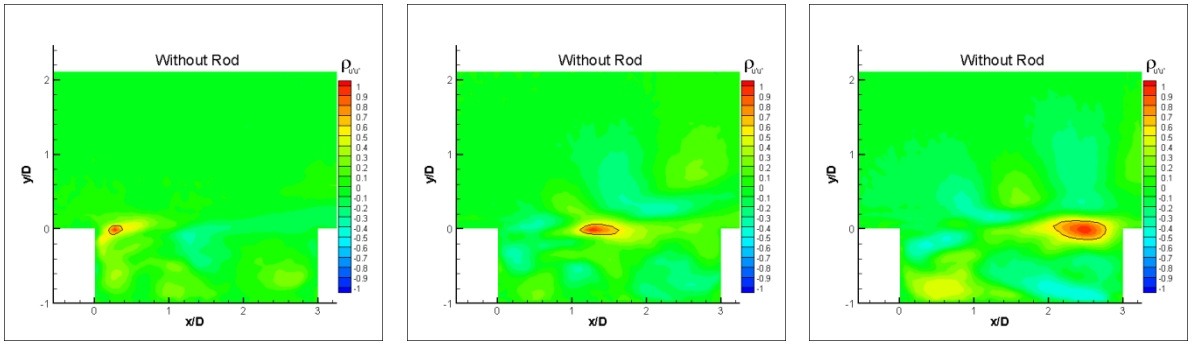

Three points at mouth level (y/D=0)

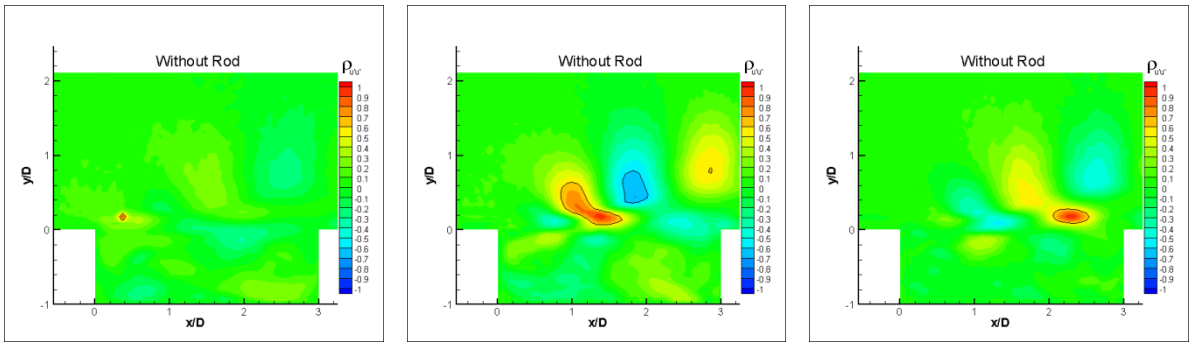

Three points at the intermediate level (y/D=0.2)

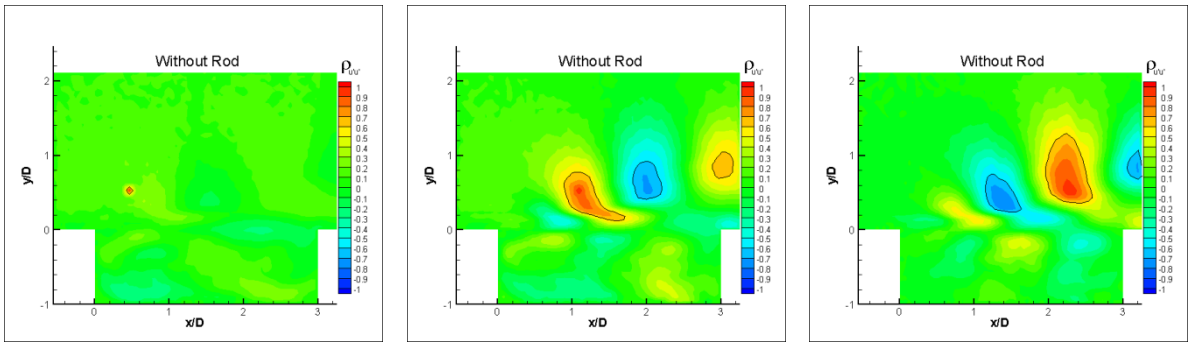

Three points at rod level (y/D=0.5)

Figure 36. Space Correlation Coefficient ρ(u'u') for the uncontrolled cavity for three different reference points at three different levels

Comparing these findings with the λ_{ci} results in the previous section, we find that the distance between two equally correlated areas (about 1/2L) is the same as the distance between two vortices, and they are seen in the same part of the cavity length. Besides, these results are compatible with the second Rossiter mode peaks, seen in the spectra, also in the last two thirds of the cavity length.

Let us now compare with the controlled case. In Figure 37 a long horizontal positive correlation area is found around the reference point, in the shear layer. Besides, there is a negative correlation area above and below it.

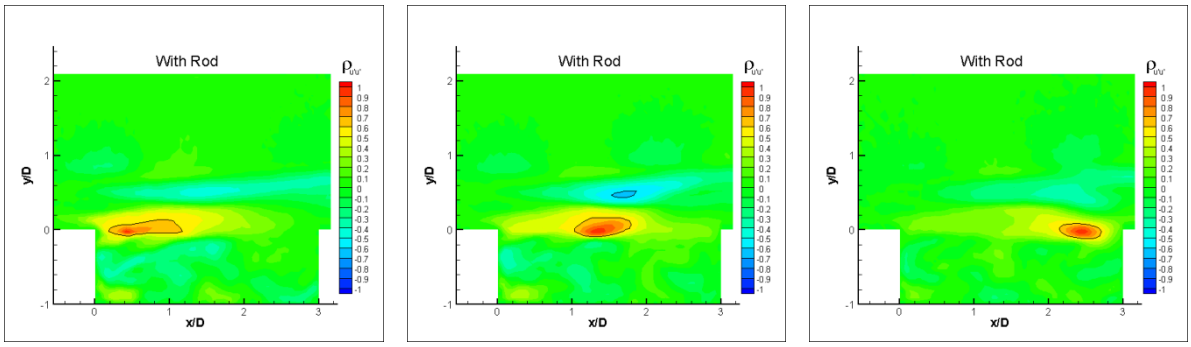

Three points at mouth level (y/D=0)

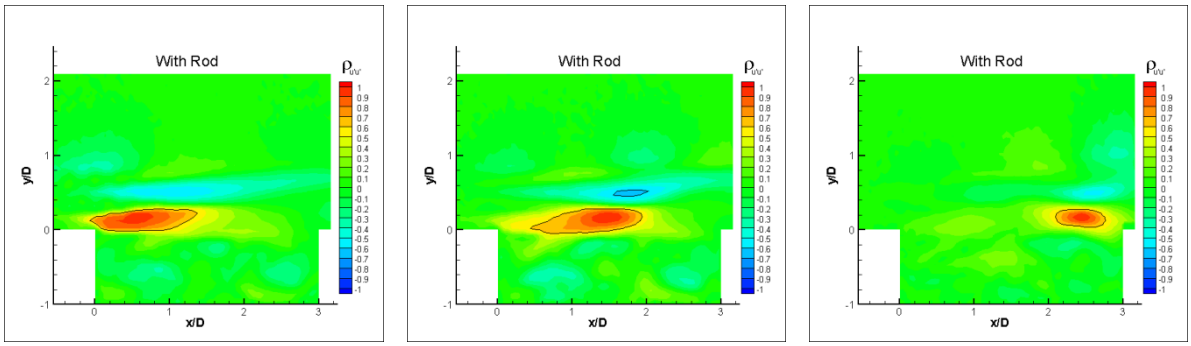

Three points at the intermediate level (y/D=0.2)

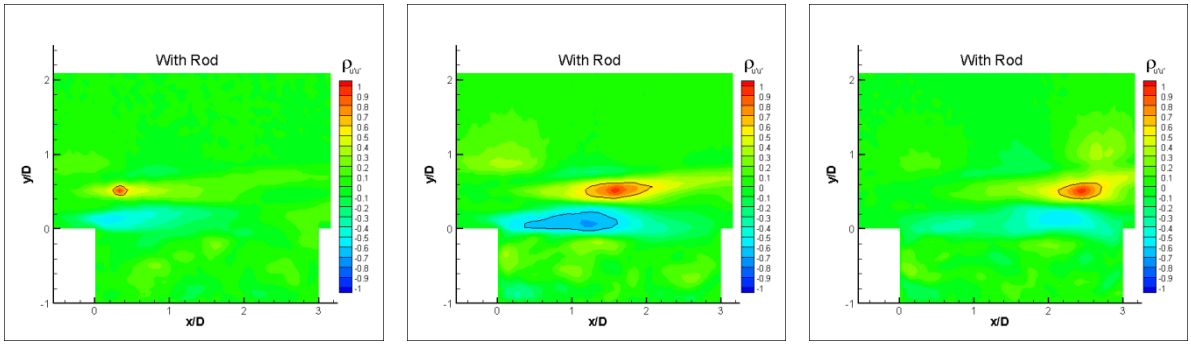

Three points at rod level (y/D=0.5)

Figure 37. Space Correlation Coefficient ρ(u'u') for the controlled cavity for three different reference points at three different levels.

The most important finding on these images is that, unlike in the uncontrolled case, NO REGULARITY IS DETECTED.

b) Component v'v'

The Coefficient is now defined in the following manner:

$$\rho_{v'v'} = \frac{\overline{v'_{ref}\, v'_{xy}}}{\sigma_{v_{ref}}\, \sigma_{v_{xy}}}$$

Let us start again by the non-controlled case. As in previous cases, in the non-controlled cavity we find a sequence of regularly spaced correlated regions alternated between

positive and negative values. In all three levels this effect can be seen from 1/3L of the cavity on, and it seems to be a clear proof of REGULARITY.

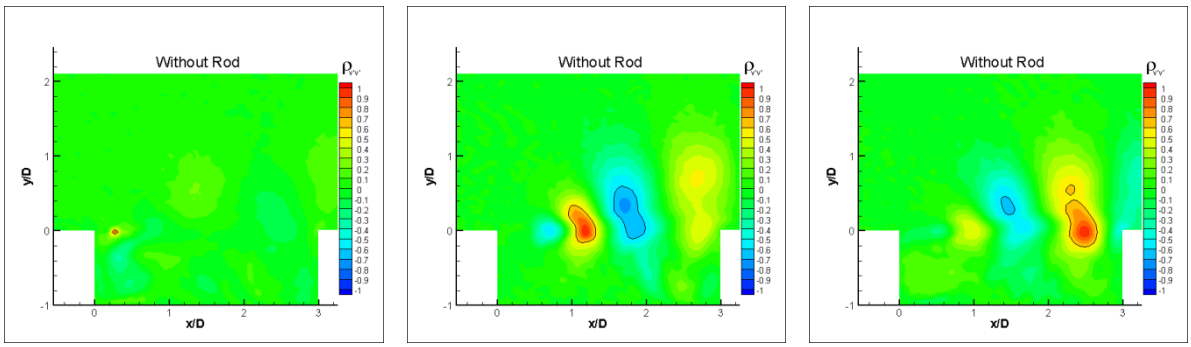

Three points at mouth level (y/D=0)

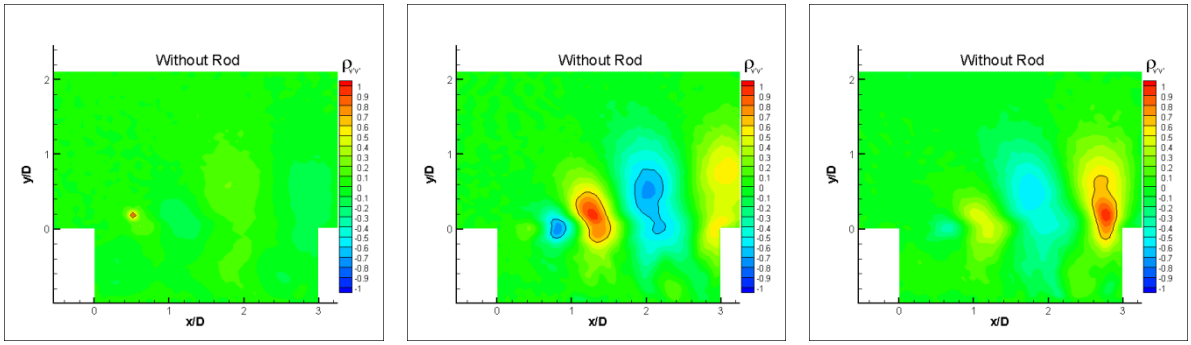

Three points at the intermediate level (y/D=0.2)

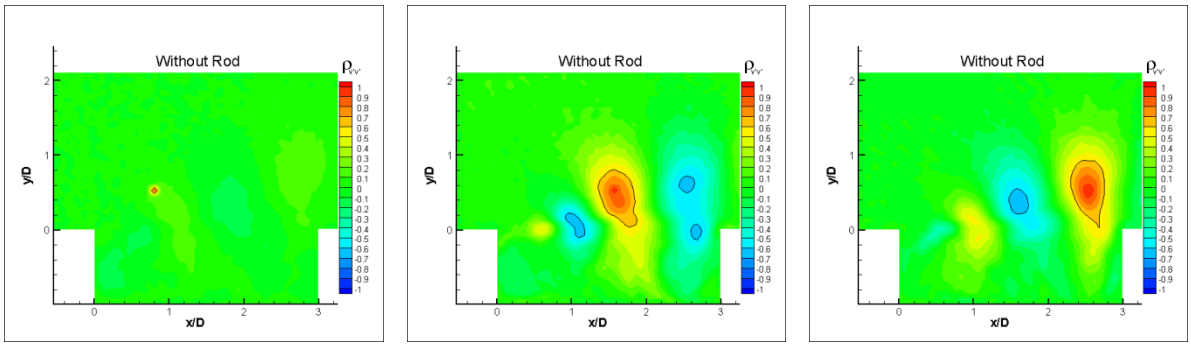

Three points at rod level (y/D=0.5)

Figure 38. Space Correlation Coefficient ρ(v'v') for the uncontrolled cavity for three different reference points at three different levels.

As in the streamwise component case, these results are absolutely coincident with the findings in the λ_{ci} results and in the spectra.

Let us now refer to the controlled cavity. At the mouth level, no sign of regularity is found. Just a small positive correlation area around the reference point is seen. The negative correlation areas in front and behind the reference point are very weak (pale blue) and not equally spaced.

In the intermediate level, we can observe some regularity from the vortex shedding in the first third **getting weaker downstream**. From 1/2L on we can observe alternated positive and negative correlation areas, but **not equally spaced**.

In the upper level the regularity from the vortex shedding is evident, and the vortices **get weaker downstream**. No other sign of regularity is found.

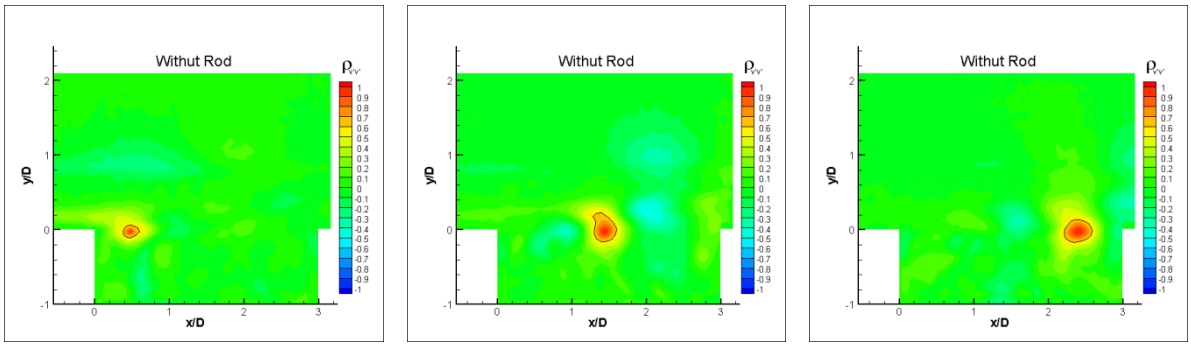

Three points at mouth level (y/D=0)

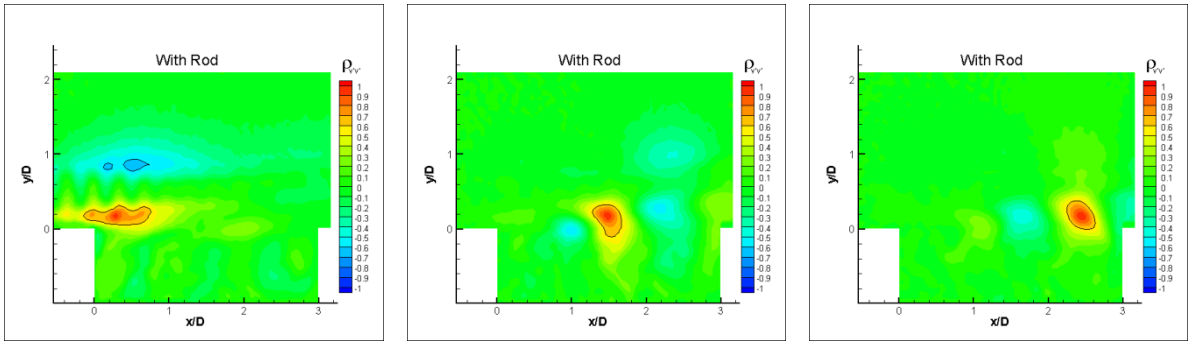

Three points at the intermediate level (y/D=0.2)

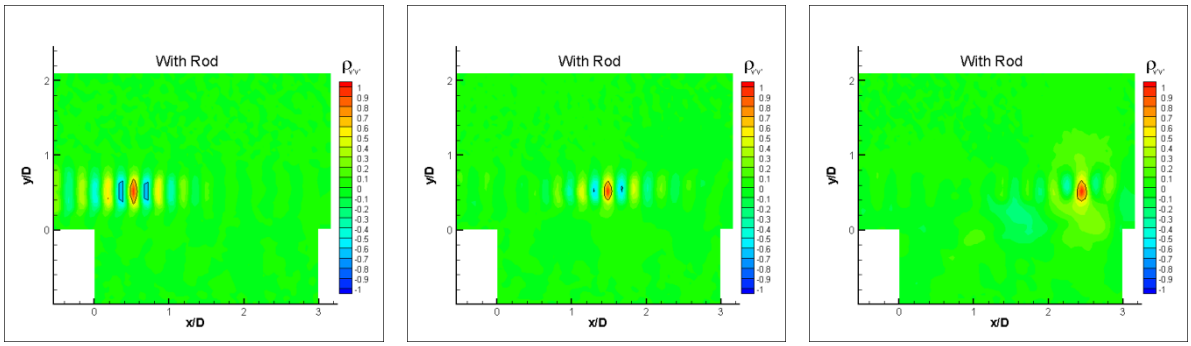

Three points at rod level (y/D=0.5)

Figure 39. Space Correlation Coefficient ρ(v'v') for the controlled cavity for three different reference points at three different levels.

Following, four important remarks are introduced in order to clarify the findings made in this section.

Remark 19. *In the non-controlled cavity, equally spaced large correlated zones, compatible with the low frequency vortex regularity found in previous sections, was found in the downstream two thirds of the cavity length.*

Remark 20. *In the controlled cavity, equally spaced small correlated zones due to the vortex shedding ware found in the first third of the cavity length.*

Remark 21. *In the controlled cavity, non-equally spaced correlated zones were found in the downstream half of the cavity length.*

Remark 22. *In all cases the large correlated zones are amplified as they are placed more downstream; while, the small correlated zones vanishes downstream.*

6.1.11 Momentum Balance and Drag

Taking the fluid inside the cavity as our Control Volume we can apply the momentum balance theorem. This theorem states that the streamwise momentum variation of the fluid inside the cavity equals the streamwise component of the resultant force of all the forces applied on this portion of fluid (R_x).

$$\int_{c.m.} \rho UV dl = R_x$$

In Figure 40 are represented all the forces applied on the control volume, according to it we can express:

$$R_x = P_{\substack{upstream \\ wall}} \cdot D - P_{\substack{downstream \\ wall}} \cdot D + \tau_{floo\,r} \cdot L + \tau_{mout\,h} \cdot L$$

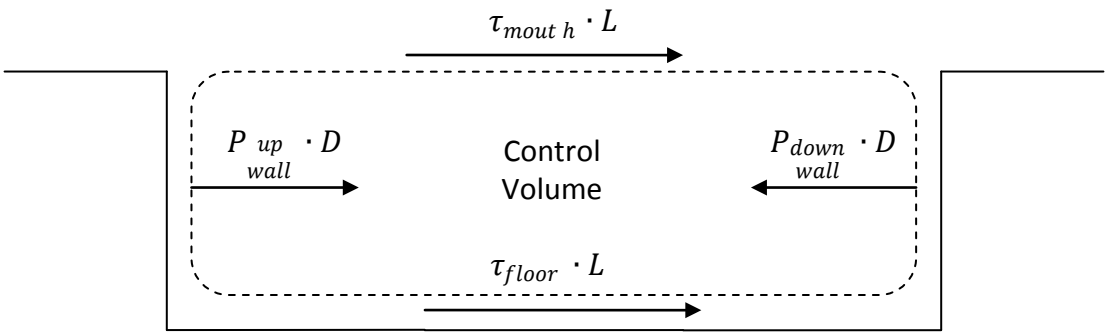

Figure 40. Forces applied on the fluid inside the cavity (Control

Then:

$$\int_{c.m.} \rho UV dl = P_{\substack{upstream \\ wall}} \cdot D - P_{\substack{downstream \\ wall}} \cdot D + \tau_{floor} \cdot L + \tau_{mout\,h} \cdot L$$

The resultant of all the forces that the fluid makes on the cavity is the Drag.

$$D(t) = -P_{\substack{upstream \\ wall}} \cdot D + P_{\substack{downstream \\ wall}} \cdot D - \tau_{floor} \cdot L$$

and

$$\tau_{mout\ h} \cdot L = \int_{c.m.} \mu \frac{\partial u}{\partial y} dl$$

from where:

$$\int_{c.m.} \rho UV dl = -D(t) + \int_{c.m.} \mu \frac{\partial u}{\partial y} dl$$

finally,

$$D(t) = \int_{\substack{cavity \\ mout\ h}} \left(-\rho UV + \mu \frac{\partial U}{\partial y}\right) dl$$

Where, the first term represents the momentum flux (total variation of momentum of the fluid inside the cavity), while the second represents the drag due to the viscous effect (52).

Assuming that the presence of the cavity does not influence the flow upstream and downstream, the momentum balance applied to the flow inside the cavity gives the relation between the drag force on the cavity walls and the momentum flux across the cavity mouth.

In Figure 41 the instantaneous cavity drag coefficient, $CD(t) = \frac{D(t)}{\frac{1}{2}U_\infty^2 D}$ is displayed as a function of time. This time histories show the global unsteady nature of the two flows in the measurement plane. The standard deviations appear to be as high as the mean values for both flows.

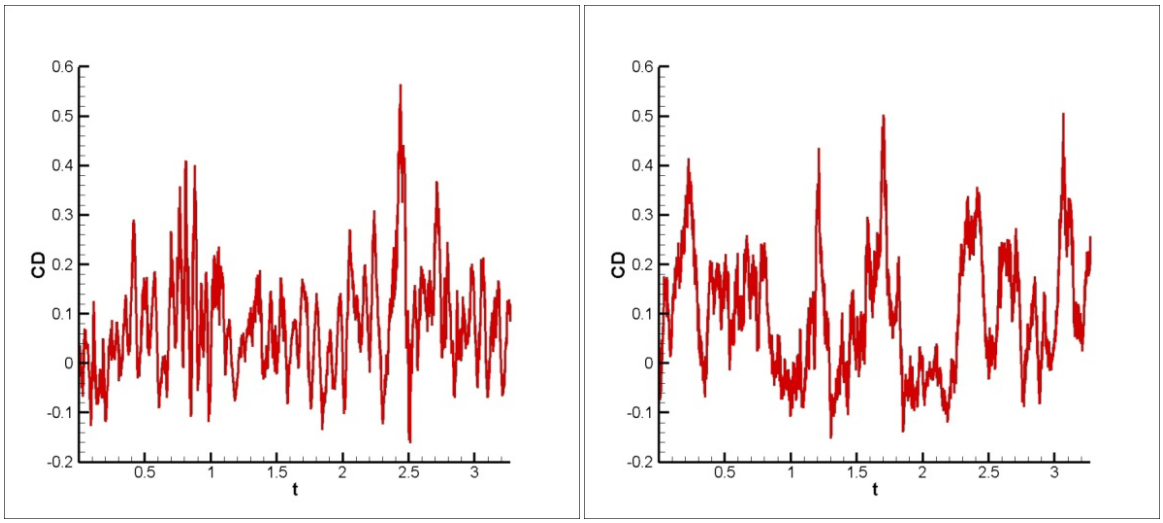

Figure 41. Drag Coefficient Time History, for the uncontrolled cavity (left), and the controlled cavity (right).

In the left image, oscillations of about 10Hz are superimposed to other oscillation of lower frequency and larger amplitude. Even though the time series are too short to be sure (about 3.2 seconds), watching carefully many of them it is possible to detect the presence of oscillations of about 2Hz.

Remark 23. *The low frequency oscillations are detected in the drag spectra.*

In the right image we can see that the 10Hz oscillations have been dramatically attenuated by the presence of the rod, standing out the presence of the low frequency ones which remain.

Until this moment, we have seen in this thesis the presence of frequencies compatible with the Rossiter modes 2^{nd} and 3^{rd} (10Hz and 16.5Hz approximately) and, in the controlled case, a frequency one order of magnitude higher, corresponding to the vortex shedding. The appearance of a new oscillation pushes us to search for new possible mechanisms to explain it. The lower frequency oscillation may be tentatively attributed to a kind of flapping motion involving the whole cavity shear layer.

The mean momentum balance is calculated in a similar way using the following equation. On the right hand side, the first term represents the mean flow, the second term represents the contribution of the fluctuating flow and the third term represents the drag due to viscous effects.

$$\overline{D} = -\int_{\substack{upstream\\wall}} \bar{p} \cdot dl + \int_{\substack{downstream\\wall}} \bar{p} \cdot dl \int_{bottom} \overline{\tau_s} \cdot dl$$

$$= \int_{\substack{cavity\\mout\ h}} \left(-\rho \bar{U}\bar{V} - \rho\overline{u'v'} + \mu \frac{\partial U}{\partial y}\right) dl$$

The contribution of each term of the right hand side equation and the total value are show in Figure 42.

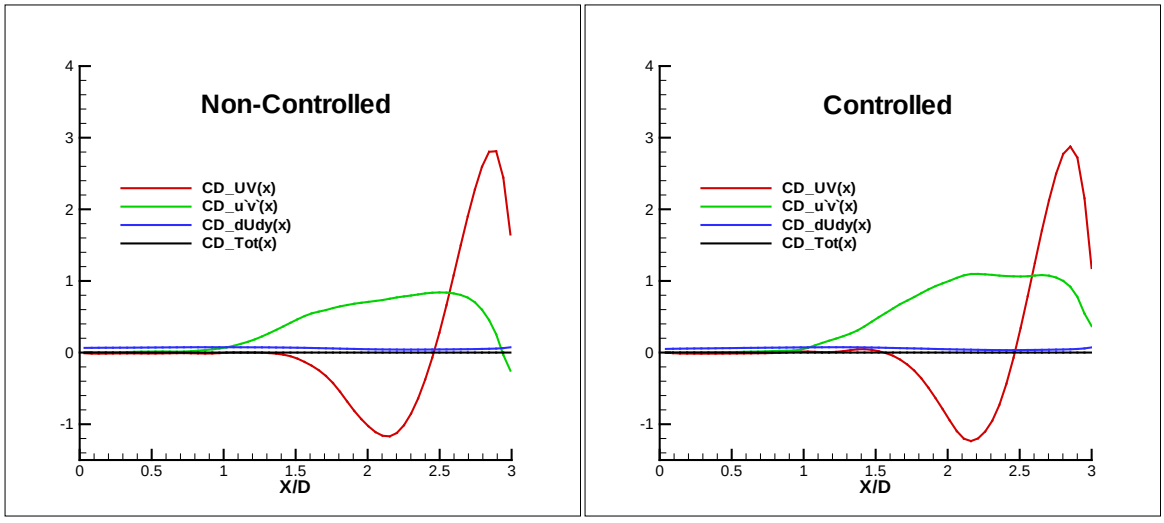

Figure 42. Contribution of each term to the Drag Coefficient

A useful method to evaluate the reasons underlying to the variation of the drag is the computation of a conditioned average. To do this the average is computed considering only the time steps in which the instant value of the drag is higher that (or lower than) a given limit value.

In order to visualize the flow at instants of high and low drag, a conditional average of the flow fields based on:

$$CD_{high} > \overline{CD} + CD_{rms}$$

$$CD_{low} < \overline{CD} - CD_{rms}$$

was performed (Figure 43), leading to the flow configurations in Figure 44 and Figure 46.

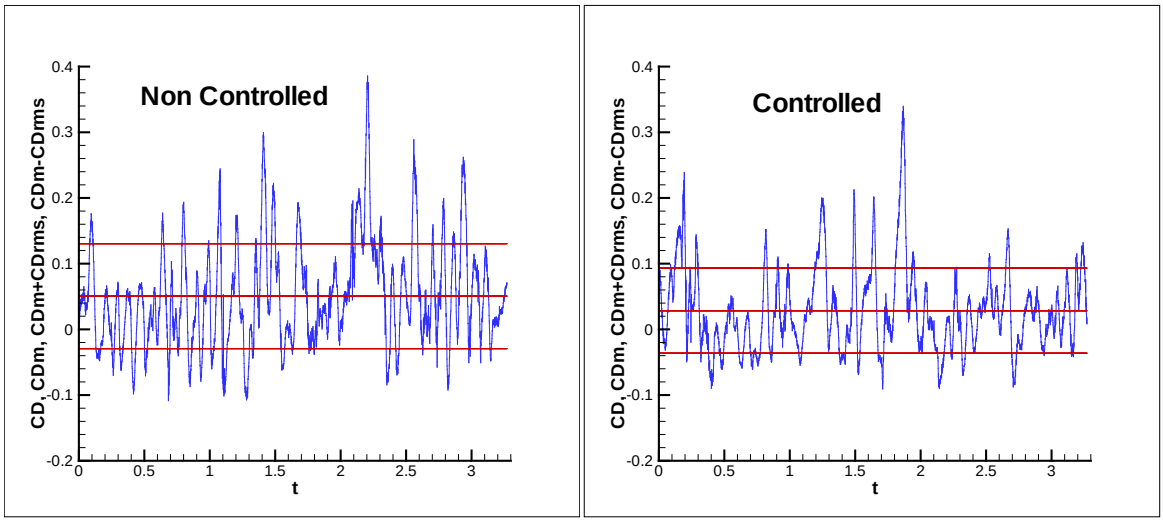

Figure 43. Drag Coefficient time history showing the limits for the Conditional Average.

Where, $\overline{CD}_{non-controlled} = 0.034$

$\overline{CD}_{controlled} = 0.044$

a) Positive Momentum Balance - High Drag Flow Configuration

In the present configuration (Figure 44) we can see that several streamlines starting in the external flow come into the cavity getting immersed into the downstream recirculation zone. This means that the lower part of the fluid, including the incoming boudary layer, is caught inside the cavity. As the fluid comes with a certain velocity (momentum) from the ouside of the cavity and finishes as part of a quasi static vortex, there is a positive transference of momentum to the cavity. Besides, the streamlines after the cavity are more spaced than the ones before it, this means that the flow after the cavity is slower than the flow bebore the cavity, meaning a negative transference of momentum from the fluid.

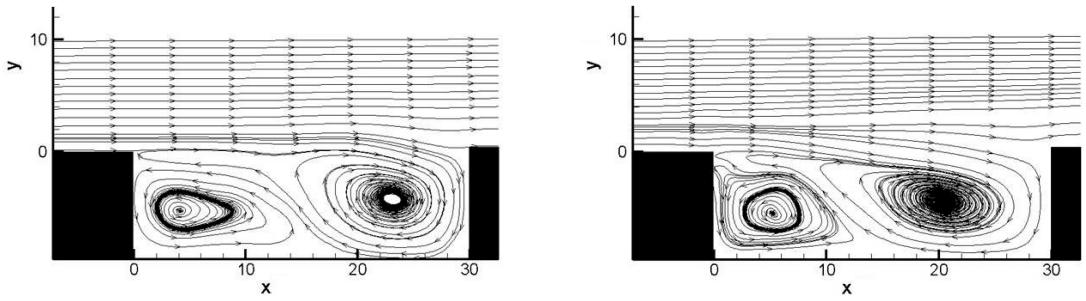

Figure 44. Conditional Averaged Streamlines –HIGH drag flow configuration–. Without control (left) and with control (right).

In Figure 45 the superposition of the velocity field and the Lambda-Ci field show more clearly the relation between the incoming flow and the vortices.

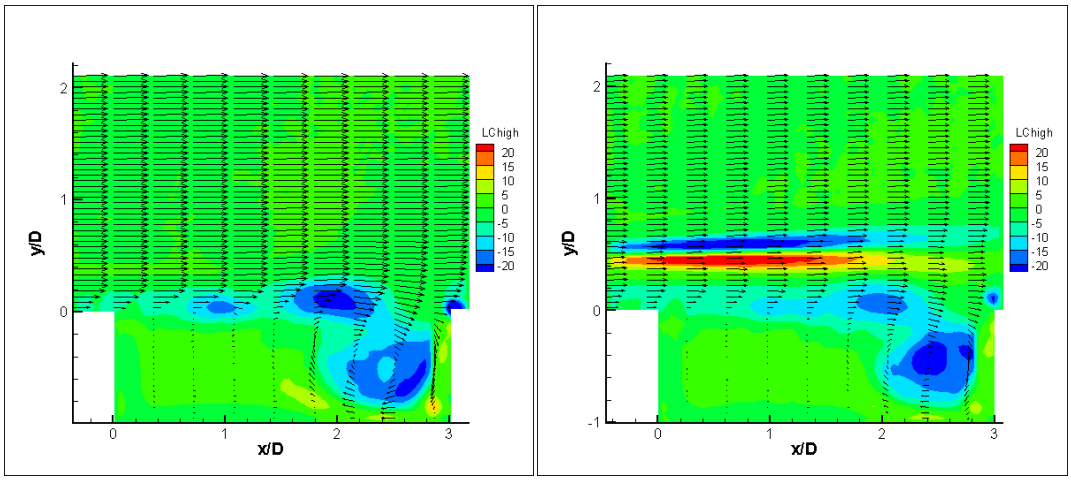

Figure 45. Conditional Averaged mean velocity field (vectors) superimposed to Lambda-Ci field – HIGH drag flow configuration. Without control (left) and with control (right).

Another possible approach is to consider that a stagnation point is placed on the downstream wall, producing a high pressure area on it.

b) Negative Momentum Balance - Low Drag Flow Configuration

The inverse situation can be seen in this configuration. A net flux of mass leaves the cavity, meaning a net transference of momentum from the cavity to the external fluid. It is, also, very easy to see that the flow is accelerated downstream of the cavity, since the streamlines are much closer.

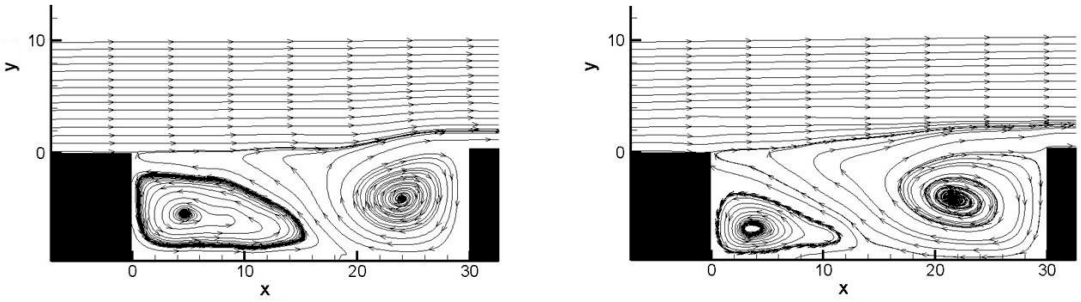

Figure 46. Conditional Averaged Streamlines –LOW drag flow configuration–. Without control (left) and with control (right).

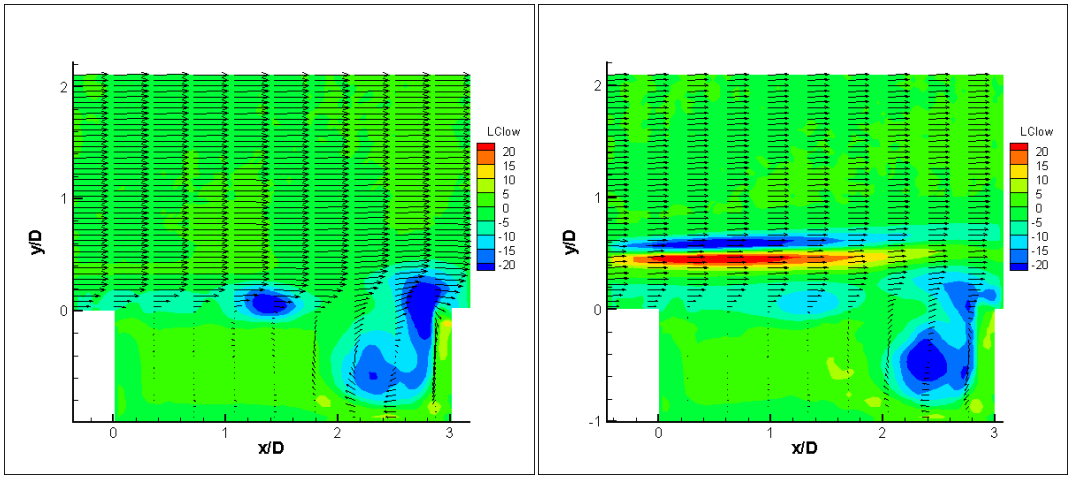

Figure 47. Conditional Averaged mean velocity field (vectors) superimposed to Lambda-Ci field – LOW drag flow configuration. Without control (left) and with control (right).

Comparing the two images in Figure 44 and in Figure 46 no significant modification seems to be produced by the rod. This means that the High Drag Configuration and the Low Drag Configuration have no relationship with the Rossiter frequencies or with the shedding frequency.

Watching the time series as a video it is possible to obtain some interesting information. During the 3.3 seconds about 34 switches between both configuration take place, this is coincident with the frequency of the 2nd Rossiter mode. However, the most important thing is that, while in the non-controlled case those configurations switches seems to be equaly spaced in time, in the controlled cavity they are not.

Remark 24. *The High Drag Configuration and the Low Drag Configuration are not modified by the presence of the rod, themselves. However, the presence of the rod affects the regularity of the change between them.*

It is important to highlight the 'spiral' pattern of the streamlines in the downstream vortices. According the the Mass Conservation Principle, a flow normal to the evaluated plane (z-direction) must be present in the center of those vortices. In the case of Figure 44 we see that the spiral is cetripetal, therefore, its center must behave as a source. In Figure 46 the spiral is centrifugal, so its center must behave as a sink. In onther words, being water an uncompressible fluid, at a given plane, any income must be acompanied by and outcome.

In Figure 48 instantaneous detected vortices are shown superimposed to the velocity field, for the baseline flow. The plotting (a) refers to an instant of high drag, while the vortex is still far from the trailing edge ($x/D \approx 3$) producing and inflow clearly shown by the vectors. The (b) plotting is an intermediate instant when the vortex is closer to the trailing edge and the vectors show an equilibrated flow. The last plotting (c) shows the vortex impinging the trailing edge and splitting into two smaller vortices, the vectors show a clear outflow.

In other words, it is clearly seen that an outflow takes place when the vortex jumps over the trailing edge (or impinges it); conversely inflow takes places when the vortex is approaching the trailing edge. Similar oscillating behavior is observed in the case of the controlled flow but without regurarity.

Shear layer oscillating behavior is also described by Ukeiley and Murray (2005) (53). They demonstrated the pumping action occurring in an open cavity (with L/D=5.16 and subsonic flow of Mach=0.2), showing cycles of inhalation phase followed by exhalation phase. They observed that the pumping cycles are driven by a build up of fluid beneath the shear layer.

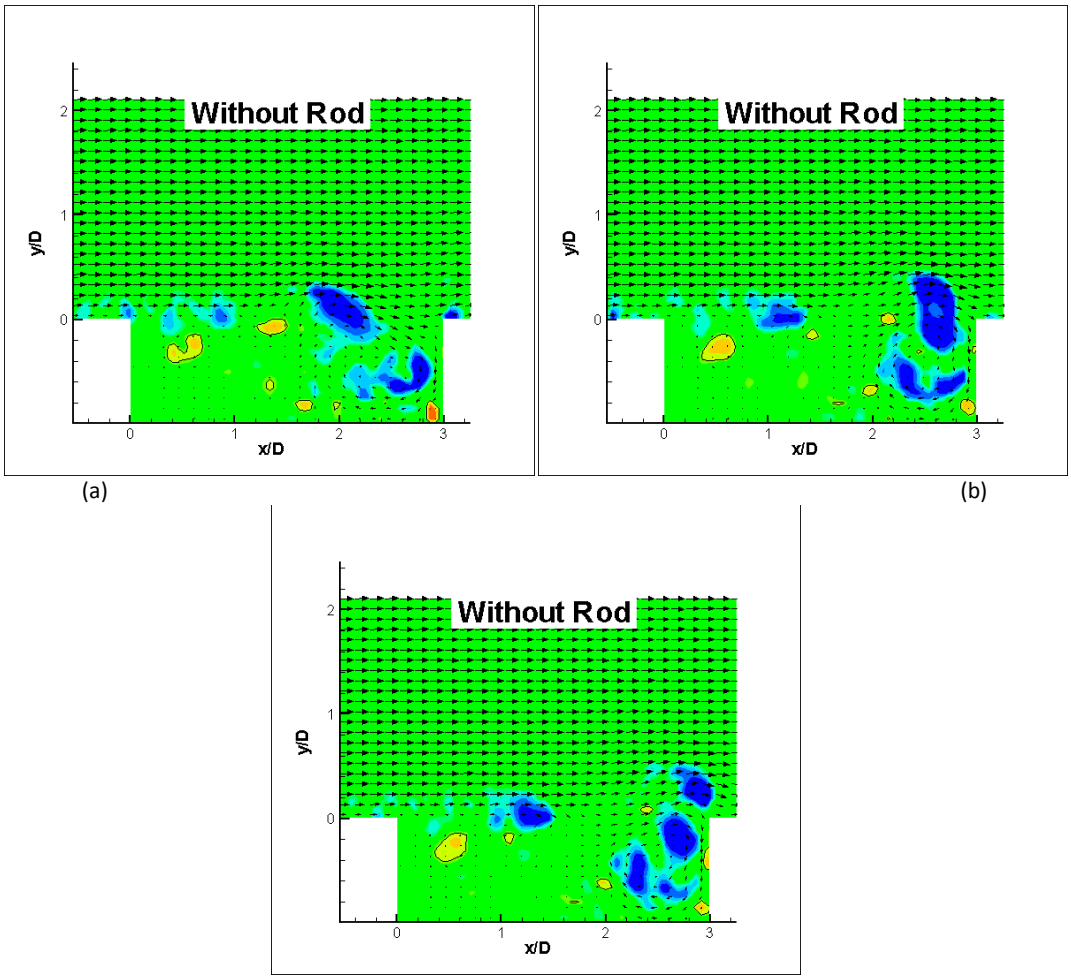

Figure 48. Instantaneously detected vortices superimposed to the velocity field for the baseline flow. (a) A vortex at x/D=3 produces an inflow. (b) The vortex is approaching the trailing edge. (c) The vortex impinges the trailing edge splitting into two smaller vortices and producing an outflow.

Finally, the observed inflow and outflow oscillations and flow continuity suggest, for the baseline and the controlled, the existence of a transversal periodic motion. This is highlighted also by the spiral nature of the primary recirculating bubbles described before.

Considering that there is enough evidence that 3D phenomena plays an important role in the flow under study, we decided to clarify this situation by leading further experiments in order to evaluate the 3D characteristics of the flow.

c) Drag Introduced by the Rod

In the previous analysis of the drag the direct contribution of the rod, which is certainly important, was ignored. The reason is that we intend to focus our work in the analysis of the cavity flow and the phenomena introduced in it by the high frequency forcing.

For a Reynolds number $Re_{\Phi} = 248$ the drag coefficient of a cylinder normalized with ϕ is $CD_{\Phi} = 1.5$. The corresponding value normalized with the cavity depth, as in the previous cases is about $CD_D = 0.12$.

6.2 Parallel Planes Data Analysis

Considering (a) the fact that the re-organization of the spanwise vorticity in the shear layer due to the high frequency vortex shedding from the cylinder may play an important role in the suppression of the cavity tone (Stanek et al., 2007), (b) the finding of low frequency oscillations in the drag spectra, which could not be explained for the Rossiter mechanism, and (c) the observation of streamlines coming in and out of the cavity periodically we assumed that the three dimensional effects would not be unimportant. For that reason new Time Resolved PIV measurements were made in five planes (see Table 4) parallel to the cavity surface (*xz*-planes in our coordinate system) to find a proper explanation to those effects and to evaluate a possible connection with the high pressure peaks and with the suppression mechanism under study. The most remarkable findings were made at the internal levels of the cavity (Levels 1 and 2). For that reason we will refer mainly to them in our analysis.

6.2.1 Instant Velocity Field

Figure 49 to Figure 52 show snapshots of the vector fields corresponding to the Instant Velocity Fields at Levels 1 and 2, for the controlled and for the uncontrolled cavity. The superimposed shadowed areas show limited regions where the direction of the flow is transitorily reverted. Inside those regions the streamwise component of the flow has a direction opposite to the free stream. At both levels it is possible to observe strong jets directed against the upstream wall of the cavity, those jets periodically appear at different

points along the cavity span. Those real cellular fluid-dynamic structures impinge over the cavity wall splitting into two spanwise jets, or giving birth to vortical structures.

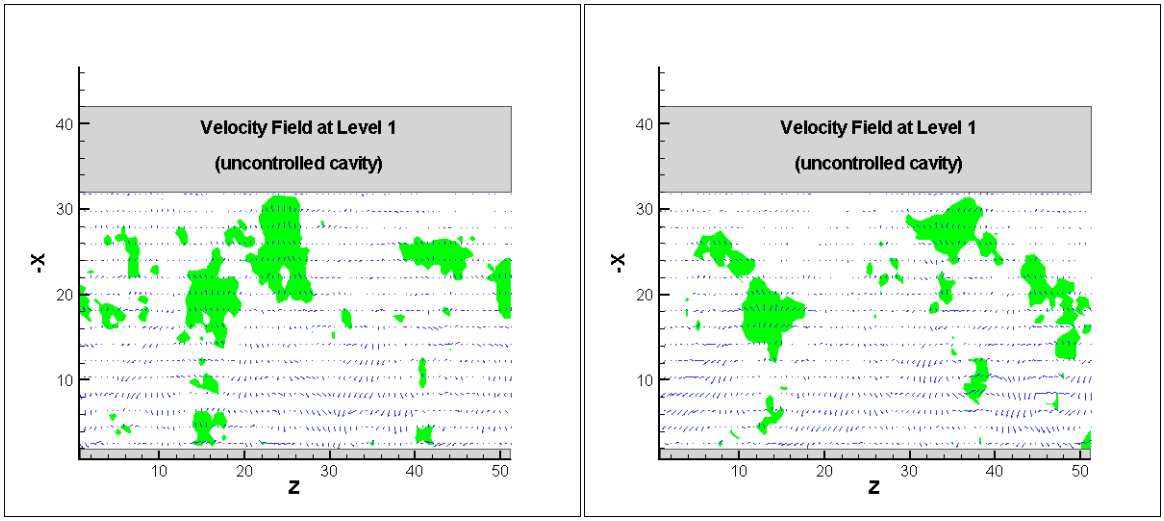

Figure 49. Two snapshots of the Instant Velocity Field in the Uncontrolled Cavity at Level 1. The superimposed colorized areas show reversed flow.

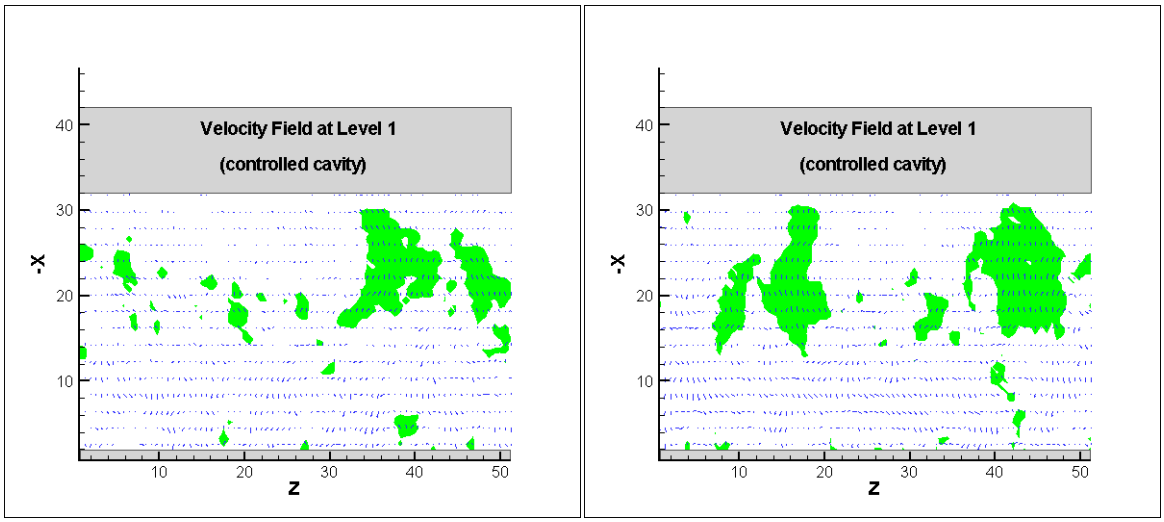

Figure 50. Two snapshots of the Instant Velocity Field in the Controlled Cavity at Level 1. The superimposed colorized areas show reversed flow.

As shown in Figure 49 and Figure 50 the jets seem to be more intense and organized in the deeper plane. Watching the videos from which the snapshots were taken, there seems to be some temporal regularity between the appearances of the cellular structures.

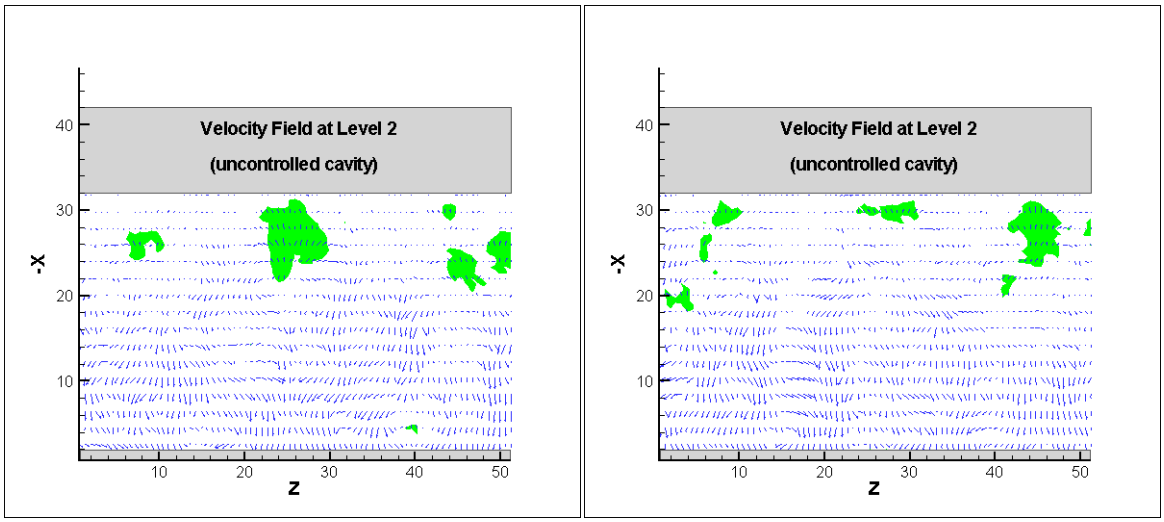

Figure 51. Two snapshots of the Instant Velocity Field in the Uncontrolled Cavity at Level 2. The superimposed colorized areas show reversed flow.

Possibly, those jets impinging periodically over the cavity upstream wall are related to the fluctuations of the drag.

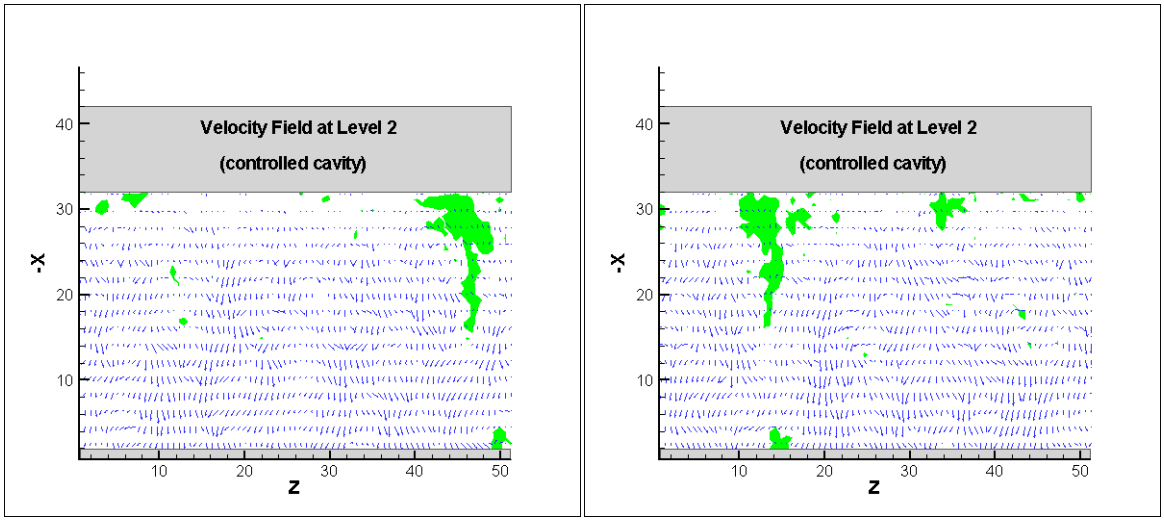

Figure 52. Two snapshots of the Instant Velocity Field in the Controlled Cavity at Level 2. The superimposed colorized areas show reversed flow.

6.2.2 Mean Velocity Field

The Mean Velocity fields do not provide new information; however, their analysis is important to test the congruence between the measurements made on the *xz*-panes and those made on the *xy*-planes. Besides, in is useful to confirm the exactly position of their Levels respect to the fluid-dynamic structures present in the cavity.

Starting with Level 2 (1mm under the cavity mouth level), we observe that the velocity absolute value gets larger as it is measured more downstream (Figure 53). Its value is null in the vicinity of the leading edge and its value overpasses the 50% of the free stream velocity in the downstream third of the cavity, diminishing near the trailing edge. The presence of the control device does not seem to produce any important effect in this case. The only visible difference is a faster increase of the velocity in the zone close to the leading edge.

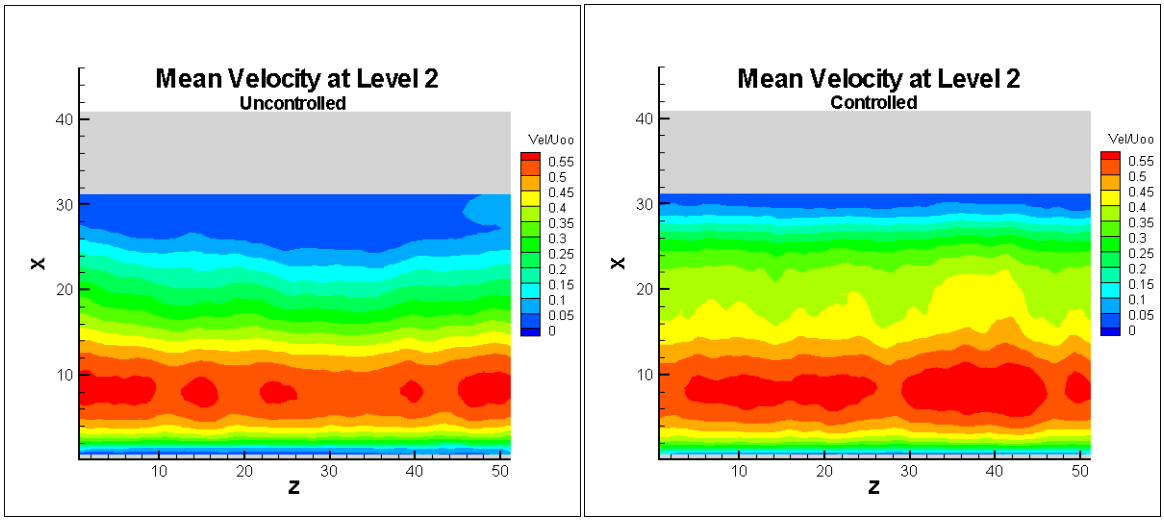

Figure 53. Mean Velocity Field at Level 2, for the uncontrolled cavity (left) and for the controlled cavity (right)

In Figure 54 we see the value of the streamwise component of the velocity. Through this variable it is possible to know the direction of the flow. In this level, close to the cavity mouth, the mean average motion is always in the direction of the free stream.

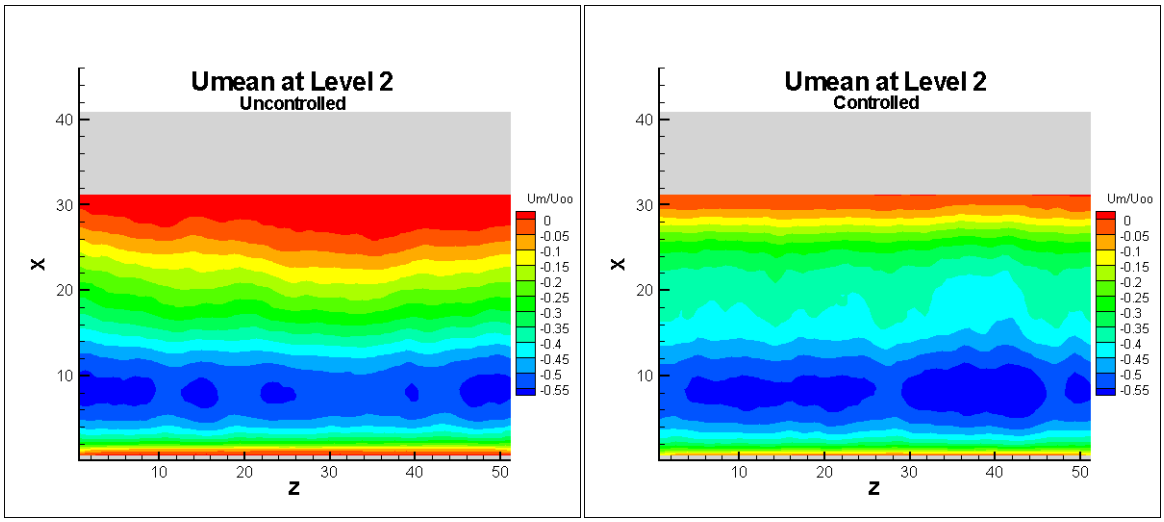

Figure 54. Mean Streamwise Velocity component (U) at Level 2, for the uncontrolled Cavity (left) and for the controlled Cavity (right).

At Level 2 (4mm under the cavity mouth) a clear increase of the velocity is seen from the leading edge. Its maximum value is found near L/3, where it reaches 15% U_∞ (Figure 55), beyond that point it descends again to become null again near L/2. In the second half of the cavity the velocity grows up again reaching a maximum of 18% U_∞ at 3/4L.

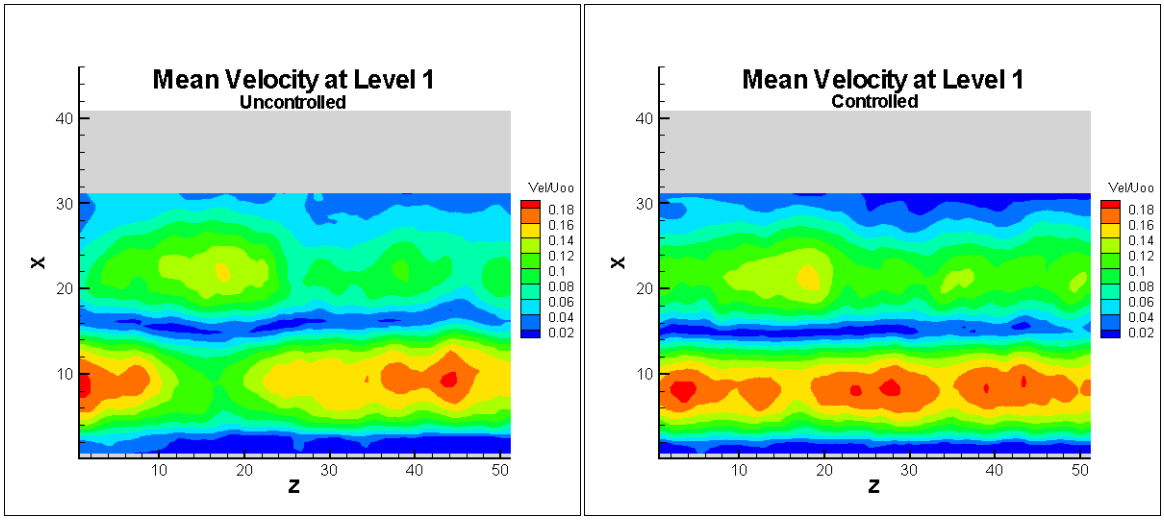

Figure 55. Mean Velocity Field at Level 1 (-4mm) for the uncontrolled Cavity (left) and for the controlled Cavity (right).

In this case, the study of the behavior of the streamwise velocity component (Figure 56) clarifies the described situation. The first maximum corresponds to a velocity with a direction opposite to the free stream; while, the second one corresponds to a velocity with downstream direction. Analyzing Figure 15 we can see that the *xz*-plane at Level 1 is placed immediately over the center of the clockwise vortex, present in the second half of the cavity, and over the center of the counterclockwise vortex, present in the first half of it. In this way the measurements in both, the normal and the parallel planes, are absolutely congruent.

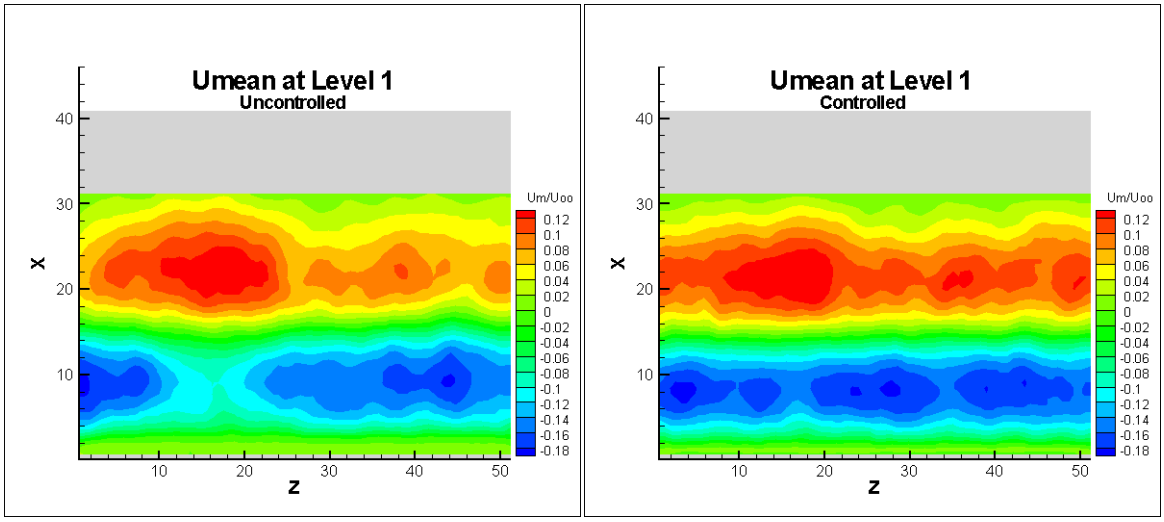

Figure 56. Mean Streamwise Velocity component (U) at Level 1 for the uncontrolled Cavity (left) and for the controlled Cavity (right).

6.2.3 Velocity Frequency Spectra

The analysis of the *xz*-planes permit us to compute the frequency spectra for the spanwise fluctuating component of the velocity. In Figure 57 we can see the spectra corresponding to Level 2. As in the normal plane, we can see peaks in the uncontrolled flow. Those peaks are coincident with the 2nd and the 3rd Rossiter frequencies, and they grow up downstream. On the other hand, we see that in the controlled flow the frequency peaks are clearly attenuated.

Remark 25. *The Rossiter frequencies are clearly seen and the peaks are also suppressed by the presence of the rod.*

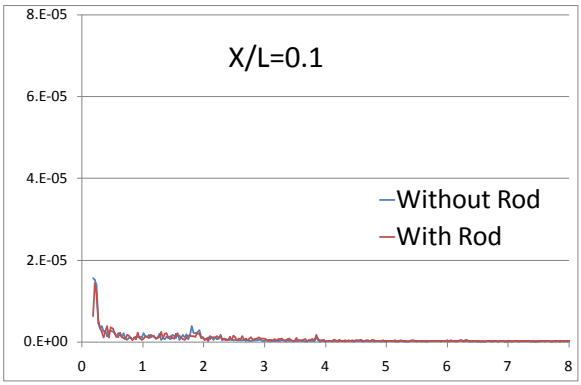

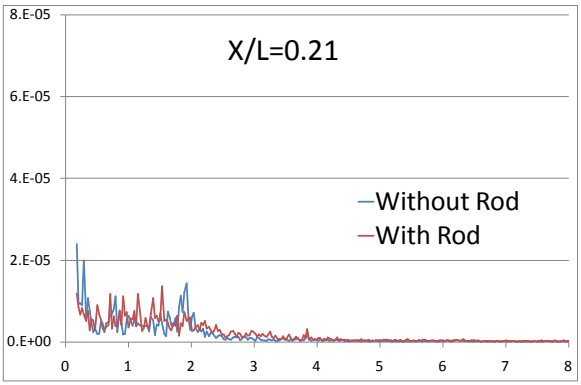

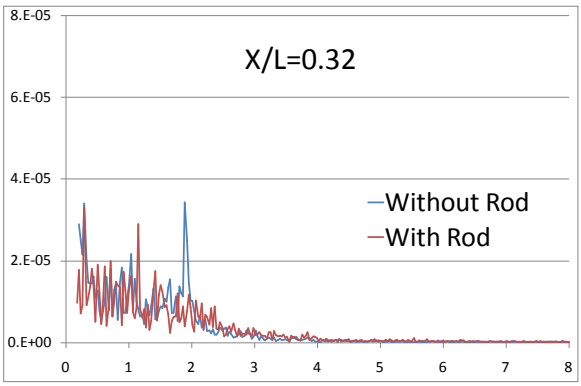

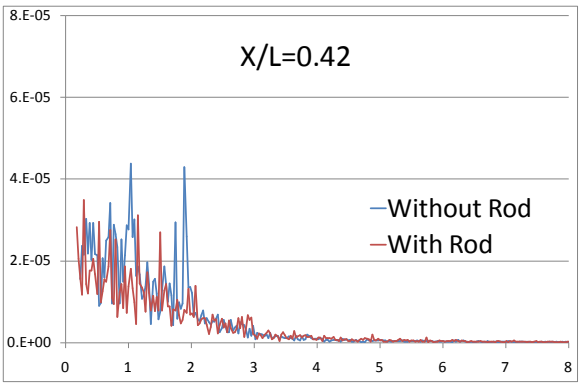

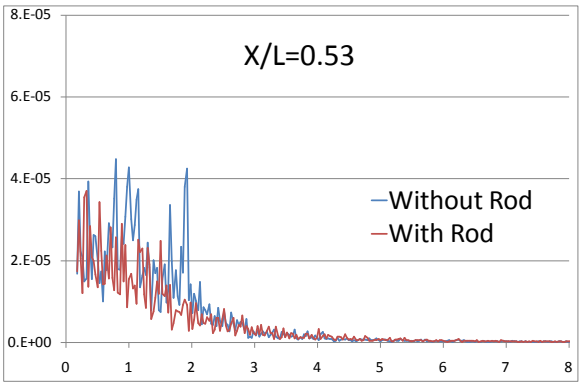

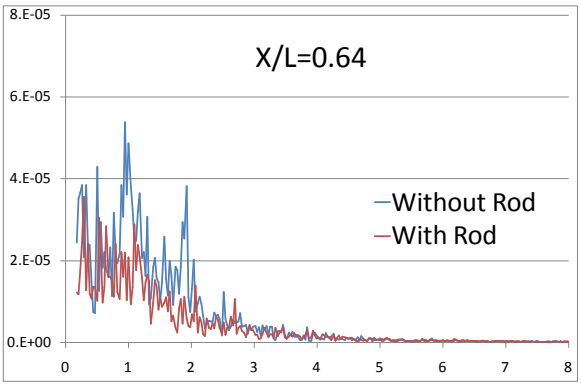

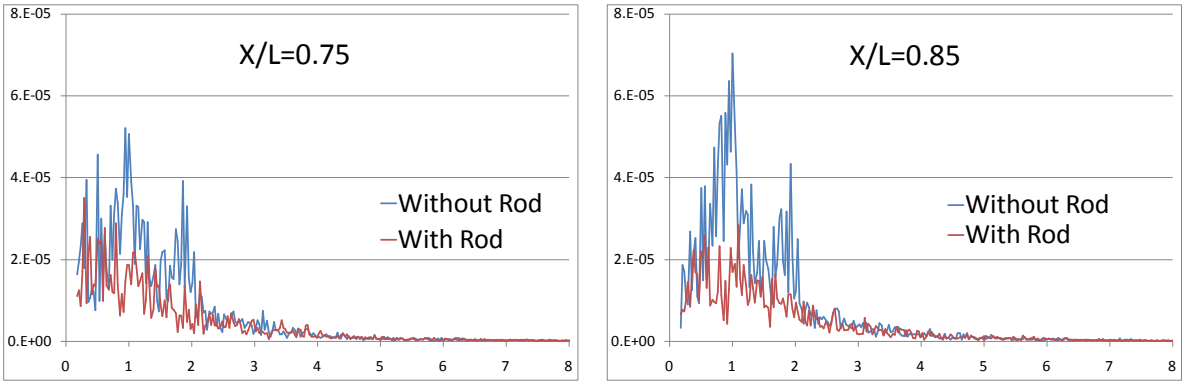

Figure 57. Normalized Power Spectra ($\boldsymbol{P_{adim}}$) of the spanwise velocity component at different x/L and at the cavity mid span at Level 2.

At Level 1 (4mm under the cavity mouth) the Rossiter frequencies are not so clearly visible. At the points placed in the downstream half of the cavity those peaks seem to mix up with other badly defined frequencies close to St=0.5. This seems to be a sign of the presence of spanwise oscillations with a frequency lower that the Rossiter modes. However, due to the fact that the acquisition time of our experiments was too short for those frequencies, we cannot assure their existence from the spectra.

Remark 26. *Oscillations at frequencies lower tan the Rossiter modes seem to be present, but this cannot be assured due to the short acquisition time.*

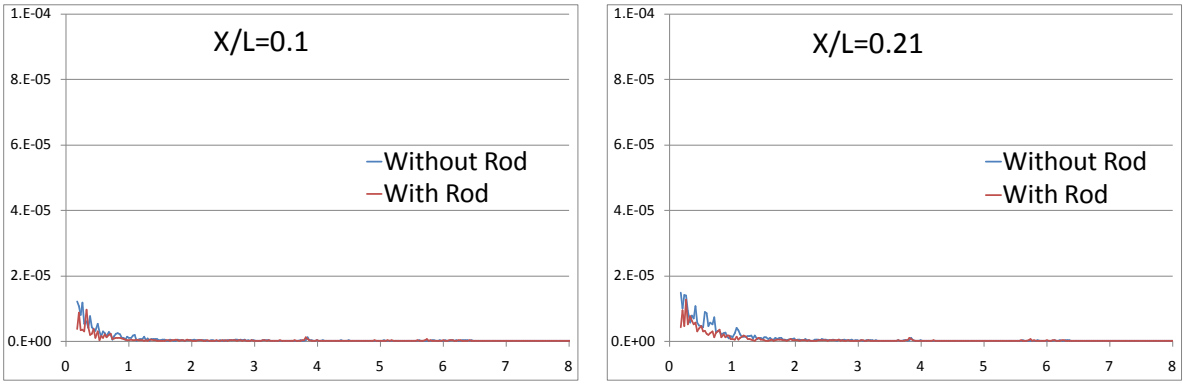

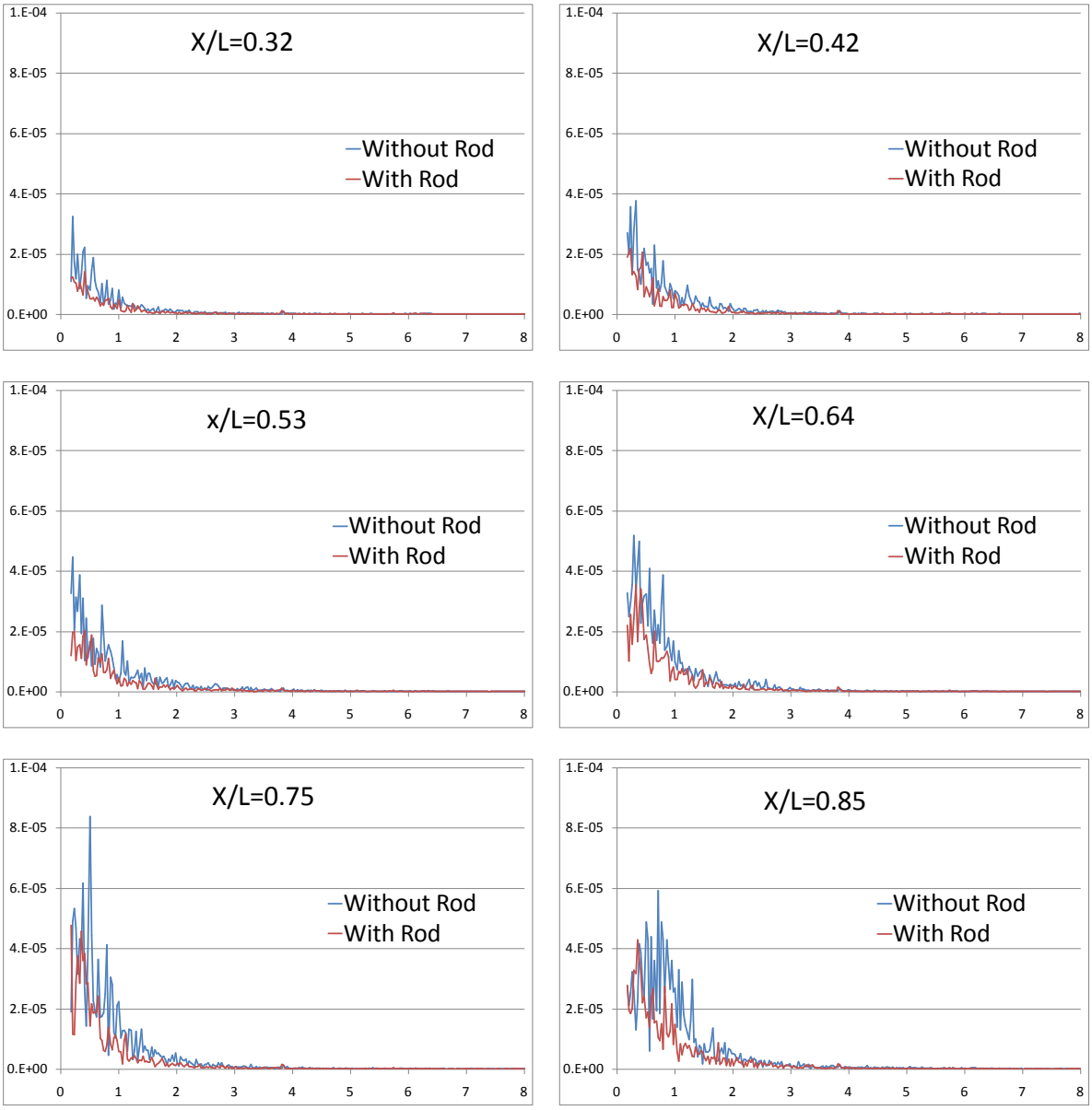

Figure 58. Normalized Power Spectra ($\boldsymbol{P_{adim}}$) of the spanwise velocity component at different x/L and at the cavity mid span at Level 1.

The low frequency peaks seem to grow up as we get closer to the center of the recirculation vortex. The presence of the rod seems to produce just a moderate attenuation of the low frequency peaks.

Remark 27. *The presence of the rod does not seem to be so efficient in the suppression of the low frequency peaks.*

6.2.4 1D Spatial Velocity Correlations – Spanwise Component

Continuing with the study of the spanwise flows present inside the cavity, we will analyze the spatial velocity correlation of the fluctuating w'-component ($\rho_{w'w'}$). We will compute these correlations in the spanwise direction, first. This means, we will compute the correlation between one reference point $P(X_{ref}, Z_{ref})$ and all the rest of the points along the same *x*-coordinate, $P(X_{ref}, Z)$. Putting together all the graphics corresponding to the different *x*-coordinates an *xz*-plane is generated, where the function $\rho_{w'w'}(x, z)$ indicates the correlation referred to the mid-*z* point.

Four plots of this kind are shown in Figure 59 as a 3-dimensional overview of the $\rho_{w'w'}$. In all the cases a central crest, corresponding to the reference points, is clearly seen where $(\rho_{w'w'} = 1)$. This value decays rapidly to both sides.

The correlation function has a particular behavior in the vicinity of the leading edge. In that zone its value decays more slowly than in the rest of the cavity, and negative peaks followed by positive peaks are located at both sides. In other words, each reference point is surrounded by two negative side peaks and two positive side peaks.

As the correlation is computed farther from the leading edge the side slope is steeper and the rest of the field is flat, showing values close to zero.

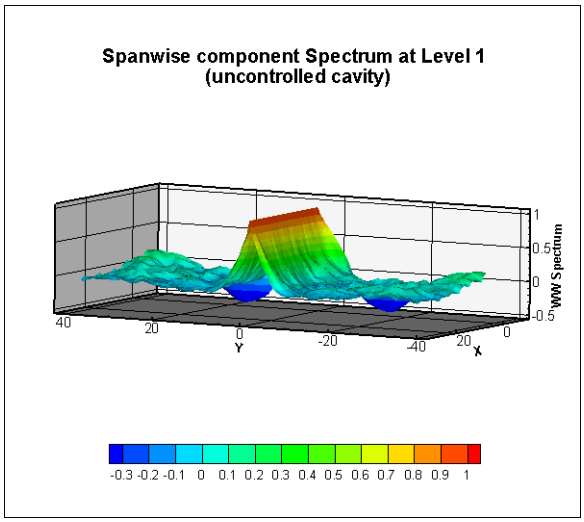

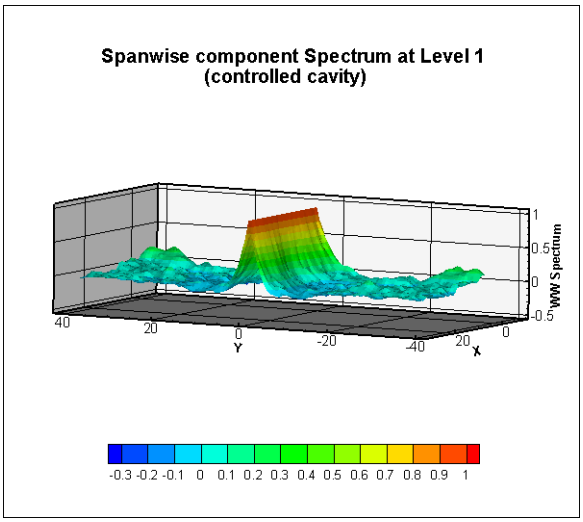

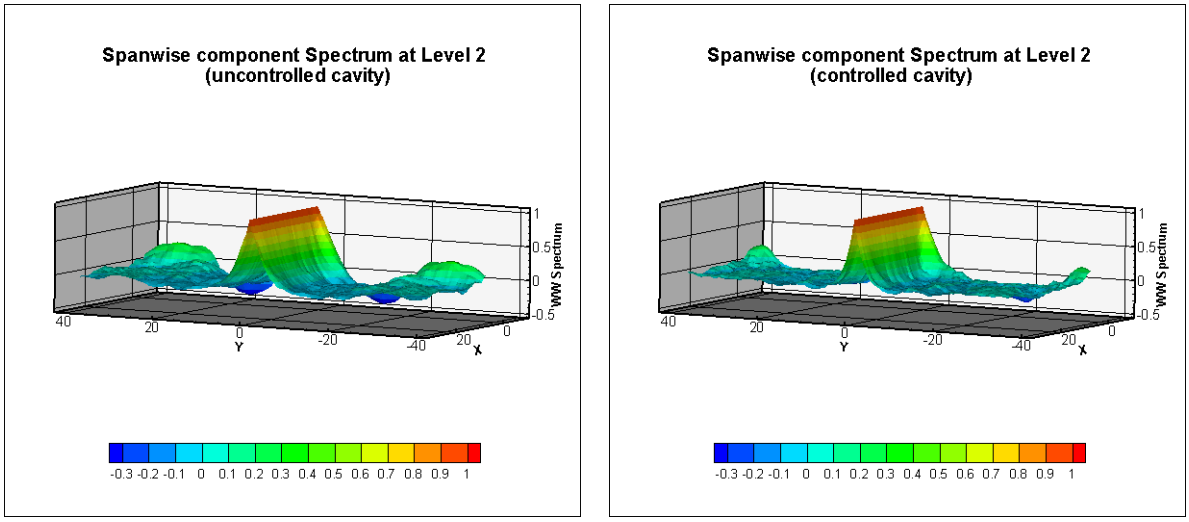

Figure 59. 3D overview of the Correlation $\rho_{u'u'}$ along the z-dimension for all x-positions

Figure 60 shows a more classic plotting of the same field. Besides supporting the previous observations we can find out from it that the presence of the rod increases the distances of the negative and positive side peaks from the center.

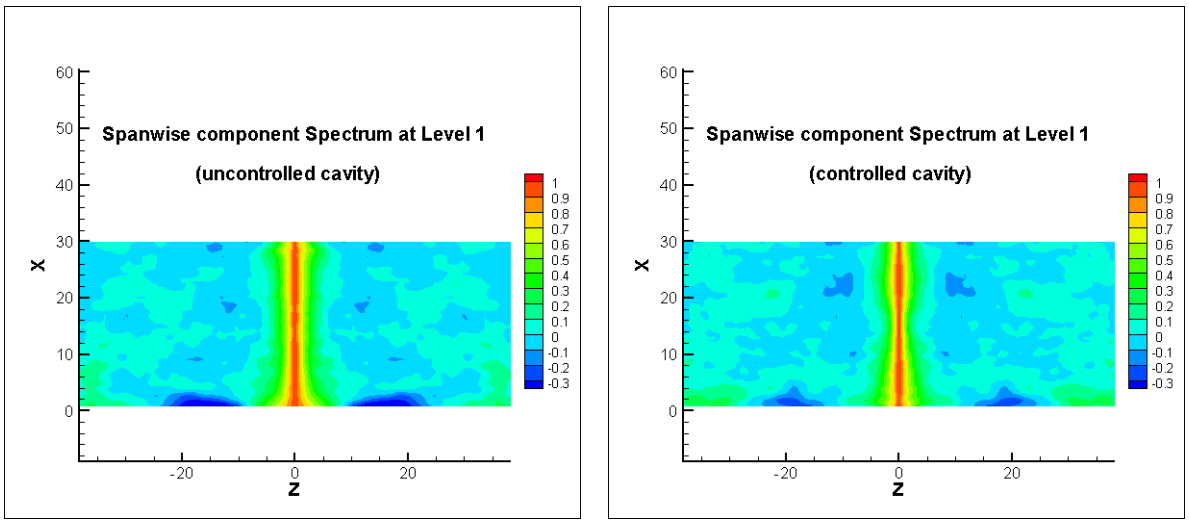

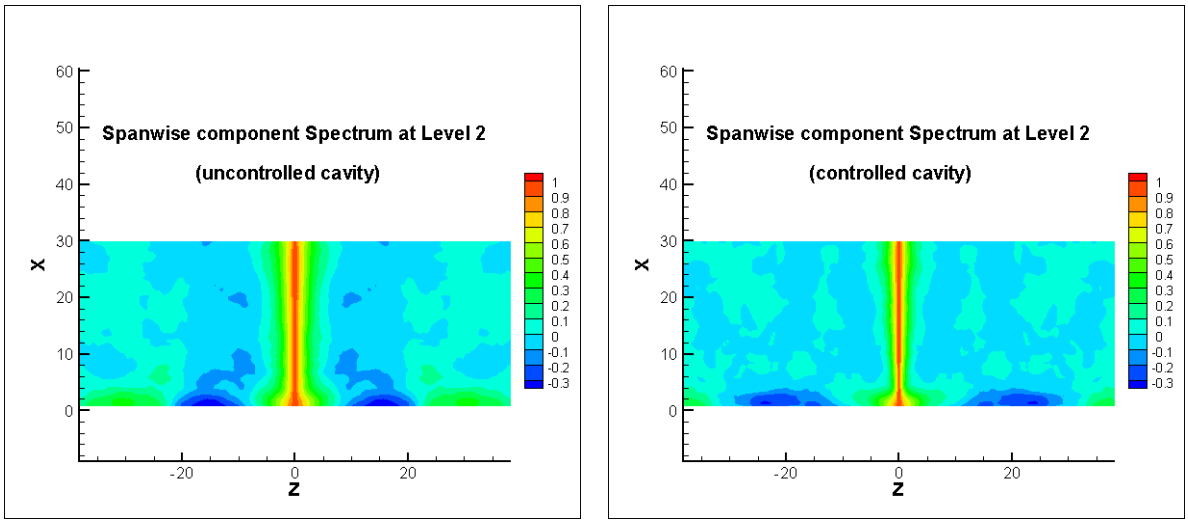

Figure 60. 2D overview of the Correlation $\rho_{u'u'}$ field along the z-dimension for all x-positions

a) Streamwise Variation

Superimposing a plotting corresponding to the vicinity of the leading edge to another corresponding to the mid-length of the cavity (Figure 61) we can clearly see the difference between the correlation fields. The behavior of the correlation function in the vicinity of the leading edge is different than in the rest of the cavity. A sequence of positive and negative peaks is observed, where the distance between successive peaks is about 3.5H.

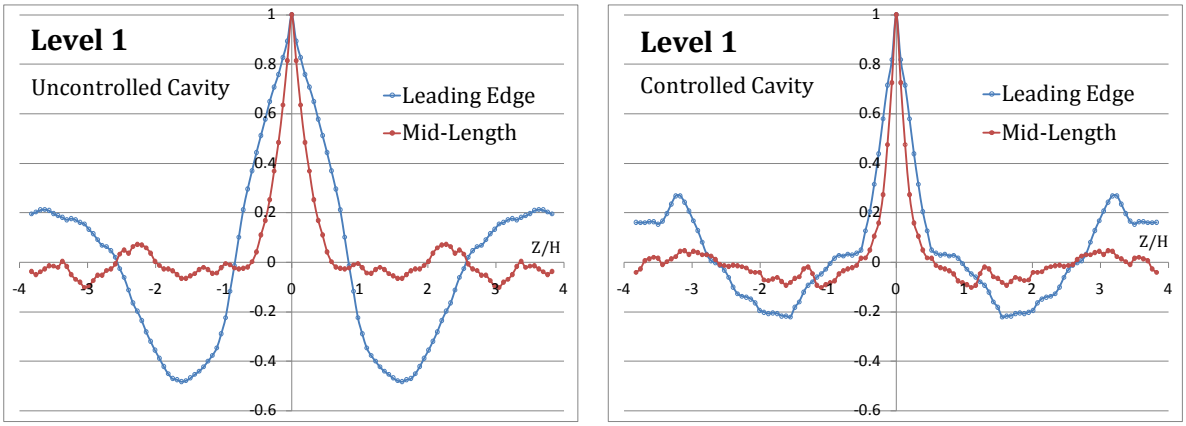

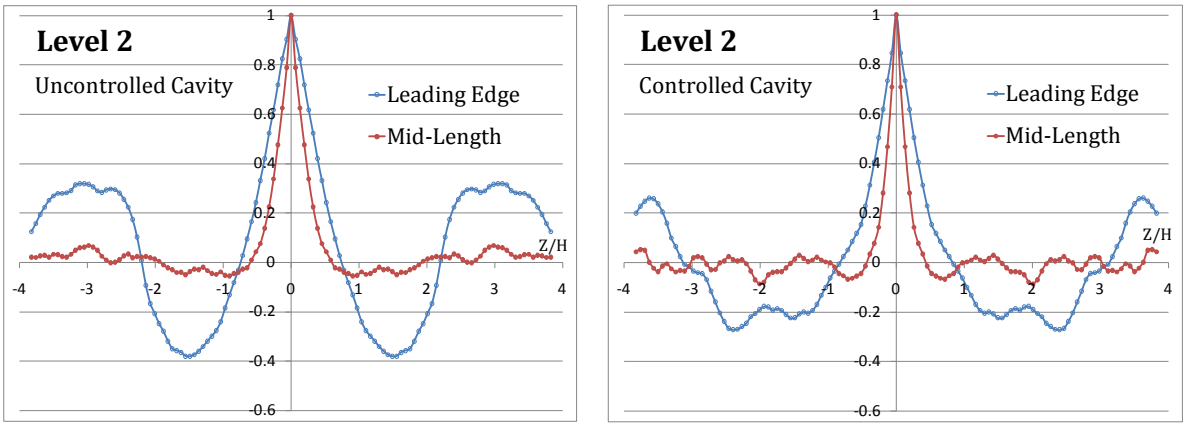

Figure 61. Correlation $\rho_{u'u'}$ along the z-dimension for two x-positions, at the leading edge (empty blue circle) and at the mid-length (full red circle)

As we move farther from the leading edge this configuration vanishes, giving place to another configuration characterized by a central peak that rapidly falls down followed by a flat field to the sides.

It is possible that these peaks are related to the presence of the cellular structures described in 6.2.1. Those impinging jets form in phase coherent structures whose spanwise statistical distance is 3.6H. The presence of negative peaks suggests that the cellular structures are characterized by colliding spanwise jets formed from the splitting of the streamwise jets after impinging on the wall.

b) Effect of the rod

The presence of the rod has a visible effect in the vicinity of the leading edge (Figure 62). The central peak is narrower and the negative side peaks are less deep. Beside, the distance between the peaks is increased. This could be attributed to the fact that the average distance between the cellular structures is increased due to the presence of the control device. Once again, the presence of the rod seems to provoke a loose of regularity in the flow configuration.

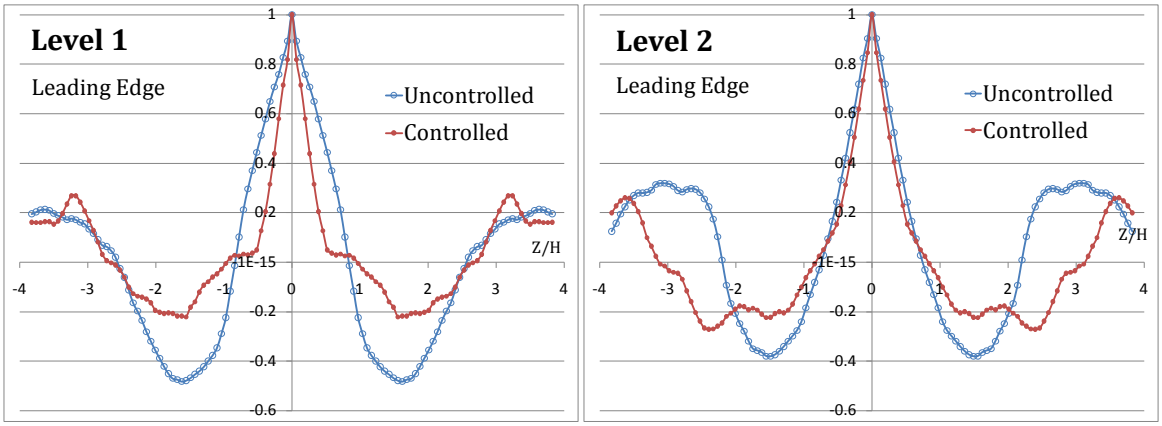

Figure 62. Comparison of $\rho_{u'u'}$ values for the controlled and for the uncontrolled cavity at a section near the leading edge

Remark 28. *The presence of the rod makes the correlations loose regularity.*

In the zones far from the leading edge the narrowing of the central peak due to the rod persists, while the rest of the lateral fields are flat (Figure 63).

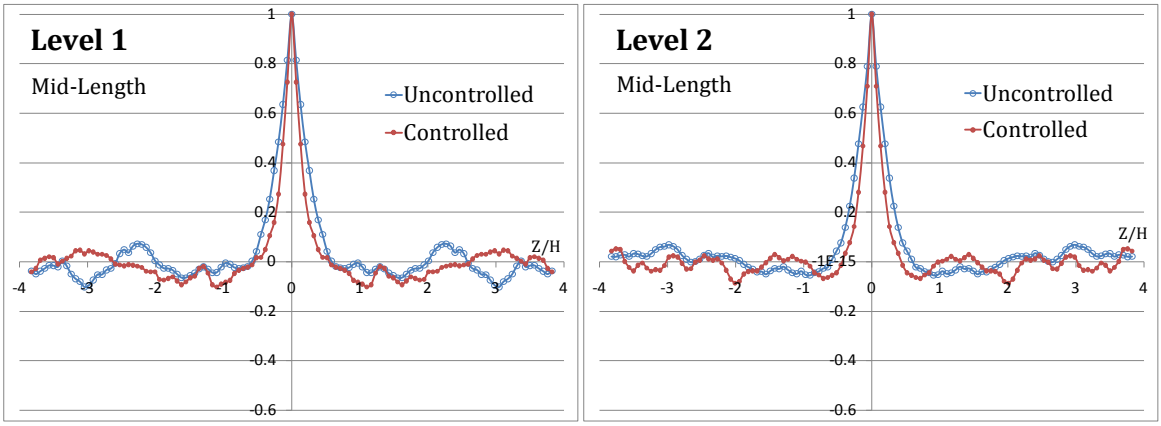

Figure 63. Comparison of $\rho_{u'u'}$ values for the controlled and for the uncontrolled cavity at the mid-length of the cavity

Remark 29. *The presence of the rod trends to flatten the profile making the side peaks less pronounced and the correlations trend to zero more rapidly.*

c) Level 1 vs. Level 2

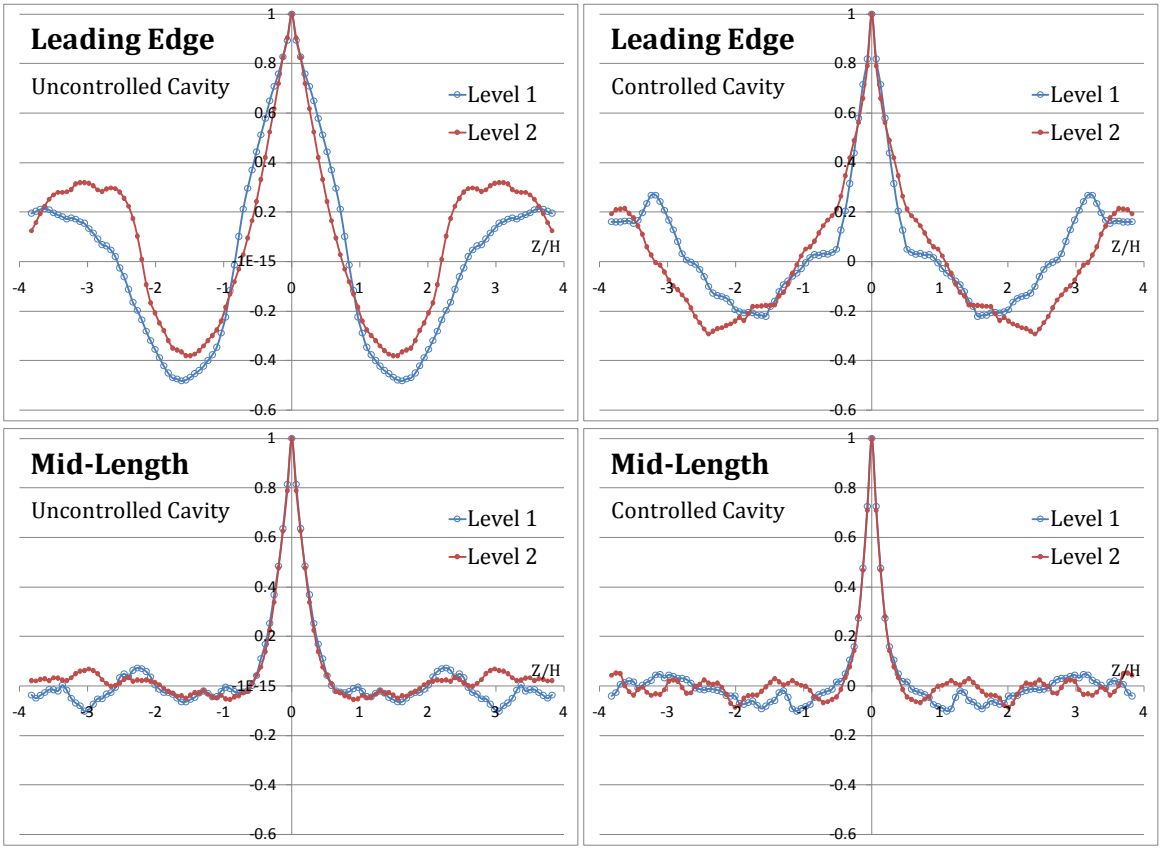

Figure 64. Comparison between the values of $\boldsymbol{\rho_{u'u'}}$ at the two levels

6.2.5 2D Spatial Velocity Correlations – Spanwise Component

Now, the spatial correlation of the fluctuating w'-component ($\rho_{w'w'}$) will be computed in the two dimensions of the *xz*-plane. This means that we will compute the correlation between one reference point $P(X_{ref}, Z_{ref})$ and all the rest of the points of the *xz*-plane, $P(X, Z)$.

Taking as the reference a point close to the leading edge a chessboard pattern comes out in the correlations field. The intensity of the correlation field rapidly diminishes as the reference point moves downstream. The average distance between two positive

correlated zones in the streamwise direction seems to be about 2H, this is 33% shorter that in the spanwise direction.

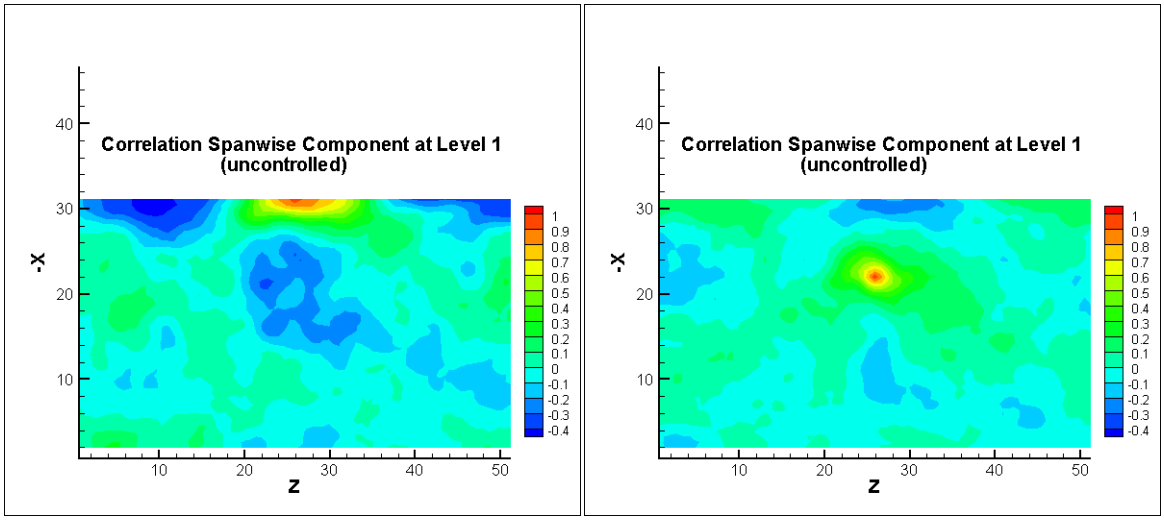

Figure 65. 2D Correlation $\rho_{u'u'}$ at Level 1 for two reference points. Uncontrolled cavity.

Let us consider now the controlled cavity (Figure 66). It seems that the chessboard pattern is less clear than in the uncontrolled case (Figure 65). The distances between streamwise correlated zones remains unchanged.

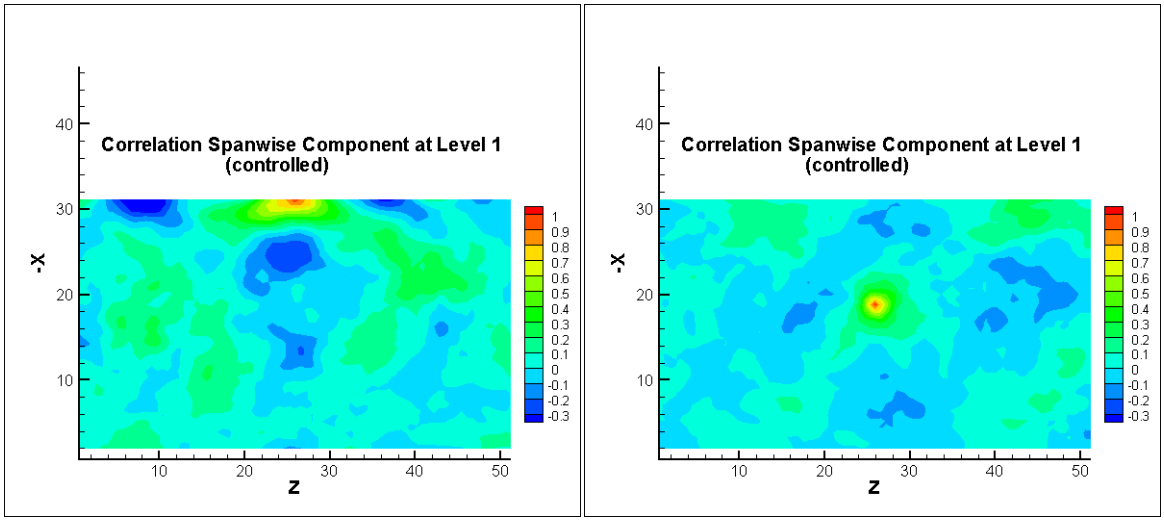

Figure 66. 2D Correlation $\rho_{u'u'}$ at Level 1 for two reference points. Controlled cavity.

At Level 2 (Figure 67 and Figure 68) it is not possible to describe a clear pattern. The correlations field shows values close to zero in the entire field except, as seen before, in the vicinity of the leading edge. Unlike the previous case, no correlation is seen in the streamwise direction.

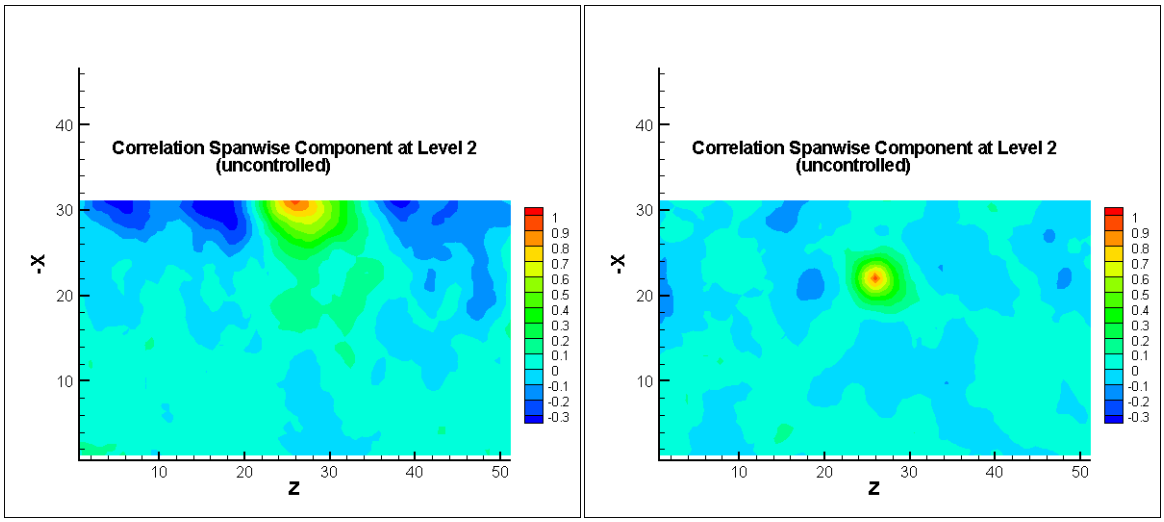

Figure 67. Correlation $\rho_{u'u'}$ at Level 2 for two reference points. Uncontrolled cavity.

The only apparent difference seen in the controlled case is that the field seems to oscillate more between positive and negative values, but always close to zero.

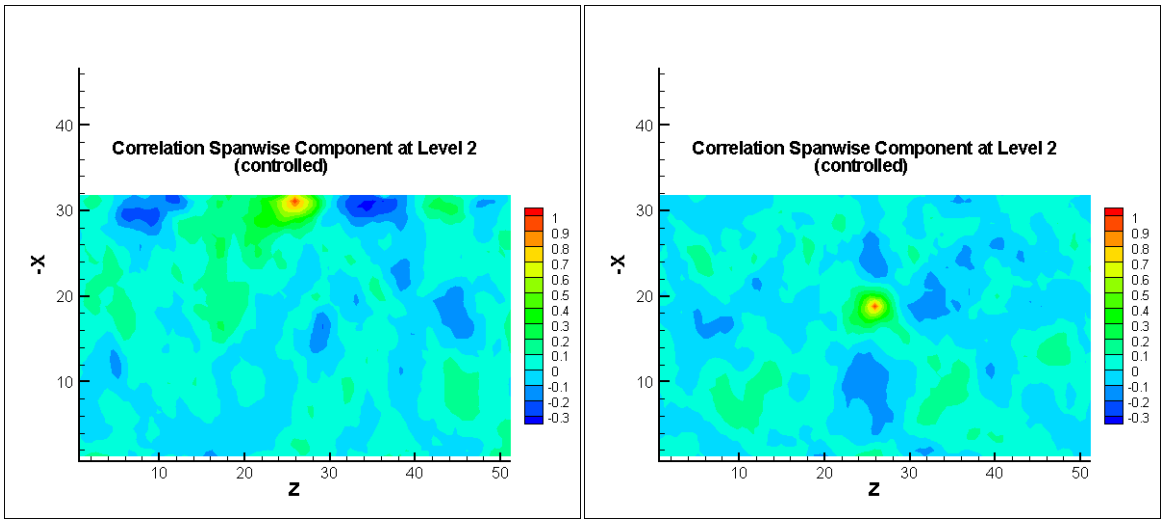

Figure 68. Correlation $\rho_{u'u'}$ at Level 2 for two reference points. Controlled cavity.

6.2.6 1D Spatial Velocity Correlations – Streamwise Component

The observation of the spanwise correlation analysis of the streamwise velocity in the plane (x,z) at level 2 (the closest to the shear layer) (Figure 69, Figure 70 and Figure 71)confirms the numerical results of Stanek et al. (2007), showing the dramatic lose of spanwise coherence already very close to the leading edge, in the case of the controlled flow. It should here be recalled that Stanek et al. 2007 affirm that this specific re-organization is responsible for the cavity tone suppression.

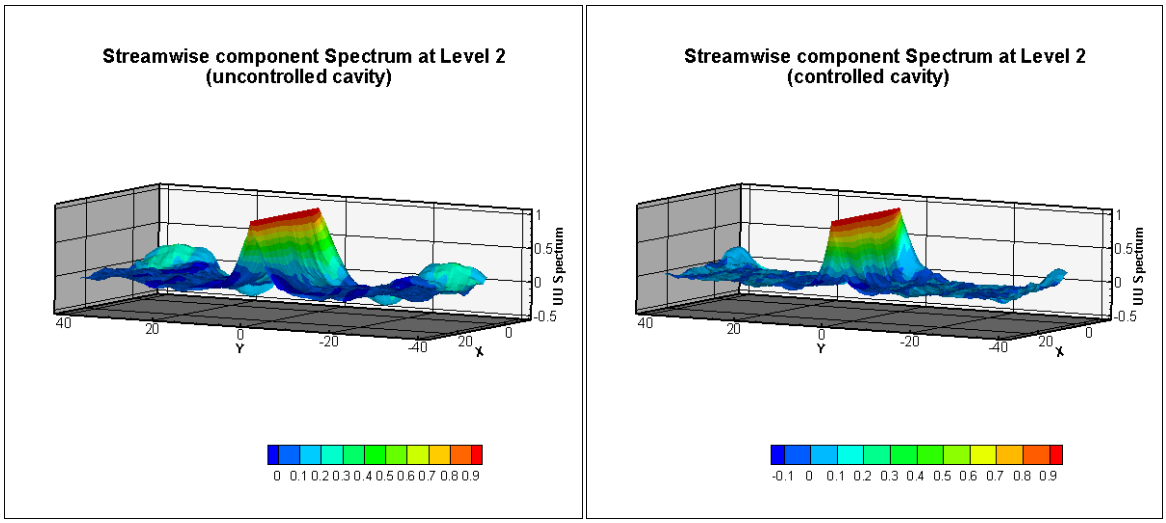

Figure 69. Streamwise Velocity Component Spectrum at Level2. 3D view.

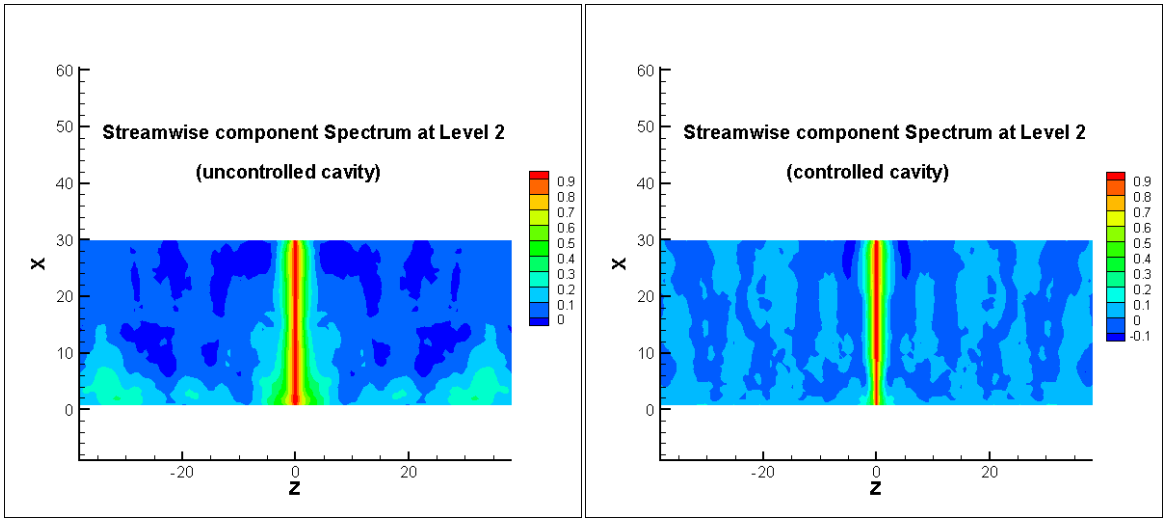

Figure 70. Streamwise Velocity Component Spectrum at Level2. 2D View.

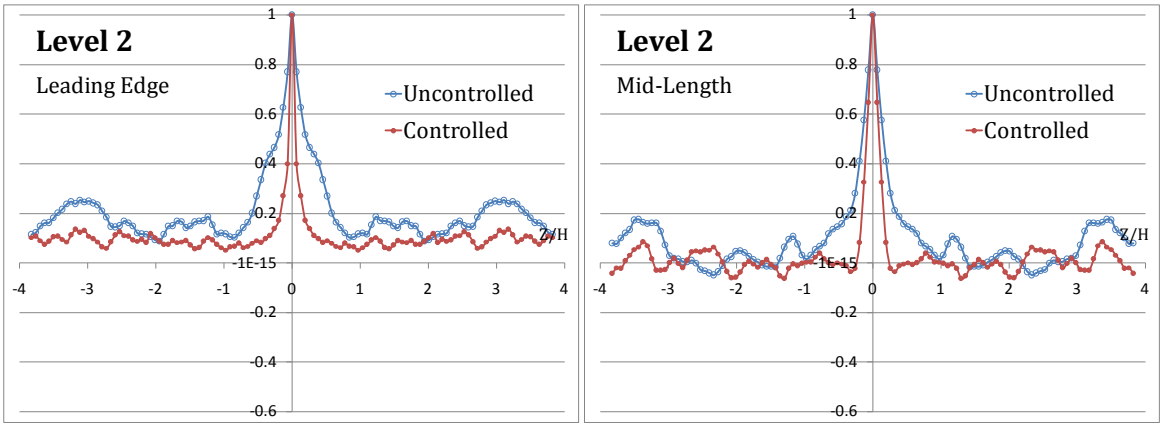

Figure 71. Streamwise Velocity Component Spectrum at Level2. 1D View.

Chapter 7

STABILITY ANALYSIS

The last aspect that we need to analyze to complete our theory explaining the physics of the suppression mechanism is the flow stability.

In order to try to understand in which way, the modification of the baseline flow produced by the control affects the stability characteristics of the shear layer at the cavity mouth, a linear stability analysis has been performed on the experimentally measured shear layer mean velocity profiles downstream the cavity leading edge. The flow has been assumed locally parallel in order to apply the classical Orr-Sommerfeld equation.

The theoretical approach to the Stability Theory is based on the assumption that laminar flows are affected by small disturbances superimposed to the basic flow. The theory endeavors to follow up in time the behavior of such. The decisive question to answer is whether the disturbances increase or die out with time. If the disturbances decay with time, the main flow is stable; on the other hand, if the disturbances increase with time it is considered unstable (54). When the disturbances can be considered small, Navier Stokes equations can be linearized thus allowing an analytical treatment.

According to Schlichting (54) many shear flows, like boundary layer flows, can be regarded as parallel with a good approximation because the dependence of the velocity U in the main flow on the $x\text{-}coordinate$ is very much smaller than that on **y**. Besides, as far as the pressure in the main flow is concerned, it is obviously necessary to assume a dependence on x as well as o $y, P(x,y)$, since the pressure gradient dP/dx maintains the flow. Considering the profiles shown in Figure 16 we will use such assumption to analyse our shear layer, considering it as a good approximation to parallel flow, too.

In the Orr-Sommerfeld hypothesis, the basic flow is assumed as:

$$U(y); \qquad V \equiv W \equiv 0; \qquad P(x,y) \tag{7.1}$$

Upon the mean flow we assumed superimposed a two-dimensional disturbance which is function of time and space. Its velocity components and pressure are, respectively:

$$u'(x,y,t); \qquad v'(x,y,t); \qquad p'(x,y,t) \tag{7.2}$$

Hence the resultant motion is described by:

$$u = U + u'; \quad v = v'; \qquad w = 0; \qquad p = P + p' \tag{7.3}$$

It is assumed that the base flow (7.1) is a solution of the Navier Stokes equations, and it is required that the resultant motion (7.3) must also satisfy the Navier Stokes equations. The fluctuating velocities (7.2) are taken to be small respect to the linear terms and their quadratic terms can be neglected. The task of the stability theory consists, then, in determining whether the disturbance is amplified or whether it decays, for a given mean motion.

After introducing the decomposition (7.3) in the Navier Stokes equations and neglecting the quadratic terms in u', v', with some simplifications, we obtain the linearised momentum and continuity equations.

$$\frac{\partial u'}{\partial t} + U\frac{\partial u'}{\partial x} + v'\frac{dU}{dy} + \frac{1}{\rho}\frac{\partial p'}{\partial x} = \nu\nabla^2 u'$$

$$\frac{\partial v'}{\partial t} + U\frac{\partial v'}{\partial x} + \frac{1}{\rho}\frac{\partial p'}{\partial y} = \nu\nabla^2 v'$$

$$\frac{\partial u'}{\partial x} + \frac{\partial v'}{\partial y} = 0$$

These equations can be reduced to a single one by expressing the disturbances u' and v' in terms of a streamfunction φ and then by considering the following form of solution:

$$\varphi(x, y, t) = \Phi(y) e^{i(\alpha x + \beta t)}$$

Here we consider the time evolution of spatial disturbancies, so that:

- α is the real wavenumber and $\lambda = 2\pi/\alpha$ is the wavelength of the disturbance.

- $\beta = \beta_r + i\beta_i$ is the complex pulsation

  Its imaginary part, β_i, called the amplification factor, represents the degree of amplification or damping.

  Its real part, β_r, is the circular frequency of the partial oscillation and

  Note that β_i determines the stability of the flow:

  $\beta_i < 0 \quad \Longrightarrow$ the laminar mean flow is stable

  $\beta_i > 0 \quad \Longrightarrow$ the laminar mean flow is unstable

- $\Phi(y)$ is the amplitude function of the fluctuations, which depends only on y as the mean flow.

The components of the perturbation velocity can be obtained by differentiating the stream function respect to x and y.

$$u' = \frac{\partial \varphi}{\partial y} = \phi'(y) e^{i(\alpha x + \beta t)}$$

$$v' = \frac{\partial \varphi}{\partial x} = -i\alpha\phi(y) e^{i(\alpha x + \beta t)}$$

Introducing these variables into the Navier Stokes equations, we obtain the final expression of the Orr-Sommerfeld equation. This is an ordinary fourth-order differential equation for the amplitude $\phi(y)$.

$$(U-c)(\phi'' - \alpha^2\phi) - U''\phi = -\frac{i}{\alpha R}(\phi'''' - 2\alpha^2\phi'' + \alpha^4\phi)$$

The Orr-Sommerfeld equation has been numerically solved by means a fourth-order finite difference method in the computational domain $-H \leq y \leq y_{max}$, with y_{max} six times larger than the boundary layer thickness. At y = -H the physical no-slip boundary conditions have been applied, while at y = y_{max} a free stream condition has been imposed. The time amplification coefficients β_i obtained from the numerical solution have been then transformed into spatial amplification factors α_i by means of the following relation (55).

$$\alpha_i = -\frac{\bar{k}\beta_i}{\frac{\partial\beta_r}{\partial\alpha}}$$

where β_r is the pulsation and α is the wavenumber. Figure 72 shows the resulting spatial amplification factor, normalized with the cavity depth H, as a function of the Strouhal number for a section downstream the cavity leading edge. Similar results have been obtained at different distances from the leading edge.

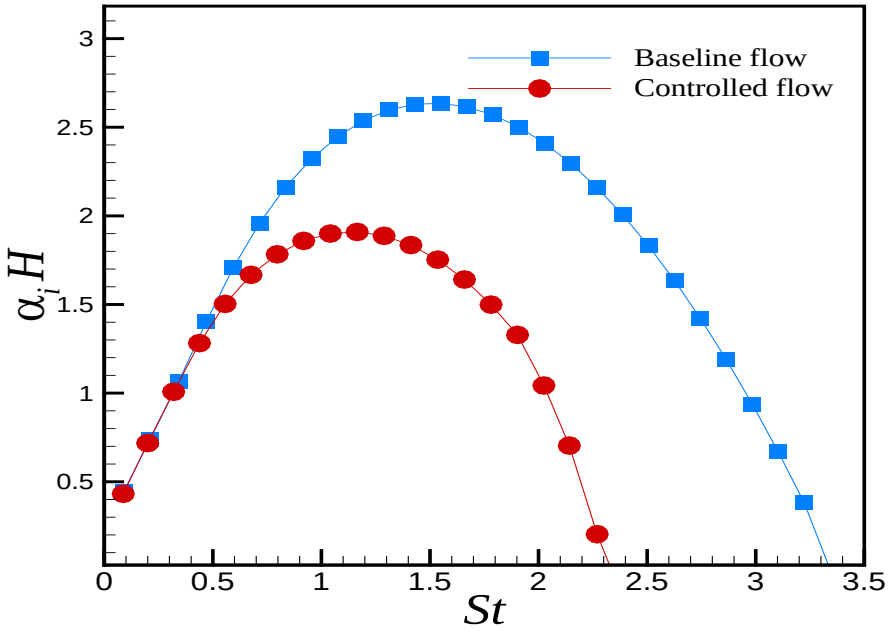

Figure 72. Dimensionless spatial amplification factor as function of the Strouhal number. Stability analysis on the velocity profiles at x/L=0.26 downstream the cavity leading edge.

A first observation to the results is that the instability corresponding to the second Rossiter mode at St = 1 lies within the envelope of the most amplified frequencies, i.e. the frequency of the second Rossiter mode is spatially amplified.

Remark 30. *The frequency of the second Rossiter mode is spatially amplified.*

Conversely the Strouhal number corresponding to the vortex shedding frequency from the rod (St=7.5) lies well outside the amplification envelope in the region where there is no spatial growth of the instability modes. Thus, the instability in the shear layer at the rod Von Karman shedding frequency, according to the linear stability theory, is expected to decay in the streamwise direction.

Remark 31. *The frequency of the vortex shedding should decay*

This analysis is in agreement with the facts observed in the time resolved sequences of snapshots, like the one in Figure 35 and with the results of the spectral analysis of the normal velocity component in the shear layer Figure 29 to Figure 33.

Moreover, the time resolved PIV sequences of the controlled flow shows that vortices of considerable intensity take form downstream in the shear layer, in the region close to the cavity trailing edge. These large structures can still be produced by the Kelvin-Helmholtz hydrodynamic instability because the range of unstable frequencies is only slightly reduced by the control (Figure 72). Sometimes these structures seem to appear as a consequence of the pairing between vortices present in the shear layer or between vortices in the shear layer and vortices coming out from the recirculation zone. In all cases, the main point is that their formation frequency is not regular. Again we conclude that the *regularity is lost with the control*, so no peak is produced but broadband oscillations.

Remark 32. *The regularity is lost with the control*

The present results support and extend what has been deduced by Panickar and Raman (2008). Their experimental and analytical results indicate that the effective mechanism for resonance suppression is the rapid spatial decay of all structures due to the high excitation frequency, lying outside the envelope of the most amplified frequencies in the shear layer. They performed spatial linear stability analysis on mean velocity profiles measured in the shear layer using a total pressure probe and acquired aero acoustic information by means of unsteady pressure measurements in the shear layer using a Kulite pressure probe and by means of a microphone located on the center of the cavity floor. Their contribution was essential, but their point type measurements did not allow to give a description of the dynamics of the vortical flow in the baseline and in the controlled cavity, as is done with the present field measurements. In Panickar and Raman (2008) results, the irregular formation of vortical structures in the controlled case at frequencies of the order of the second Rossiter mode, developing in the second half of the shear layer and amplifying going downstream, is not described.

Chapter 8

ANALYSIS OF THE RESULTS

The purpose of this chapter is to make a clear, ordered and systematic presentation of all the important findings that we made along the previous ones; especially, in the 'Analysis of the Data'. Many of these findings were previously highlighted in the text as 'remarks'. All of them will be grouped according to the physical interpretation that we make on them and to the role we assign to each of them. In that manner we will be offering them in a way that they will serve as the basis to explain the physic mechanism of the cavity oscillations suppression that will be proposed in the conclusions and that is the main goal of this work.

8.1 Absence of direct fluiddynamic effect of the rod on the Boundary Layer and on the first three thirds of the Shear Layer

The first important concept that comes out from our analysis that is that there seems to be no doubt that the presence of the rod and its vortex shedding do not have any direct fluiddynamic effect on the Boundary Layer and on the first two thirds of the Shear Layer (Remark 1, Remark 2, Remark 6 and Remark 8). The effect on the last third of the shear layer highlighted by Remark 3 and Remark 7 will be discussed in the next chapter and is compatible with the mechanism proposed later in this thesis. We must then exclude 4.3.4.(a) from our hypothesis

- Watching the mean velocity field in Figure 15 and Figure 16 we clearly see that between the wake of the rod (von Karman's vortex shedding) and Shear Layer there is a zone where the flow remains unaltered. The same occurs in the space

between the rod and the Boundary Layer. We can also see in Figure 17 that the streamwise component of the velocity is not altered by the presence of the rod.

- Something similar can be seen in the u'_{rms} field (Figure 18) and in the v'_{rms} field (Figure 19). A zone of unaltered flow separates vortex shedding from the Shear Layer and the rod from the Boundary Layer.

- Let us now evaluate carefully the incoming Boundary Layer (Figure 22 and Figure 23) at the Leading Edge. In the controlled cavity it develops normally (similar to the uncontrolled cavity and reproducing the Blasius profile) under the level of the rod. At the level of the rod a depression in the velocity appears, and over that level the flow recovers the velocity corresponding to the cavity without rod. The same behavior is shown in Figure 27.

- Following the analysis of the Shear Layer, we see in Figure 24 that the mean streamwise velocity along the shear layer is not affected by the presence of the rod. In Figure 25 we see that also the Momentum Thickness is unaltered. Finally Figure 26 shows a slight increase of the Vorticity Thickness with the presence of the rod, mainly in the last third.

- Figure 35 shows the swirling strength fields, calculated with the Lambda-Ci method. As highlighted in Remark 15 no direct interaction is seen between the vortex shedding and the shear layer or the boundary layer.

All those findings allow us to assert that the suppression effects are exclusively due to the High Frequency Forcing.

It is important to remark that, before us, other authors made a big effort to demonstrate that the suppression effect of the rod in crossflow technique was not due to the direct fluiddynamic effect of the rod on the Boundary Layer, as others had hypothesized before (see 4.3.4.(a)). Panickar and Raman in 2008 (9) used a rod covered with a thin spiral filament to suppress the vortex shedding and then an uncovered one to compare. They found that the first one produced no suppression effect of the cavity oscillations, while the second did normally.

8.2 High Frequency Vortex Decay

The second concept we must highlight is related to the evolution of the high frequency vortices shed from the rod. Their intensity decays as they are convected downstream by the flow until they extinguish.

- As highlighted by Remark 4, Figure 18 and Figure 19 show that both components of the fluctuating velocity, u'_{rms} and v'_{rms}, decay donwnstream along the wake of the rod.

- In Figure 34 a sequence of spectra corresponding to the fluctuating *v*-component of the instant velocity is plotted for several points along the cavity length at the level of the rod. It is clearly seen that the peak corresponding to the vortex shedding (St=7.5) decrease downstream (Remark 12) until it disappear around X/L≈0.75. Also Figure 29 and Figure 30 show the same effect highlighted in Remark 11.

- In Figure 35, where the swirling strength fields, calculated with the Lambda-Ci method are shown, the vortex shedding from the rod is clearly visible. It is also easy to notice that the intensity of the vortices decay downstream (Remark 14).

- The space correlation coefficients plotted in Figure 36, Figure 37, Figure 38 and Figure 39 show that the small correlated zones vanish downstream (Remark 22).

- The theoretical stability analysis performed in Chapter 7 shows what is expressed in Remark 31: *"The intensity of the vortex shedding must decay"*. Effectively, watching Figure 72 we notice that any perturbation with a frequency higher that St=3.4 falls out of the amplification envelope.

8.3 Amplification of the Low Frequency Vortices

The third concept we want to show is about the evolution of the low frequency vortices originated in the shear layer. They are amplified as the travel downstream.

- As highlighted by Remark 4, Figure 18 and Figure 19 show that both components of the fluctuating velocity, u'_{rms} and v'_{rms}, grow up donwnstream along the Shear Layer.

- The v-component Velocity Spectra calculated for several points along the cavity mouth is plotted in Figure 29 to Figure 33 (Remark 11). In those figures it is clearly seen that the peaks at low frequencies, coincident with the Rossiter 2nd and 3rd modes grow up downstream. This is clear evidence that those frequencies are amplified.

- The w-component Velocity Spectra calculated for several points 1mm under the cavity mouth is plotted in Figure 57. Peaks corresponding to the Rossiter 2nd and 3rd modes are detected growing up downstream.

- The Swirling Strength intensity calculated by the Lambda-Ci method shows that, in the non-controlled cavity, regularly spaced vortices (periodically generated from Kelvin-Helmholtz instabilities) appear in the first third of the mouth and they grow up as they travel downstream (Remark 13). In the controlled cavity those vortices are not regularly spaced and they appear more downstream. Figure 35 shows one snapshot for each one of the cases.

- The theoretical stability analysis performed in Chapter 7 shows what is expressed in Remark 30: *"The frequency of the second Rossiter mode is spatially amplified"*. Effectively, watching Figure 72 we notice that perturbations with frequencies near the Rossiter modes lie in the highest sector of the amplification envelope.

- The space correlation coefficients plotted in Figure 36, Figure 37, Figure 38 and Figure 39 show that the large correlated zones are amplified as they are placed more downstream (Remark 22).

8.4 *Triggering* phenomenon

Until this moment, we have seen in Sections 8.2 and 8.3 the description of two isolated mechanisms. In this Section we will show clear evidence of a subtle but effective interconnection between them, by means of a mechanism of triggering the instabilities. This fact constitutes the angular stone of the physic mechanism that will be proposed in the next Chapter.

- The first sign that shows this triggering effect can be found in the spectra shown in 6.1.8, especially in Figure 29 and Figure 30. In those spectra, corresponding to points placed at the cavity mouth level, peaks at frequencies corresponding to the vortex shedding from the rod are visible. Despite the absence of direct fluiddynamic effect of the rod on the shear layer (8.1), oscillations reproducing the vortex shedding frequency are found in it.

- Possibly, the clearest sign to support the existence of this phenomenon is found with the vortex detection method (Section 6.1.9). In the image on the right of Figure 35 we can see that a line of vortices reproducing the frequency of the vortex shedding is present over the cavity mouth. The video this snapshot is taken from shows that this vortex line reproduces from the distance the vortex shedding as a mirror.

We consider that this effect takes place when the instabilities, naturally present in Shear Layer, are affected by disturbances (like pressure waves) coming from the rod and from the vortex shedding (Remark 16).

It is useful to remark that vortex line decays and disappear downstream.

8.5 Loss the Regularity

Considering that the phenomenon we are studying and controlling is originated due to the presence of periodicity resulting from the Rossiter cycle, the evaluation of this periodicity and its suppression is fundamental to understand the cancellation mechanism. Following, we will evaluate the cases in which periodicity is detected in the uncontrolled cavity, and is eliminated by the presence of the control device.

- In Section 6.1.9 the results obtained from the Lambda-Ci vortex visualization method are showed. According to Remark 13 "…*vortices generated periodically from Kelvin-Helmholtz instabilities…"* are found in the Shear Layer corresponding to the uncontrolled cavity. Later, in the evaluation of the controlled cavity, it is stated in Remark 17 that after the disappearance of the high frequency vortices only non regular vortices appear in the shear layer.

- The spectra showed in Sections 6.1.8 and 6.2.3 are a strong evidence of the loss of regularity, since the peaks in the spectra show regularity in the velocity concentrated in a given frequency.

- The correlations in the xy-plane show a clear evidence of regularity in the non-controlled cavity case. Analyzing the $\rho_{u'u'}$ correlation the Remark 18 describes the finding of "A sequence of regularly spaced correlated regions" in the uncontrolled cavity (Figure 36) that is not found in the controlled cavity (Figure 37). In the analysis of $\rho_{v'v'}$ an identical situation is found (Figure 38 and Figure 39).

It is important to remark that in the controlled cavity there are still vortices which are amplified downstream, and the shear layer still gets thicker. Only the regularity is lost.

Chapter 9

SUPPRESSION MECHANISM

At the beginning of this thesis we stated that: "The contribution to the understanding of the physical phenomena leading to the suppression of the pressure peaks in a cavity flow by high frequency forcing, constitutes the central core of this thesis and its main objective". According to this objective, in this chapter we will explain our hypothesis about the physical mechanism that makes the rod in crossflow such an efficient flow control device to suppress the self sustained oscillations, which constitutes the main undesired effects in cavity flows. Our hypotesis will be based on the exhaustive analysis of the experimental data obtained with Time Resolved Particle Image Velocimetry techniques, together with a large amount of evidence that was obtained from other authors' scientific publications. All this has been presented in a methodical manner along the whole work and systematically summed up in the previous chapter.

9.1 Cavity without Control

The Rossiter cycle, has already been introduced in section 3.5 as the mechanism governing the self sustained oscillations in cavity flows. Now, we will see a detailed illustrated step-by-step description of this mechanism since this will be very useful later, in section 9.2, to better understand how the control device is able to alter it.

9.1.1 Step 0 – Time = T_0

Let us consider the ideal situation in which the Shear Layer on the cavity mouth is unstable in all its length, but no disturbance has acted on it, yet.

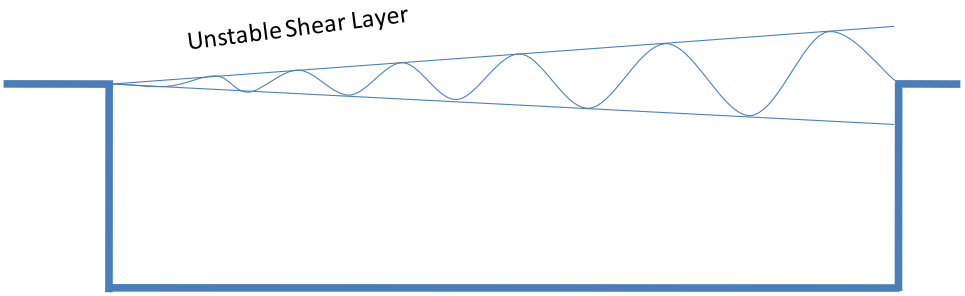

9.1.2 Step 1 - Amplification

A low frequency (10Hz for our cavity) disturbance triggers the instabilities in the Shear Layer generating a vortex that is convected downstream by the flow. We say that this disturbance is the *"effective trigger"* since it is the one that generates the vortex. The reason for its "low frequency" will be understood later.

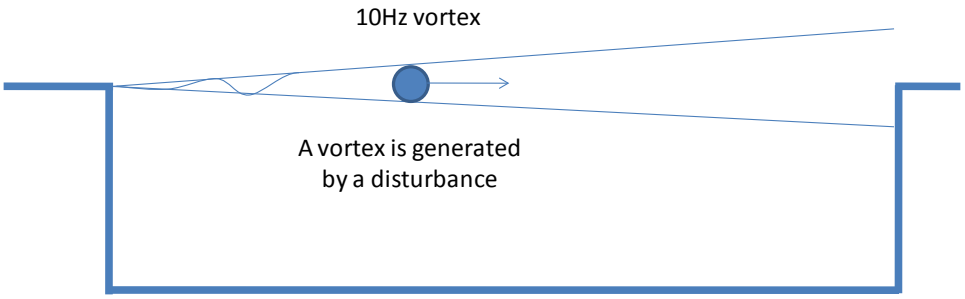

As we have already seen the low frequency corresponding to this cavity lies well inside of the amplification envelope (Figure 72). For this reason the vortex will grow up (Remark 30) as it is convected downstream. Behind the vortex, the instabilities in the shear will start developing again.

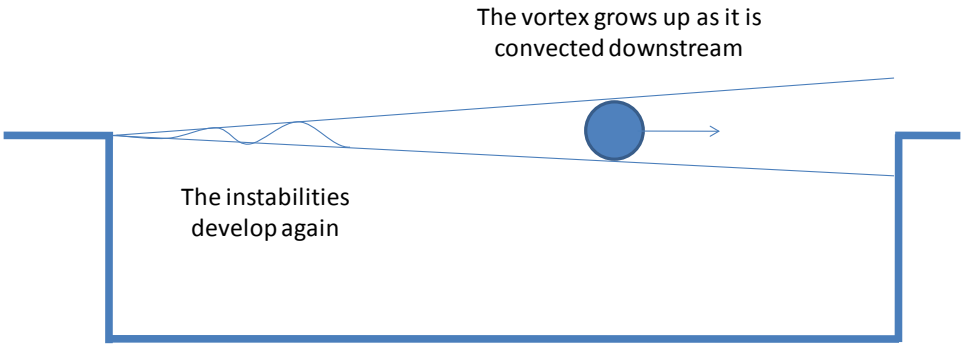

9.1.3 Step 2 - Interaction

When the vortex impinges on the trailing edge of the cavity generates acoustic waves that propagate in all directions, in particular upstream by the inside of the cavity.

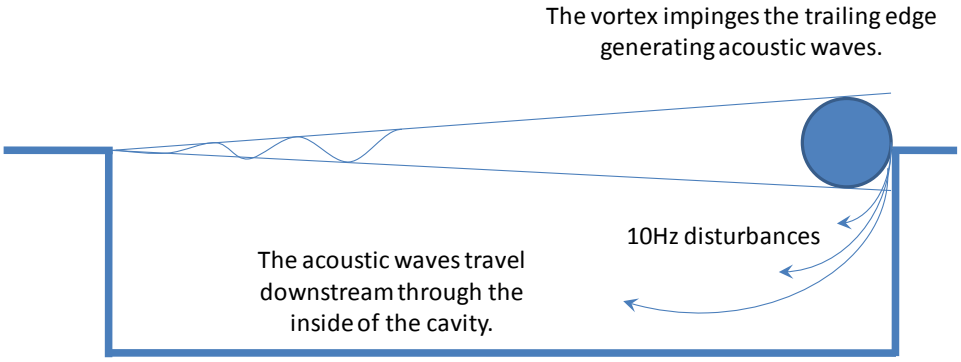

Those disturbances are generated every time that a vortex reaches the trailing edge; therefore, its frequency will be the same as the vortices frequency.

9.1.4 Step 3 – Feed-Back

The acoustic waves propagate upstream through the inside of the cavity.

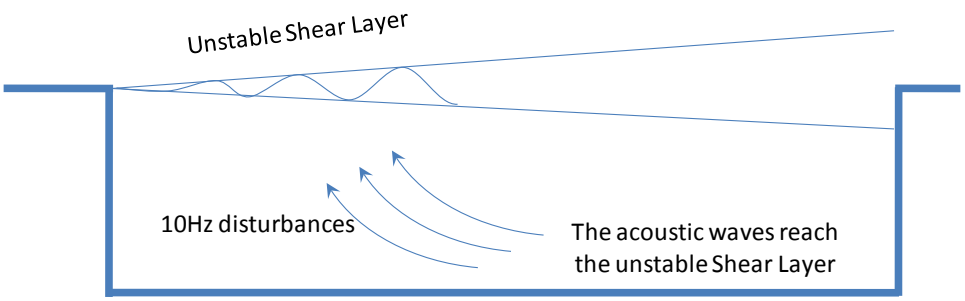

9.1.5 Step 4 – Receptivity

When the acoustic waves reach the unstable (receptive) Shear Layer they *'trigger'* it generating a new vortex and completing the cycle. Again, we say that these disturbances are the *"effective triggering"* since they generate the vortices.

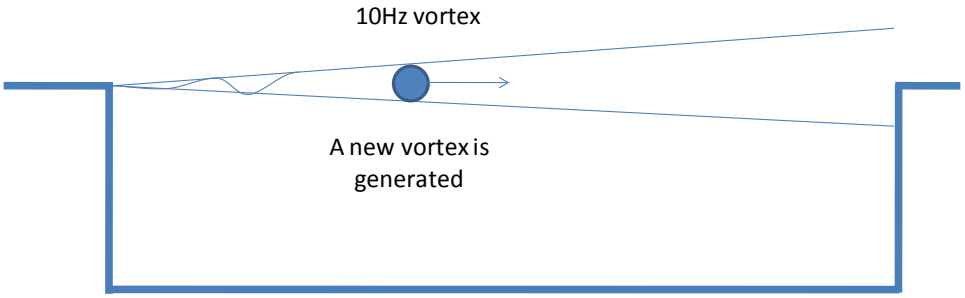

The frequency of the oscillations is defined by the inverse of the total time of the whole process. The Rossiter formula introduced in section 3.5 is based in these principles.

9.2 Cavity with Control

We will now start the explanation of the new concepts developed for this thesis.

The physical mechanism activated in the cavity by the presence of the rod will be showed in the following simple steps.

9.2.1 Step 1

The disturbances produced by the rod, whose frequency is one order of magnitude higher than the Rossiter modes, act immediately on the Shear Layer *"triggering"* the instabilities This means that the vortices in the shear layer will reproduce the vortex shedding frequency (see Figure 35).

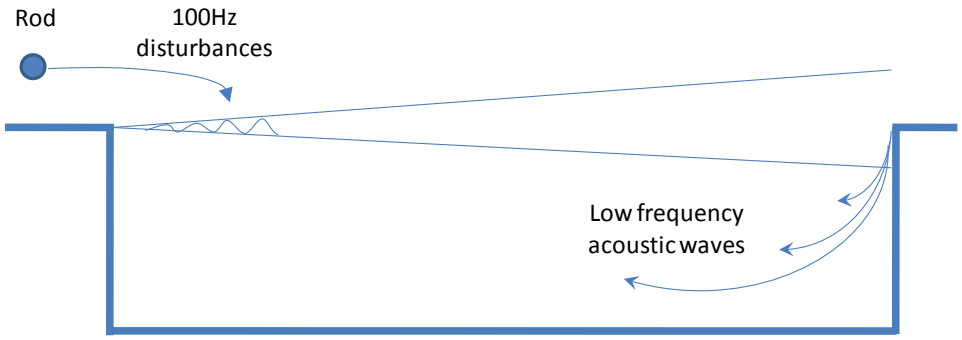

9.2.2 Step 2

The vortices in the Shear Layer are generated at the frequency of the disturbances coming from the rod. Since the disturbances coming from the trailing edge are of a lower frequency, they either arrive late finding the Shear Layer not receptive, since a vortex has been just generated, or arrive together with a disturbance from the rod. Anyhow, they are not able to produce any periodic effect on the Shear Layer. In other words, the high frequency disturbances take the control becoming the *"effective forcing"* (again see Figure 35).

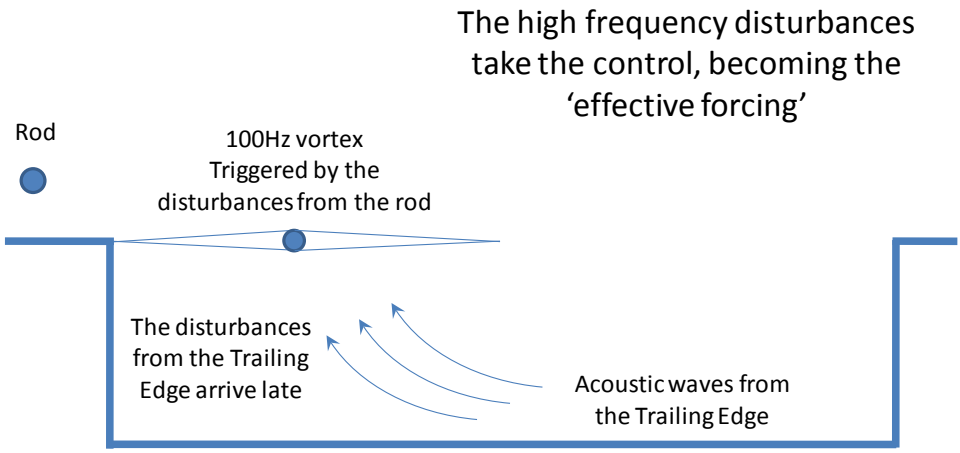

In this point we can say that the Rossiter cycle was broken.

9.2.3 Step 3

As we have already discussed (Remark 11) the high frequency vortices rapidly decays downstream and vanish (see Figure 29 to Figure 33).

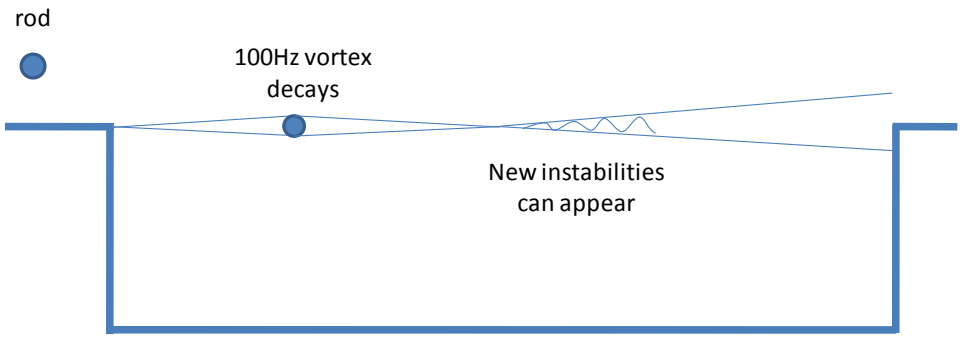

New instabilities appear in the Shear Layer after the high frequency vortices disappeared.

9.2.4 Step 4

Sometimes, in the downstream half of the cavity an isolated non-periodic vortex is generated, is amplified and impinges the trailing edge.

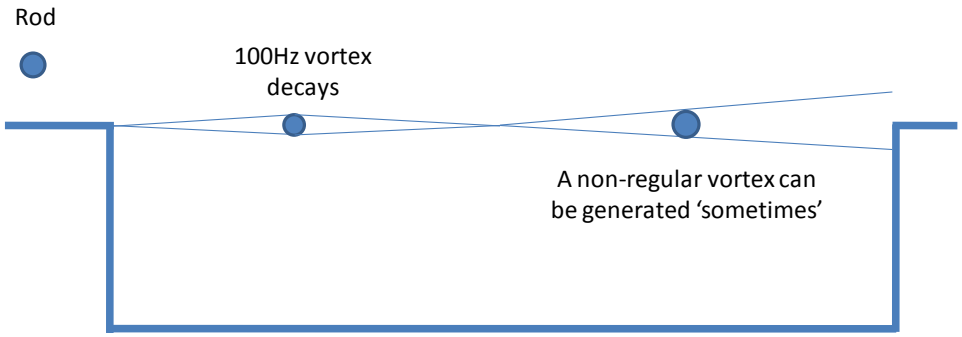

9.2.5 Step 5

Naturally, the impingement of the vortex over the Trailing Edge generates Acoustic Waves. However, from the process that generated them we can clearly infer that they are not regular at all.

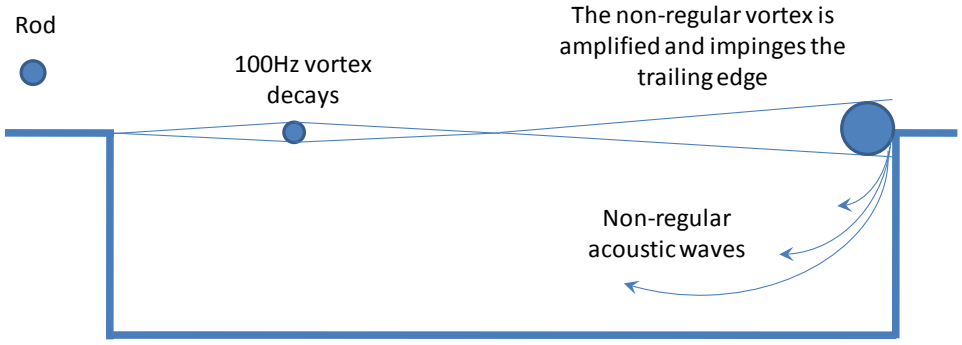

Finally we can say that no sign of periodicity is found in this process. The Shear Layer still shows strong fluctuations and big vortices can be found impinging over the Trailing Edge, but the periodic phenomena that generated the pressure peaks disappeared as the Rossiter Cycle was broken.

Chapter 10

CONCLUSIONS

Time resolved PIV measurements have been applied to nominally 2D cavity flows having the ratio length-to-depth L/H=3. The primary objective was to contribute to the understanding of the physics governing the suppression mechanism of the cavity flow self-sustained oscillations by means of a cylindrical rod positioned transversally just upstream the cavity entrance. The rod was positioned at the external edge of the incoming boundary layer (section 5.1). The measurements made especially for this work, described in previous chapters and analyzed in Chapter 6, together with the results obtained by other authors, which have been carefully studied, confirm the effectiveness of this device for the cavity self-sustained oscillations suppression.

As reported in 4.3.4, several physical mechanisms have been hypothesized to explain the cavity tone suppression resulting from the use of the cylinder in cross-flow. The most accredited mechanisms from that section are:

a) Direct interaction: The suppression effects of the rod are due to the direct interaction of the vortex shedding with the Shear Layer instabilities.

b) Alteration of the impingement region: The cylinder lifts-off the shear layer and causes the impingement region to be altered.

c) Reorganization of the vorticity field in the shear layer: The presence of the rod lead to a dramatic reorganization of the vorticity field in the shear layer

producing its stabilization. This would be due to the spanwise breakdown of the initially spanwise coherent pair of counter-rotating vortices in the cylinder wake.

d) Stability: High frequency forcing alters the stability characteristics of the mean flow in the shear layer.

It is expected that more than one of these mechanisms could act together, since they are not mutually exclusive and they are supported by their authors with solid experimental a theoretical bases (see references at section 4.3.4). However, the present experimental results almost exclude contributions to the observed tone suppression by mechanisms (b) and (d). As highlighted in Remark 9, Figure 28 does not show any evidence of lift-off of the shear layer induced by the rod to justify the cavity tone suppression, excluding mechanism (b). While, Figure 72 shows that the presence of the rod does not alter significantly the stability characteristics of the shear layer. Namely, the spatial amplification factor and the range of unstable frequencies are only slightly reduced by the control. This seems to exclude mechanism (d).

Regarding mechanism (c), the present results show that a rearrangement of the vorticity field takes place, due to the presence of the rod, producing reduction of the spanwise coherence of the vortical structures in the shear layer. As observed by Stanek et al. (2007) (44), this vorticity reorganization is in the direction of more random field, therefore pushing the flow towards stability and contributing to the cavity tone suppression.

In addition, as it has been widely discussed in section 8.1, the results visualized in Figure 18, Figure 19 and Figure 20 show that a direct interaction between the cylinder wake and the shear layer takes place only in the region near the cavity trailing edge. It may be argued that this interaction also contribute to a less two-dimensional organized motion of the vortices in the shear layer and to the reduction of the negative vorticity in the shear layer due to an expected unwind action by the positive Karman vortices in the cylinder wake lower side.

The scenario appearing from the present result, for the controlled flow, is the following (see also Chapter 9). The high frequency excitation, due to the unsteady wake of the cylindrical rod, induces and controls an instability process in the shear layer, near the leading edge, by forcing it at a frequency corresponding to Von Karman vortex shedding frequency (Figure 35) (see also sections 8.4 and 9.2.2). As shown by the stability analysis and as found by Panickar and Raman (2008) (9), this high frequency excitation lies outside the envelope of the amplified instabilities (Figure 72) then decays rapidly as it is convected

downstream along the shear layer (Figure 29 to Figure 33) (see section 9.2.3). Moreover, vortical disturbances at a frequency of the order of the tone frequency for the baseline flow, appear in the controlled shear layer from about two/third of the cavity and are amplified going downstream (Figure 35 and Figure 33) (see also9.2.4). These vortices, possibly due to the previously mentioned mechanisms (a) and (c), do not show the regular behavior expected in the case of self-sustained oscillation conditions, as in the case of the non-controlled flow. They give rise only to a modest broadened peak in the velocity spectra (see Figure 31 to Figure 33).

A global analysis of the flow field made in section 6.1.11 by looking at the cavity instantaneous drag per unit span (Figure 41) shows, for the baseline flow, a drag fluctuation of relatively high frequency superimposed to a lower frequency fluctuation of larger amplitude (about 2Hz). The observed high frequency corresponds to the frequency of the cavity tone (St = 1) and it has been attributed to the dynamics of the vortical structures along the cavity mouth. The superimposition of the Conditioned Averaged Velocity Field and Lambda-Ci Field clearly shows that the approaching of a vortical structure to the trailing edge (Figure 45) induces inflow, causing high drag, conversely, a vortical structure passing the trailing edge (Figure 47) induces outflow, causing low drag. A similar process is observed for both, controlled and non-controlled flows, but the drag oscillations show considerable variation in frequency and appear to be of smaller amplitude in the second case with respect to the one in the baseline flow.

The low frequency oscillation has been tentatively attributed to a kind of flapping motion involving the whole cavity shear layer. This low frequency oscillation is present also in the case of the controlled flow with comparable frequency and amplitude.

Chapter 11

FUTURE WORKS PROPOSAL

When a scientific research work is done, mainly if this is of the experimental type, besides the expected results, that one will find if the hypothesis formulated were correct, other unexpected results may appear. These unexpected results, whose detection might depend on the capacity of observation of the researcher, are frequently the starting point of new investigations. It was frequently seen in the history of science that unexpected results, secondary to a given research, finally became much more important that the investigation that originated them.

In our particular case, we can say that the three lines of research that should be followed in the future are:

1. The study of the Low Frequency oscillations in the drag.

   This effect was found and described in Section 6.1.11 and is clearly observe in Figure 41. As stated in the Conclusions: *"The low frequency oscillation has been tentatively attributed to a kind of flapping motion involving the whole cavity shear layer"*. However, further research is required to discover the origin of this effect.

2. The study of the Low Frequency spanwise oscillations.

   This effect was described in Section 6.2.3 and highlighted by Remark 26. Their existence cannot be completely assured, since the acquisition time is too short. For that reason it would be interesting to perform new experiments in this sence.

3. The study of the pressure field calculated from PIV data.

   Since the present work did not include pressure measurements, it would be very interesting to calculate the pressure field and the pressure spectra using an acoustic analogy like the one described in Haigermoser 2009 (13) and Koschatzky et al. 2011 (56).

PERSONAL EXPERIENCE OF THE AUTHOR

Following Ph. D. Studies in one of the best technological institutes of Europe was, undoubtedly, a very enriching experience for me. This is not only due to the quality of the Education and Research of Politecnico di Torino and its staff, and the modern technologies that I could learn and apply there, but also due the human quality of its people.

Being part of a Marie Curie Project, and living and working in the core of Europe, made it possible to be continuously in touch with people from the most different origins and nationalities (Italy, Germany, U.K., Czech Republic and India, among others). Besides, I had the opportunity of visiting the different institutions which were part of the AeroTraNet project in three different Countries. All this was an enriching and unforgettable experience that made me know the different ways of studying, working and living in all those places, and make professional contacts and good friendships that will, hopefully, last for all the rest of my life.

WORKS CITED

1. *Acoustic Radiation from two-dimensional Rectangular Cutouts in Aerodynamic Surfaces.* **Krishnamurty, K.** August 1955. NACA Tech Note 3487.

2. *A theoretical and experimental investigation of the acoustic response of cavities in an aerodynamic flow.* **Plumbee, H. E., Gibson, J. S. and Lassiter, L. S.** March 1962. WADD TR-61-75.

3. *Wind-tunnel experiments on the flow over rectangular cavities at subsonic and transonic speeds.* **Rossiter, J. E.** s.l. : Aeronautical Research Council Reports and Memoranda, October 1964. No. 3438.

4. *Experiments on two dimensional base flow at subsonic and transonic speeds.* **Nash, J. F., Quincey, V. G. and Callinan, J.** January 1963. ARC R&M 3427.

5. **Schlichting, Hermann.** *Boundary-Layer Theory.* s.l. : McGraw-Hill, 1968, VII.b., pp. 121-124.

6. *Some measurements of flow in a rectangular cutout.* **Roshko, A.** August 1955. NACA Tech Note 3488.

7. *Review of active control of flow-induced cavity resonance.* **Cattafesta, L. N., et al.** June 2003. AIAA 2003-3567.

8. *Experimental and predicted acoustic amplitudes in arectangular cavity.* **Dix, R. E. and Bauer, R. C.** 2000-0472, AIAA Journal.

9. *Cavity resonance suppression usin high frequency excitation: The mystery of the cylinder-in-crossflow revisited.* **Panickar, P. and Ganesh, R.** May, 2008, AIAA 2008-2853.

10. *On edge tones and associated phenomena.* **Powel, A.** s.l. : Acustica, 1953, Vol. 3, pp. 233-243.

11. *On the edgetone.* **Powel, A.** 4, s.l. : Journal of Acoustics Society of America, 1961, Vol. 33, pp. 395-409.

12. *Review - Self-sustaining oscillations of flow past cavities.* **Rockwell, D. and Naudascher, E.** s.l. : Journal of Fluids Engineering, 1978. 100:152-165.

13. *Derivation of the instantaneous pressure and the application of an acoustic analogy to PIV data from a rectangular cavity flow.* **Haigermoser, Christian.** 2008.

14. *Drag of rectangular cavities in supersonic and transonic flow including the effects of cavity resonance.* **McGregor, O. W. and White, R. A.** 8:1959-64, AIAA Journal.

15. *Vibration Analysis for Electronic Equipment, Second Edition.* **Steinburg, D. S.** s.l. : John Wiley & Sons, Inc., 1988. ISBN 0-471-63301-1.

16. *On the tones and pressure oscillation incuded by flow over rectangural cavities.* **Tam, C. K. W. and Block, P. J. W.** 89, 373, s.l. : Journal of Fluid Mechanics, 1978.

17. *Theoretical and experimental investigations of low Mach number turbulent cavity flows.* **Chatellier, L., Laumonier, J. and Gervais, Y.** 2004.

18. *Three-dimensional linear stability analysis of cavity flows.* **Brès, G. A. and Colonius, T.** 1126, s.l. : AIAA, 2007.

19. *The mixing layer over a deep cavity at high subsonic speed.* **Forestier, N., Jacquin, L. and Geffroy, P.** 475, 101-145, s.l. : Journal of Fluid Mechanics, 2003.

20. *Visualization of the flow inside an open cavity at medium range Raynolds numbers.* **Faure, T. M., et al.** s.l. : Experiments in Fluids, Vols. 42, 169-184.

21. **Boldes, Ulfilas, et al.** Low Speed Turbulent Boundary Layer Wind Tunnels. s.l. : Wind Tunnels and Experimental Fluid Dynamics Research, 2011.

22. **Flatt, J.** The History of Boundary Layer Control Research in the United States of America. [ed.] G. V. Lachmann. *Boundary Layer and Flow Control.* New York : Pergmon Press, 1961, Vol. 1, pp. 122-143.

23. *Uber Fluessigkeitsbewegung bei sehr kleiner Reibung.* **Prandtl, Ludwig.** Heidelberg, Germany : Proc. Third International Mathmatics Congress, 1904. pp. 484-491.

24. *Boundary Layer and Flow Control.* **Lachmann, G. V.** Oxford, Great Britain : Pergamon Press, Vol. 1 and 2.

25. *On Management and Control of Turbulent Shear Flows.* **Fiedler, H. E. and Fernholtz, H.** 27, s.l. : Prog. Aer. Sci., 1990, pp. 305-387.

26. *Organized Motion in Turbulent Flow.* **Cantwell, B. J.** 13, s.l. : Annual Review of Fluid Mechanics, 1981, pp. 457-515.

27. *Coherent Motion in the Turbulent Boundary Layer.* **Robinson, S. K.** s.l. : Annual Review of Fluid Mechanics, 1991, Vol. 23, pp. 601-639.

28. *Interactive Wall Turbulence Control.* **Wilkinson, S. P.** [ed.] D. M. Bushnell and J. N. Hefner. Washington, D. C. : AIAA, 1990, pp. 479-509.

29. *Feedback Control of Turbulence.* **Moin, P. and Bewley, T.** 47, s.l. : Applied Mechanics Review, 1994, Vol. 6 part 2, pp. S3-S13.

30. *Interactive Control of Turbulent Boundary Layers: A Futuristic Overview.* **Gad-el-Hack, M.** 32, s.l. : AIAA Journal, 1994, pp. 1753-1765.

31. *Modern Developments in Flow Control.* **Gad-el-Hack, M.** 49, s.l. : Applied Mechanics Review, 1996, pp. 365-379.

32. *Dynamics and Control of High-Reynolds-Number Flow over Open Cavities.* **Rowley, Clarence W. and Williams, David R.** 38, 2006, Annual Review of Fluid Mechanics, pp. 251-276.

33. *Control of Cavity Flow by Ustream Mass-Injection.* **Vakili, A. D. and Gauthier, C.** 1, Jan. - Feb. 1994, Journal of Aircraft, Vol. 31, pp. 169-174.

34. *Active Control of Flow-Induced Cavity Resonance.* **Cattafesta, L. N., et al.** June 1997, AIAA 98-2347.

35. *Suppression of Flow-Induced Pressure Oscillations in Cavitites.* **Sarno, R. L. and Franke, M. E.** 1, s.l. : Journal of Aircraft, Jan. - Feb. 1994, Vol. 31, pp. 90-96.

36. *Control of Cavity Resonance through Very High Frequency Forcing.* **Stanek, M. J., et al.** Lahaina, Hawaii : AIAA, 2000. 6th AIAA/CEAS Aeroacoustics Conference.

37. *Active Control of Shallow Cavity Acoustic Resonance.* **McGrath, S. F. and Shaw, L. L. Jr.** June 1996, AIAA 96-1949.

38. *Closed Loop Active Control for Cavity Resonance.* **Shaw, L. and Northcraft, S.** s.l. : AIAA 99-1902, May 1998.

39. *Direct Excitation of Small-Scale Motions in Free Shear Flows.* **Wiltse, J. M. and Glazer, A.** 8, s.l. : Physics of Fluids, 1998, Vol. 10, pp. 2026-2036.

40. *Simulations of High-Frequency Excitation of a Plane Wake.* **Cain, A. B., et al.** s.l. : AIAA, 2001. AIAA-2001-0514.

41. *Perturbed Free Shear Layers.* **Ho, J. and Huerre, P.** s.l. : Annual Review of Fluid Dynamics, 1984, Vol. 16, pp. 365-424.

42. *Suppression of Cavity Resonance Using High Frequency Forcing - The Characteristic Signature of Effective Devices.* **Stanek, Michael J., et al.** s.l. : AIAA, 2001. 7th AIAA/CEAS Aeroacoustics Conference. AIAA 2001-2128.

43. *Suppression of pressure loads in cavity flows.* **Ukeilei, L. S., et al.** 2002-0661, s.l. : AIAA, 2002.

44. *On a mechanism of stabilizing turbulent free shear layers in cavity flows.* **Staneck, M. J., et al.** 36: 1621-1637, s.l. : Computers and Fluids, 2007.

45. *Large-Scale Structures in a Forced Turbulent Mixing Layer.* **Gaster, M., Kit, E. and Wygnanski, I.** s.l. : Journal of Fluid Mechanics, 1985, Vol. 150, pp. 23-39.

46. *Evolution of Instabilities in the Axisymmetric Jet. Part 2. The Flow Resulting from the Interaction Between Two Waves.* **Cohen, J. and Wygnanski, I.** s.l. : Journal of Fluid Mechanics, 1987, Vol. 176, pp. 221-235.

47. *Stability of a hybrid mean velocity profile and its relevance to cavity resonance suppression.* **Sarpotdar, S., Panickar, P. and Raman, G.** 22, 076101, s.l. : Physics of Fluids, 2010.

48. *The effects of flow oscillations on cavity drag.* **Gharib, M. and Roshko, A.** 177, 501-530, s.l. : Journal of Fluid Mechanics, 1987.

49. *Experimental investigation of oscillations in flows over shallow cavities.* **Sarohia, V.** 15:984-991, s.l. : AIAA Journal, 1977.

50. *On density effects and large structure in turbulent mixing layers.* **Brown, Garry L. and Roshko, Anatol.** 64, 775:816, s.l. : Journal of Fluid Mechanics, 1974. ISSN 0022-1120.

51. *Mechanisms for generating coherent packets of hairpin vortices in channel flow.* **Zhou, J., et al.** 387: 353-396, s.l. : Journal of Fluid Mechanics, 1999.

52. *A time resolved particle image velocimetry investigation of a cavity flow with a thick incoming turbulent boundary layer.* **Haigermoser, Christian, et al.** 105101:1-14, s.l. : Physics of Fluids, 2008, Vol. 20.

53. *Velocity and surface pressure measurements in an open cavity.* **Ukeiley, L. and Murray, N.** 38, 656, s.l. : Experiments on Fluids, 2005.

54. **Schlichting, Hermann.** *Boundary-Layer Theory.* [ed.] Karl H. Vesper. [trans.] J. Kestin. 6th. s.l. : McGraw Hill Series in Mechanical Engineering, 1968.

55. *Hydrodynamical Instability.* **Drazin, P. G. and Reid, W. H.** s.l. : Cambridge University Press, 1981.

56. *Self-sustaining oscillations of impinging free shear layers.* **Rockwell, D. and Naudascher, E.** s.l. : Annual Review of Fluid Mechanics, 1979. 11:67-94.

57. *High Frequency Acoustic Suppression - The Mystery of the Rod-in-Crossflow Revealed.* **Stanek, Michael J., et al.** Nevada : AIAA, 2003. 41st AIAA Aerospace Sciences Meeting and Exhibit.